

## ABSTRACT

GUSKE, JOSHUA TRAVIS. Modeling and Prediction of Surface Plasmon Resonance Spectroscopy. (Under the direction of Stefan Franzen).

Surface plasmon resonance (SPR) is a spectroscopy that measures the response of a surface wave at the interface of a conductor and a dielectric, called the surface plasmon polariton (SPP). In the Kretschmann configuration, a thin film of the conductor is illuminated under total internal reflection via a prism. At the appropriate angle and frequency, an absorption is seen in reflected  $p$ -polarized light. This excitation is highly sensitive to the properties of the dielectric medium, the conductor itself, and the substrate material.

Theoretical modeling is valuable in SPR, because of the high sensitivity and the large number of experimental variables involved. As the technology advances, increasingly sophisticated modeling techniques become necessary. In addition, with the aid of theoretical modeling, SPR may be used as a materials characterization tool, to study the properties of the conductors themselves.

In this dissertation, several plasmonic systems were studied. First, in chapters 2 and 3, films of silver sandwiched between two layers of non-conductive aluminum-doped zinc oxide (AZO) on glass were considered. The films were prepared by reactive pulsed DC magnetron sputtering, and the silver thickness was varied. The films' SPR response was measured in the near-IR in air. Theoretical modeling of  $R_p/R_s$  was performed by the multilayer transfer-matrix method, with the aid of a modified Nelder-Mead simplex optimization algorithm. The initial modeling results suggested that both the silver and AZO properties were significantly different from the bulk materials. In particular, the silver had a higher plasma frequency and high-frequency dielectric constant than bulk, and it was hypothesized that the AZO was contributing charge carriers into the silver layer. However, upon review it was determined that a miscalibration of the incident angles could also explain the results.

Second, in chapter 4, films of silver sandwiched between two layers of AZO were deposited using pulsed laser deposition (PLD) onto both glass and  $\text{CaF}_2$ . The film thicknesses were held nearly constant, and the AZO plasma frequency was varied by changing the Al doping concentration and oxygen pressure during deposition. The films' SPR response was measured in near-IR in two separate instruments, in air for the films on glass and in water for the films on  $\text{CaF}_2$ . In the theoretical modeling, which took place via the multilayer transfer-matrix model, the bulk silver dielectric function was used, and the AZO dielectric function was approximated as a hybrid between a conductive Drude model and the ZnO bulk. Initial results were promising, but indicated that the system was limited by the accuracy of the film thickness measurements and the consistency of the deposition process.

Third, in chapter 5, pure AZO films were assessed using SPR spectroscopy. The films were deposited using PLD in an oxygen environment onto  $\text{CaF}_2$ . The SPR responses of the films were measured in both air, in the near-IR, and in water, in the mid-IR. A modified Nelder-Mead simplex optimization algorithm was used to determine the optical constants of the films in the Drude model. The high-frequency dielectric constant was consistent with literature values. However, the plasma frequency and damping constant suggested that the films had a higher free electron mass than is reported in the literature. In addition, the spectra in water were complex, which was explained as the result of interaction of the water molecular vibrations with the surface plasmon polariton in the mid-IR. This is believed to be the first reported observation of a mid-IR water-plasmon interaction in this fashion.

© Copyright 2013 by Joshua Travis Guske

All Rights Reserved

Modeling and Prediction of Surface Plasmon Resonance Spectroscopy

by  
Joshua Travis Guske

A dissertation submitted to the Graduate Faculty of  
North Carolina State University  
in partial fulfillment of the  
requirements for the degree of  
Doctor of Philosophy

Chemistry

Raleigh, North Carolina

2013

APPROVED BY:

---

Dr. Stefan Franzen  
Committee Chair

---

Dr. Jon-Paul Maria

---

Dr. David Aspnes

---

Dr. Jan Genzer

## **DEDICATION**

Dedicated to the memory of

Scott A. Guske

1956 – 1994

## BIOGRAPHY

Joshua Travis Guske was born on August 22, 1984 in Michigan. He attended elementary school at Holy Nativity Episcopal School in Panama City Florida, followed by middle school and high school in Murphy, North Carolina. Here, conducted his first truly scientific experiment for a science fair project: a comparison of the effectiveness of various plant species at controlling erosion. It was also here, at Murphy High School, that he was first introduced to the concepts of chemistry.

After graduating from high school in 2002, Josh entered Elon University, a liberal arts school in the piedmont of North Carolina, in the Science Fellows program. He completed a major in Chemistry and a minor in Multimedia Authoring. His research project at Elon was the attempted detection of estrogen-like endocrine disrupting compounds in river water via solid-phase extraction and high performance liquid chromatography. He also spent one summer conducting chemical ecology research at the Mote Marine Laboratory in Sarasota, Florida, studying a pollution detection protocol that used the fluorescence of laundry detergent as an indicator of discharges. After graduating from Elon in 2006, Josh was hired as a laboratory technician at Kay Chemical Co, in Greensboro, NC, which involved performance testing and reformulation of cleaning products.

In 2007, Josh decided to enter graduate school at North Carolina State University's department of Chemistry, and soon discovered Stefan Franzen's project on surface plasmon resonance. With virtually no background in materials science, solid state physics, or optics, there were many challenges to overcome, but Josh was eventually able to make significant progress in the project, receiving his Ph.D. in June of 2013. Shortly thereafter, Josh moved on to take a position as a postdoctoral associate at Massachusetts Institute of Technology, in the Center for Materials Science and Engineering's X-ray Diffraction Shared Experimental Facility, under the supervision of Scott Speakman.

## ACKNOWLEDGMENTS

I would like to give my sincere thanks to the following people and organizations, for their numerous contributions to this project:

Stefan Franzen, and group:

- Misun Kang
- Alina Efremenko
- Crissy Rhodes
- Marta Cerruti
- Trey Wingerson
- Drew Williams

Maria Moreno

David Aspnes

Stephen Weibel

Bill Gerber

Simon Lappi

Kirill Efimenko

Jan Genzer

Jon-Paul Maria, and group:

- Mark Losego
- Edward Sachet
- Michelle Casper
- Peter Lam
- Nicole Estrich

Acree Tech, Inc.:

- Jeff Brown
- Alex Welsh
- Mike McFarland

The National Science Foundation

Karl Booksh, and group:

- Nick Menegazzo
- Laurel Kegel

## TABLE OF CONTENTS

LIST OF TABLES .....	viii
LIST OF FIGURES .....	ix
1. Introduction .....	1
1.1 Surface plasmon resonance .....	4
1.1.1 The Drude model .....	6
1.1.2 Surface plasmons .....	11
1.1.3 SPR experimental considerations .....	19
1.2 <u>Equation Section (Next)</u> Thin film optics .....	22
1.2.1 Fresnel equations for reflectance from a single thin film .....	23
1.2.2 Matrix method for reflectance from a system of thin films .....	25
1.3 References .....	28
2. Reprint: Infrared surface plasmon resonance of AZO-Ag-AZO sandwich thin films .....	33
2.1 Introduction .....	34
2.1.1 Sandwich thin films .....	35
2.1.2 Surface plasmon resonance .....	36
2.2 Materials and methods .....	37
2.2.1 Film deposition .....	37
2.2.2 SPR analysis .....	38
2.3 Modeling .....	40
2.3.1 SPR spectra .....	40
2.3.2 Bulk silver .....	43
2.3.3 Sensitivities .....	44

2.4	Transmission .....	45
2.5	Results .....	46
2.6	Discussion .....	48
2.7	Conclusions .....	51
2.8	Acknowledgments .....	51
2.9	References .....	52
3.	Reassessment of data: Infrared surface plasmon resonance of AZO-Ag-AZO sandwich thin films .....	60
3.1	Introduction .....	60
3.2	Experiment .....	60
3.3	Results .....	64
3.3.1	Method 1: Drude AZO, bulk Ag .....	64
3.3.2	Method 2: Bulk ZnO, bulk Ag .....	66
3.3.3	Method 3: Constant AZO, Drude Ag .....	67
3.3.4	Method 4: Free angles .....	68
3.4	Discussion .....	70
3.5	Conclusions .....	73
3.6	Acknowledgments .....	74
3.7	References .....	74
4.	Trilayer AZO-Ag-AZO films for SPR deposited by PLD: Influence of AZO conductivity .....	75
4.1	Introduction .....	75
4.2	Experiment .....	81
4.2.1	Film depositions .....	81

4.2.2	SPR analysis.....	83
4.2.3	Theoretical modeling .....	84
4.3	Results .....	90
4.4	Discussion .....	92
4.5	Conclusions .....	95
4.6	Acknowledgments .....	97
4.7	References .....	97
5.	Infrared AZO surface plasmon resonance: relation to material properties .....	102
5.1	Introduction .....	102
5.2	Method .....	104
5.3	Results .....	108
5.4	Discussion .....	111
5.5	Conclusions .....	115
5.6	Acknowledgments .....	116
5.7	References .....	116

## LIST OF TABLES

Table 2.1: Summary of fitted parameters for the AZO/Ag/AZO films. ....	40
Table 2.2: Estimated sensitivities of the films to refractive index changes. Sensitivities expressed in units per refractive index unit (RIU): $S_\theta$ : angle interrogation, $S_\nu$ : wavenumber interrogation, $S_\lambda$ : wavelength interrogation. ....	45
Table 3.1: Film thicknesses for the AZO-Ag-AZO sandwich thin films, as originally reported, and as measured by XRR. ....	62
Table 3.2: Comparison of fitting results, using the sum squared error, for each fitting method described. ....	70
Table 3.3: Comparison of angles measured on the instrument, back-calculated using Snell's law, and the fitting results from the free angle calculation. The fitting results are close to both the physically measured angle and the Snell angle, and thus can be considered acceptable. ....	72
Table 4.1: Methodology for the AZO / Ag / AZO sandwich films and sheet resistances for pure AZO deposited by the same method. ....	83
Table 4.2: AZO Drude term parameters $\omega_p$ and $\Gamma$ for the AZO layers, in the right hand sides of Figs. 4.4 and 4.5. ....	91
Table 4.3: The AZO resistivities, as measured by four-point probe and as calculated from the optical parameters listed in Table 4.2. ....	91
Table 5.1: Results of the Hall Effect and four-point probe electrical characterizations of the AZO films used in this study. ....	111

## LIST OF FIGURES

Figure 1.1: Cartoon representation of a propagating surface plasmon polariton. Under the appropriate conditions, electromagnetic radiation striking a metallic film causes electrons to oscillate, which causes a wave of polarization to propagate in the x-direction..... 5

Figure 1.2: Example Drude dielectric function, silver in the near-IR. The model (black line) is shown compared to spectroscopic ellipsometry values from several sources. TG1: Acree Tech Inc.; Sopra: Sopra, S.A. Database; Ordal: Ordal *et al.* [31]; J&C: Johnson and Christy [32]. ..... 9

Figure 1.3: Schematic of the coordinate system along with pictorial representations of the  $x$  and  $z$  electric fields of a surface polariton in media A and B. .... 13

Figure 1.4: Dispersion relations for: light propagating through air (small dashes), light at a BK-7 prism interface at  $60^\circ$  (large dashes), the imaginary component of the waves at the conductor/air interface (dots), and the real component of the plasmon waves at the conductor/air interface (solid). The real component of the plasmon waves is separated into regions radiative plasmon (RP), quasi-bound mode (QBM), and surface plasmon polariton (SPP). The dispersion relation for light in air never crosses the SPP line..... 18

Figure 1.5: A diagram of the main optical elements in a typical Kretschmann-configuration SPR spectrometer..... 20

Figure 1.6: Example spectrum from a typical FT-SPR instrument at varying angles. Two excitations are seen: the surface plasmon polariton (SPP), and the quasi-bound mode (QBM)..... 22

Figure 1.7: Notation convention for a system of  $h$  thin films bounded by materials  $A$  and  $C$ .23

Figure 2.1: Experimental (left) and theoretical (right) FTIR-SPR spectra from  $4200\text{ cm}^{-1}$  to  $11000\text{ cm}^{-1}$  ( $2.38\text{ }\mu\text{m}$  to  $0.909\text{ }\mu\text{m}$ ) for (A) the 23 nm AZO / 5 nm Ag / 23 nm AZO film, (B) the 23 nm AZO / 10 nm Ag / 23 nm AZO film, (C) the 23 nm AZO / 11.2 nm Ag / 23nm AZO film, and (D) the 42.0 nm AZO / 13.9 nm Ag / 22.4 nm AZO film. The summary for all films is shown in Table 2.1. .... 39

Figure 2.2: Experimental (left) and theoretical (right) FTIR-SPR spectra from  $4200\text{ cm}^{-1}$  to  $11000\text{ cm}^{-1}$  ( $2.38\text{ }\mu\text{m}$  to  $0.909\text{ }\mu\text{m}$ ) for (A) the 21.5 nm AZO / 15.8 nm Ag / 48.5 nm

AZO film, (B) the 27.5 nm AZO / 20.0 nm Ag / 27.1 nm AZO film, (C) the 23 nm AZO / 30 nm Ag / 23nm AZO film, and (D) the 23 nm AZO / 50 nm Ag / 23 nm AZO film. The summary for all films is shown in Table 2.1. ....	42
Figure 2.3: Complex dielectric function ( $\epsilon = \epsilon_1 + i\epsilon_2$ ) for bulk silver from 4000 to 11290 $\text{cm}^{-1}$ wavenumber (2.5 $\mu\text{m}$ to 0.886 $\mu\text{m}$ wavelength), from the following data sources: ATI: Acree Tech Inc.; Sopra: Sopra S. A. Database; Ordal: Ordal, et al.[58]; J&C: Johnson and Christy[59]. Model: Drude model fit, using the means across data sources of the parameters $\epsilon_\infty$ , $\omega_p$ , and $\Gamma$ given by the method in the text. The reported $R^2$ values are the averages. SPR: Average result from SPR modeling ( <i>cf.</i> Table 2.1). ....	44
Figure 2.4: UV-vis transmission spectra of the AZO/Ag/AZO films.....	46
Figure 3.1: Contour map of sum squared error for film G, as a function of AZO Drude model parameters plasma frequency ( $\omega_p$ ) and high-frequency dielectric constant ( $\epsilon_\infty$ ), using constrained value for the damping ( $\Gamma=3457.7 \text{ cm}^{-1}$ ) and using the bulk silver dielectric function. The minimum of 86.2 is located at ( $\epsilon_\infty=1.7859$ , $\omega_p=2774.6 \text{ cm}^{-1}$ ). ....	65
Figure 3.2: Left: The background-corrected experimental FT-SPR spectrum for film G. Right: Resulting theoretical FT-SPR spectrum at the SSE minimum of the AZO Drude model parameter space in Fig. 3.1 ( $\epsilon_\infty=1.7859$ , $\omega_p=2774.6 \text{ cm}^{-1}$ , $\Gamma=3457.7 \text{ cm}^{-1}$ ), using the bulk silver dielectric function. ....	66
Figure 3.3: Left: The background-corrected experimental FT-SPR spectrum for film G. Right: Resulting theoretical FT-SPR spectrum using the bulk silver dielectric function and the bulk ZnO dielectric function. With the angles fixed at their previously reported values, there are no parameters to optimize, and only one SPR spectrum is possible. The sum squared error by this method is 281.1. ....	67
Figure 3.4: Left: The background-corrected experimental FT-SPR spectrum for film G. Right: Resulting theoretical FT-SPR spectrum, returning to the original fitting method. The silver Drude model parameters ( $\epsilon_\infty$ , $\omega_p$ , and $\Gamma$ ) were allowed to vary freely, as was the AZO scalar dielectric function ( $\epsilon_{\text{AZO}}$ ). The SSE minimum in the four-dimensional parameter space is then 8.123, at ( $\epsilon_\infty=32.90$ , $\omega_p=9.386 \times 10^4 \text{ cm}^{-1}$ , $\Gamma=600 \text{ cm}^{-1}$ , and $\epsilon_{\text{AZO}}=2.360$ ). ....	68

- Figure 3.5: Contour map of the SSE for fitting film G in the angle space, with the starting angle on the x-axis and the angle increment on the y-axis. The minimum SSE of 5.09 is located at ( $\theta_{\text{start}} = 31.65^\circ$ ,  $\theta_{\text{incr}} = 0.67^\circ$ ), which produces the SPR spectrum seen on the right side of Fig. 3.6..... 69
- Figure 3.6: Left: The background-corrected experimental FT-SPR spectrum for film G. Right: Resulting theoretical FT-SPR spectrum, allowing angles of incidence to vary freely. The best fit is obtained by the parameters ( $\theta_{\text{start}} = 31.65^\circ$ ,  $\theta_{\text{incr}} = 0.67^\circ$ ), and produces an SSE of 5.09. .... 69
- Figure 4.1: Theoretical SPR reflectance ( $R_p/R_s$ ) showing the difference between a bare 30 nm silver film (left) and a 20 nm ZnO / 30 nm Ag / 20 nm ZnO film (right). Both films were modeled on calcium fluoride in water, using a  $60^\circ$  calcium fluoride prism. .... 78
- Figure 4.2: Theoretical SPR reflectance ( $R_p/R_s$ ), as in Fig. 2.1 except on glass and in air, showing the difference between a bare 30 nm silver film (left) and a 20 nm ZnO / 30 nm Ag / 20 nm ZnO film (right). Both films were modeled on BK-7 glass in air, using a  $60^\circ$  BK-7 glass prism. The “doubling” of the resonances is due to the glass dispersion, which causes the light’s wavevector to interact with the SPP wavevector at multiple frequencies. .... 78
- Figure 4.3: Theoretical FT-SPR spectra of (A): a 30 nm Ag film with an 800 nm ZnO underlayer, showing the onset of interference effects compared to Fig. 4.2, and (B): a 30 nm Ag film with an 80 nm ZnO overlayer, showing the high dependence on the thickness of the ZnO top layer. Note that unlike previous figures, the angle ranges for the left and right sides of this figure are different..... 80
- Figure 4.4: AZO plasma frequency series for Instrument 1, for the films on BK-7 glass in air, showing experimental results (left) and theoretical results (right). (A, B): Undoped ZnO, deposited at 20.0 mTorr  $O_2$ . Thicknesses 91.8 / 25.0 / 91.8 nm. ZnO  $\omega_p=5000\text{ cm}^{-1}$ ,  $\Gamma=2000\text{ cm}^{-1}$ . (C, D): 3at% Al AZO, deposited at 20.0 mTorr  $O_2$ . Thicknesses 84.9 / 25.0 / 84.9 nm. AZO  $\omega_p=7000\text{ cm}^{-1}$ ,  $\Gamma=2000\text{ cm}^{-1}$ . (E, F): 4at% Al AZO, deposited at 10.0 mTorr  $O_2$ . Thicknesses 87.6 / 25.0 / 87.6 nm. AZO  $\omega_p=9000\text{ cm}^{-1}$ ,  $\Gamma=2000\text{ cm}^{-1}$ . (G, H): 3at% Al AZO, deposited at 10.0 mTorr  $O_2$ . Thicknesses 84.9 / 25.0 / 84.9 nm. AZO

$\omega_p=10000 \text{ cm}^{-1}$ ,  $\Gamma=2000 \text{ cm}^{-1}$ . (I, J): 4at% Al AZO, deposited at 2.0 mTorr  $\text{O}_2$ . Thicknesses 76.7 / 20.0 / 76.7 nm. AZO  $\omega_p=12000 \text{ cm}^{-1}$ ,  $\Gamma=2000 \text{ cm}^{-1}$ . Discrepancies between theory and experiment are most likely due to error in measured thicknesses. ... 86

Figure 4.5: AZO plasma frequency series for Instrument 2, for the films on  $\text{CaF}_2$  in water, showing experimental results (left) and theoretical results (right). (A, B): Undoped ZnO, deposited at 20.0 mTorr  $\text{O}_2$ . Thicknesses 80.0 / 25.0 / 80.0 nm. ZnO  $\omega_p=4000 \text{ cm}^{-1}$ ,  $\Gamma=2000 \text{ cm}^{-1}$ . (C, D): 3at% Al AZO, deposited at 20.0 mTorr  $\text{O}_2$ . Thicknesses 84.9 / 25.0 / 84.9 nm. AZO  $\omega_p=6000 \text{ cm}^{-1}$ ,  $\Gamma=2000 \text{ cm}^{-1}$ . (E, F): 4at% Al AZO, deposited at 10.0 mTorr  $\text{O}_2$ . Thicknesses 87.6 / 25.0 / 87.6 nm. AZO  $\omega_p=8000 \text{ cm}^{-1}$ ,  $\Gamma=2000 \text{ cm}^{-1}$ . (G, H): 3at% Al AZO, deposited at 10.0 mTorr  $\text{O}_2$ . Thicknesses 84.9 / 25.0 / 84.9 nm. AZO  $\omega_p=11000 \text{ cm}^{-1}$ ,  $\Gamma=2000 \text{ cm}^{-1}$ . ..... 88

Figure 4.6: The experimental SPR spectrum of Film C on glass (left), compared to the theoretical spectrum that is obtained when the thicknesses are adjusted to 73 nm / 28 nm / 73 nm for AZO / Ag / AZO (right). ..... 94

Figure 4.7: The experimental SPR spectrum of Film A on glass (left), compared to the theoretical spectrum that is obtained when the thicknesses are adjusted to 130 nm / 40 nm / 130 nm for AZO / Ag / AZO (right). ..... 95

Figure 5.1: The dielectric functions of calcium fluoride, from spectroscopic ellipsometry, and water, from [34]. The water dielectric function has a significant imaginary component due to molecular vibrations. .... 107

Figure 5.2: (Left side) Near-IR SPR spectra of the AZO films A, B, and C, in an air environment. (Right side) Theoretical modeling results for the same films. Films A and B were prepared identically, while film C was prepared in a higher pressure oxygen environment. .... 109

Figure 5.3: (Left side) Mid-IR SPR spectra of the AZO films A, B, and C, in a water environment. (Right side) Theoretical modeling results for the same films, using the numerical results of the air-environment modeling of Fig. 5.2. Films A and B were prepared identically, while film C was prepared in a higher pressure oxygen environment. .... 110

Figure 5.4: Surface plasmon polariton (SPP) dispersion relation for AZO in water ( $k_{spp}$ ), showing real and imaginary parts and the added complexity from the molecular vibrations of the water. Also shown is the dispersion of an evanescent wave from CaF<sub>2</sub> at 65° incidence, and points of intersection where the SPP may be driven..... 114

Figure 5.5: Theoretical SPR spectra for film A, with labeled regions corresponding to the labeled intersections in Fig. 5.4. .... 114

# 1. Introduction

Many chemists and biochemists who read this dissertation will already be familiar with the concepts of surface plasmon resonance (SPR), due its popular applications: surface enhancement from localized SPR on metallic particles, and biosensing on planar metallic surfaces. However, the physics that cause these effects are often seen as arcane, and thus many scientists will spend their entire careers having used the effects of SPR without understanding the fundamentals. The theories are intrinsically useful, as they enable the accurate prediction and modeling of SPR responses. This is necessary in a surprisingly large number of cases: for example, in designing an SPR system that will operate at a particular angle and frequency range, in the extraction of information from SPR spectra, or in the search for new SPR-active materials. Moreover, as SPR devices become increasingly sophisticated and accurate, our ability to understand the spectra must grow accordingly.

This introduction is intended to provide readers with a small foundation in SPR on thin conductive films (the so-called propagating surface plasmon), and the methods used to predict and model SPR responses on such films. It assumes some knowledge of chemistry, solid-state physics, materials science, and classical optics. It does not cover localized SPR on particles, the principles of surface-enhanced scattering, SPR in waveguide modes, or biosensing. Readers who desire more detailed coverage of these and other topics are referred to the following resources:

## **Surface Plasmon Resonance: General Introductions**

- [1] S. A. Maier, *Plasmonics: Fundamentals and Applications*, (Springer, New York, 2007).
- [2] L. Novotny and B. Hecht, “Chapter 12: Surface Plasmons,” in *Principles of Nano-Optics*, (Cambridge, 2006).
- [3] V. H. Pérez-Luna, “Surface plasmon resonance,” in *Surfaces and Interfaces for Biomaterials*, P. Vadgama, ed. (CRC Press, 2005), pp. 249-270.

### **Surface Plasmon Resonance: Physics, LSPR, and Advanced Topics**

- [4] D. Sarid and W. A. Challener, *Modern Introduction to Surface Plasmons: Theory, Mathematica Modeling, and Applications* (Cambridge University Press, 2010).
- [5] J. M. Pitarke, V. M. Silkin, E. V. Chulkov and P. M. Echenique, "Surface plasmons in metallic structures," *J. Opt. A: Pure Appl. Opt.* **7**, S73 (2005).
- [6] V. M. Agranovich and D. L. Mills, *Surface Polaritons* (North-Holland, 1982).
- [7] S. I. Bozhevolnyi, *Plasmonic nanoguides and circuits* (Pan Stanford, 2009).
- [8] M. L. Brongersma and P. G. Kik, *Surface plasmon nanophotonics* (Springer, 2007).
- [9] R. Zia, M. D. Selker, P. B. Catrysse, and M. L. Brongersma, "Geometries and materials for subwavelength surface plasmon modes," *J. Opt. Soc. Am. A* **21**(12), 2442-2446 (2004).

### **Surface Plasmon Resonance: Biosensors and Other Applications**

- [10] Jiří Homola, S. S. Yee, and G. Gauglitz. "Surface Plasmon Resonance Sensors: Review," *Sensors and Actuators B*, **54** 3-15 (1999).
- [11] Jiří Homola, "Present and future of surface plasmon resonance biosensors," *Anal. Bioanal. Chem.* **377**, 528–539 (2003).

### **Publications by the NCSU Surface Plasmon Resonance Materials Group**

- [12] E. Sacht, M. Losego, J. Guske, S. Franzen, and J. Maria, "Mid-infrared surface plasmon resonance in zinc oxide semiconductor thin films," *Applied Physics Letters* **102**, 051111 (2013).
- [13] J. Guske, J. Brown, A. Welsh, and S. Franzen, "Infrared surface plasmon resonance of AZO-Ag-AZO sandwich thin films," *Optics Express* **20**, 23215-23226 (2012).

- [14] M. Losego, J. Guske, A. Efremenko, J. Maria, and S. Franzen, "Characterizing the Molecular Order of Phosphonic Acid Self-Assembled Monolayers on Indium Tin Oxide Surfaces," *Langmuir* **27**, 11883-11888 (2011).
- [15] S. Franzen, C. Rhodes, M. Cerruti, R. Gerber, M. Losego, J. Maria, and D. Aspnes, "Plasmonic phenomena in indium tin oxide and ITO-Au hybrid films," *Optics Letters* **34**, 2867-2869 (2009).
- [16] R. Gerber, D. Leonard, and S. Franzen, "Conductive thin film multilayers of gold on glass formed by self-assembly of multiple size gold nanoparticles," *Thin Solid Films* **517**, 6803-6808 (2009).
- [17] M. Losego, A. Efremenko, C. Rhodes, M. Cerruti, S. Franzen, and J. Maria, "Conductive oxide thin films: Model systems for understanding and controlling surface plasmon resonance," *Journal of Applied Physics* **106**, 024903 (2009).
- [18] S. Franzen, "Surface plasmon polaritons and screened plasma absorption in indium tin oxide compared to silver and gold," *Journal of Physical Chemistry C* **112**, 6027-6032 (2008).
- [19] C. Rhodes, S. Lappi, D. Fischer, S. Sambasivan, J. Genzer, and S. Franzen, "Characterization of monolayer formation on aluminum-doped zinc oxide thin films," *Langmuir* **24**, 433-440 (2008).
- [20] C. Rhodes, M. Cerruti, A. Efremenko, M. Losego, D. Aspnes, J. Maria, and S. Franzen, "Dependence of plasmon polaritons on the thickness of indium tin oxide thin films," *Journal of Applied Physics* **103**, 093108 (2008).
- [21] M. Cerruti, C. Rhodes, M. Losego, A. Efremenko, J. Maria, D. Fischer, S. Franzen, and J. Genzer, "Influence of indium-tin oxide surface structure on the ordering and coverage of carboxylic acid and thiol monolayers," *Journal of Physics D-Applied Physics* **40**, 4212-4221 (2007).

- [22] C. Rhodes, S. Franzen, J. Maria, M. Losego, D. Leonard, B. Laughlin, G. Duscher, and S. Weibel, "Surface plasmon resonance in conducting metal oxides," *Journal of Applied Physics* **100**, 054905 (2006).
- [23] S. Brewer, A. Allen, S. Lappi, T. Chasse, K. Briggman, C. Gorman, and S. Franzen, "Infrared detection of a phenylboronic acid terminated alkane thiol monolayer on gold surfaces," *Langmuir* **20**, 5512-5520 (2004).
- [24] S. Brewer, and S. Franzen, "Indium tin oxide plasma frequency dependence on sheet resistance and surface adlayers determined by reflectance FTIR spectroscopy," *Journal of Physical Chemistry B* **106**, 12986-12992 (2002).
- [25] S. Brewer, and S. Franzen, "Optical properties of indium tin oxide and fluorine-doped tin oxide surfaces: correlation of reflectivity, skin depth, and plasmon frequency with conductivity," *Journal of Alloys and Compounds* **338**, 73-79 (2002).

### 1.1 Surface plasmon resonance

Surface plasmon resonance (SPR) is, broadly, the phenomenon in which conduction electrons, usually in a metal or metal-like material, interact with light to produce an absorption instead of the usual reflection. The absorbed light is converted into a different type of electromagnetic wave, called a surface plasmon polariton (SPP, or informally, "surface plasmon"), which can be imagined as a wave of alternating polarization that is bound to the surface of the conductor (Fig. 1). In the case of a thin film, the SPP is able to propagate a short distance away from its point of excitation, and is therefore frequently called the propagating surface plasmon. Surface plasmon resonance is also observed on particles, but these polaritons do not propagate and the effect is thus given the name localized surface plasmon resonance (LSPR). The distinction is not trivial, as the physical conditions that enable the polariton to propagate are not present in colloidal particles. Since the vast majority of this work focuses on propagating SPR, this introduction will not cover LSPR, and the reader is instead referred to Maier, [1] Sarid, *et al.*, [4] and Pitarke, *et al.* [5].

Experimentally, we use the Kretschmann configuration, in which a thin film of a conductor that has been deposited onto a transparent substrate is exposed to light through its underside, and the reflected light is monitored. When a very particular angle and frequency are reached, an absorption is seen that is typically very intense. This absorption is very sensitive to the conductor's geometry and composition, light angle and frequency, and the composition of the surrounding materials. Because of this sensitivity, the phenomenon is frequently used as a spectroscopy, most notably in the biosciences for label-free biomolecule detection. This section of the introduction will explore the physical causes of this phenomenon, and will discuss the setup of, and typical features seen in, an SPR experiment.

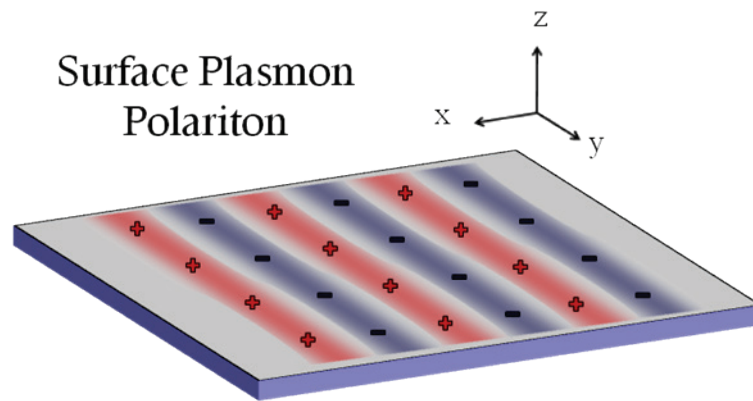


Figure 1.1: Cartoon representation of a propagating surface plasmon polariton. Under the appropriate conditions, electromagnetic radiation striking a metallic film causes electrons to oscillate, which causes a wave of polarization to propagate in the x-direction.

SPR was first noted as an anomaly in light reflected from metal diffraction gratings by Robert Wood in 1902 [26], and was known as "Wood's Anomaly" until the 1960s, when it was recognized by Ritchie to be related to the surface plasmons observed in electron energy loss spectroscopy [27]. Key developments in this era were made by Otto [28, 29] and

Kretschmann and Raether [30], who engineered experimental geometries that are widely used today.

### 1.1.1 The Drude model

Plasmons are waves in conduction electrons. The key to understanding plasmons is the Drude dielectric function model. In a good conductor, the electrons are considered free to move, with a uniform, immobile, positive ionic background. When the electrons are displaced, they create a polarization that acts as a restoring force, and thus are a collective harmonic oscillator, the harmonic frequency of which is known as the plasma frequency  $\omega_p$ .

As a first step toward understanding SPR, we derive an expression for the Drude model, *i.e.* the dielectric function of a generic electrical conductor, from first principles. The relative permittivity, or dielectric function, is usually defined as  $\varepsilon = 1 + \chi$ , where  $\chi$  is the electric susceptibility. For real materials, however, Drude theory does not encompass every process that may contribute to the dielectric function. In particular, there is a nearly constant background contribution from the ionic core, and so the constant 1 is replaced by the high-frequency dielectric constant,  $\varepsilon_\infty$ :

$$\varepsilon = \varepsilon_\infty + \chi. \quad (1.1.1)$$

The electric susceptibility may be defined in terms of the polarization  $\mathbf{P}$ , which is simply the total of the charge displacements:

$$\mathbf{P} = \chi \varepsilon_0 \mathbf{E} = n e \mathbf{x} \quad (1.1.2)$$

$$\chi = \frac{n e \mathbf{x}}{\varepsilon_0 \mathbf{E}}. \quad (1.1.3)$$

These electrons are behaving as harmonic oscillators, so we use the classical harmonic oscillator equation. In this case, the force is generated by the electric field from the charge displacements:

$$\mathbf{F} = e \mathbf{E} = m^* \frac{d^2}{dt^2} \mathbf{x} + \gamma \frac{d}{dt} \mathbf{x}. \quad (1.1.4)$$

Here, the mass  $m^*$  is the free electron mass, which is typically a fraction of the vacuum electron mass  $m_e$ . As a solution to this differential equation, both the charge displacements and the electric field oscillate sinusoidally and in phase, which allows us to define the susceptibility in terms of the time-invariant amplitudes:

$$\mathbf{x} = \mathbf{x}_0 e^{-i\omega t} \quad (1.1.5)$$

$$\mathbf{E} = \mathbf{E}_0 e^{-i\omega t} \quad (1.1.6)$$

$$\chi = \frac{ne\mathbf{x}_0}{\varepsilon_0 \mathbf{E}_0}. \quad (1.1.7)$$

Taking the derivatives of equations (1.1.5) and (1.1.6), we can arrive at an expression for  $\mathbf{x}_0$ :

$$\mathbf{F} = e\mathbf{E}_0 e^{-i\omega t} = -m^* \omega^2 \mathbf{x}_0 e^{-i\omega t} - i\omega\gamma \mathbf{x}_0 e^{-i\omega t} \quad (1.1.8)$$

$$\mathbf{x}_0 = \frac{-e\mathbf{E}_0}{m^* \omega^2 + i\omega\gamma}. \quad (1.1.9)$$

Substituting this expression for  $\mathbf{x}_0$  into equation (1.1.7), we then obtain for the susceptibility:

$$\chi = \left( \frac{ne^2}{\varepsilon_0 m^*} \right) \left( \frac{-1}{\omega^2 + i\omega\gamma/m^*} \right). \quad (1.1.10)$$

Then, we can define the plasma frequency  $\omega_p$  and the damping frequency  $\Gamma$ , both of which take units of rad/s in this convention:

$$\omega_p^2 \equiv \frac{ne^2}{\varepsilon_0 m^*} \quad (1.1.11)$$

$$\Gamma \equiv \gamma/m^*. \quad (1.1.12)$$

Substituting these expressions into equations (1.1.10) and (1.1.1), the dielectric function may be expressed in its most common form:

$$\varepsilon = \varepsilon_\infty - \frac{\omega_p^2}{\omega^2 + i\omega\Gamma}. \quad (1.1.13)$$

Lastly, the damping force constant  $\gamma$  is defined, by examining the constant velocity case, using Ohm's law:

$$\frac{d^2}{dt^2} \mathbf{x} = 0 \quad (1.1.14)$$

$$\frac{d}{dt} \mathbf{x} = \mathbf{v} = \frac{\mathbf{J}}{en} \quad (1.1.15)$$

$$\mathbf{J} = \sigma \mathbf{E} = n\mu e \mathbf{E}. \quad (1.1.16)$$

Here,  $\mu$  is the charge carrier mobility. We then have, for the velocity:

$$\frac{d}{dt} \mathbf{x} = \frac{n\mu e \mathbf{E}}{en} = \mu \mathbf{E}. \quad (1.1.17)$$

Substituting equations (1.1.14) and (1.1.17) into equation (1.1.4):

$$e \mathbf{E} = 0 + \gamma \mu \mathbf{E} \quad (1.1.18)$$

$$\gamma = e/\mu. \quad (1.1.19)$$

This allows the damping frequency constant  $\Gamma$  to be defined in terms of materials parameters:

$$\boxed{\Gamma = \gamma/m^* = e/\mu m^*}. \quad (1.1.20)$$

Equations (1.1.11), (1.1.13), and (1.1.20) explain the optical properties of most metals and degenerate semiconductors at frequencies below their plasma frequencies to a high degree of accuracy. If deviations from this model are present, they will usually occur when an interband electronic transition exists in the appropriate frequency range. This is the case for gold above  $14000 \text{ cm}^{-1}$ , and for silver above approximately  $25000 \text{ cm}^{-1}$  [18]. When it is necessary to account for these deviations, additional terms may be added to the dielectric function model, or the experimentally-determined function may be interpolated.

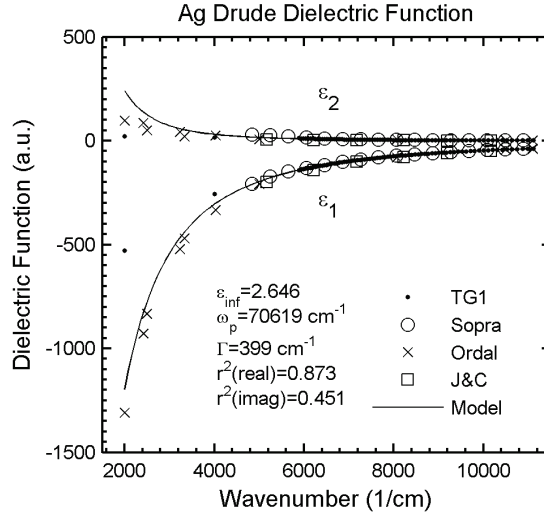


Figure 1.2: Example Drude dielectric function, silver in the near-IR. The model (black line) is shown compared to spectroscopic ellipsometry values from several sources. TG1: Acree Tech Inc.; Sopra: Sopra, S.A. Database; Ordal: Ordal *et al.* [31]; J&C: Johnson and Christy [32].

The Drude dielectric function for metals has now been derived and is shown in its final form in equation (1.1.13), and we can explore some of its properties. For reference, the silver dielectric function, which fits this model very well in the near-IR, is displayed in Fig. 1.2. This dielectric function has both a real part and an imaginary part, which can be separated and written as:

$$\varepsilon = \varepsilon_1 + i\varepsilon_2 \quad (1.1.21)$$

$$\varepsilon_1 = \varepsilon_\infty - \frac{\omega_p^2}{\Gamma^2 + \omega^2} \quad (1.1.22)$$

$$\varepsilon_2 = \frac{\omega_p^2 \Gamma}{\Gamma^2 \omega + \omega^3} \quad (1.1.23)$$

These equations can be solved for  $\omega_p$  and  $\Gamma$ , in the fashion of Ordal *et al.* [31] to obtain:

$$\Gamma = \frac{\omega \varepsilon_2}{\varepsilon_\infty - \varepsilon_1} \quad (1.1.24)$$

$$\omega_p^2 = (\varepsilon_\infty - \varepsilon_1)(\Gamma^2 + \omega^2) \quad (1.1.25)$$

If it is assumed that  $\varepsilon_\infty \ll |\varepsilon_1|$ , which is true at low frequencies relative to the plasma frequency, the precise value of  $\varepsilon_\infty$  is not important, and it may be set as unity. In this manner, equations (1.1.24) and (1.1.25) can be used to quickly evaluate a material without the need for a nonlinear regression.

At high frequencies, the real part  $\varepsilon_1$  approaches  $\varepsilon_\infty$  and inevitably crosses zero at some frequency; in ellipsometry and EELS experiments this is often called the “plasma frequency.” However, this empirical value does not necessarily equal that of equation (1.1.11). The two values are only equal in the ideal case: when  $\varepsilon_\infty = 1$  and  $\Gamma = 0$ , and there are no interband transitions. In real materials, the zero crossing is almost always different than equation (1.1.11) indicates, as each of the conditions  $\varepsilon_\infty > 1$ , the presence of interband transitions, and  $\Gamma > 0$ , contributes to  $\varepsilon_1$ . Similarly, the imaginary part  $\varepsilon_2$  approaches zero at  $\omega \rightarrow \infty$ , but only when interband transitions are not present. In real metals such as Ag and Au, interband transitions give a significant amount of positive structure to  $\varepsilon_2$  that the Drude model cannot simulate. In comparison, the transparent conductive metal oxides indium tin oxide (ITO) and aluminum zinc oxide (AZO) do not have interband transitions near their plasma frequencies, which make them nearly ideal in terms of the Drude model (this feature, combined with plasma frequencies in the near-infrared, also makes them transparent to visible light) [18].

The link to materials properties is evident when equations (1.1.11) and (1.1.20) are examined. The charge carrier density  $n$ , mobility  $\mu$ , high-frequency dielectric constant  $\varepsilon_\infty$ , and free electron mass  $m^*$  are all materials properties. Although the chemical composition of the material determines the overall range that these parameters may take, there are a number of materials, such as the conductive metal oxides indium tin oxide (ITO) and aluminum zinc oxide (AZO), in which their plasmonic properties can be directly controlled by their film

deposition parameters [17]. In particular,  $n$  and  $\mu$  may be controlled over a modest range by such effects as the doping concentration, the concentration of oxygen vacancies, the film's grain size, etc. This effect has been called “tunable plasmonics,” in accordance with the fact that a desired surface plasmon response can be engineered over a several thousand wavenumber range for a given material.

### 1.1.2 Surface plasmons

Our discussion of plasmons evolves in a similar fashion as in Stefan Maier's book [1]. We begin by deriving the electromagnetic wave equations from Maxwell's equations, then introduce a material boundary which will provide the necessary conditions for the surface plasmon polariton (SPP) to exist. In the absence of current and charge, Maxwell's equations can be written as:

$$\nabla \cdot \mathbf{E} = 0 \quad (1.1.26)$$

$$\nabla \cdot \mathbf{B} = 0 \quad (1.1.27)$$

$$\nabla \times \mathbf{E} = -\frac{\partial \mathbf{B}}{\partial t} \quad (1.1.28)$$

$$\nabla \times \mathbf{B} = \mu_0 \mu \varepsilon_0 \varepsilon \frac{\partial \mathbf{E}}{\partial t} \quad (1.1.29)$$

Along with the relations:

$$\mathbf{D} = \varepsilon_0 \varepsilon \mathbf{E} = \varepsilon_0 \mathbf{E} + \mathbf{P} \quad (1.1.30)$$

$$\mathbf{B} = \mu_0 \mu \mathbf{H} = \mu_0 \mathbf{H} + \mu_0 \mathbf{M} \quad (1.1.31)$$

Taking the curl of (1.1.28) and combining with (1.1.29), and *vice-versa*, and setting  $\mu=1$ , the electromagnetic wave equations are obtained:

$$\nabla \times \nabla \times \mathbf{E} = -\mu_0 \varepsilon_0 \varepsilon \frac{\partial^2 \mathbf{E}}{\partial t^2} \quad (1.1.32)$$

$$\nabla \times \nabla \times \mathbf{B} = -\mu_0 \varepsilon_0 \varepsilon \frac{\partial^2 \mathbf{B}}{\partial t^2} \quad (1.1.33)$$

We introduce a vector identity:

$$\nabla \times \nabla \times \mathbf{A} = \nabla(\nabla \cdot \mathbf{A}) - \nabla^2 \mathbf{A} \quad (1.1.34)$$

Which may be used in (1.1.32) and (1.1.33) to produce:

$$\nabla(\nabla \cdot \mathbf{E}) - \nabla^2 \mathbf{E} = -\mu_0 \varepsilon_0 \varepsilon \frac{\partial^2 \mathbf{E}}{\partial t^2} \quad (1.1.35)$$

$$\nabla(\nabla \cdot \mathbf{B}) - \nabla^2 \mathbf{B} = -\mu_0 \varepsilon_0 \varepsilon \frac{\partial^2 \mathbf{B}}{\partial t^2} \quad (1.1.36)$$

Recognizing that the speed of light  $c = (\varepsilon_0 \mu_0)^{-1/2}$ ,

$$\nabla(\nabla \cdot \mathbf{E}) - \nabla^2 \mathbf{E} = -\frac{\varepsilon}{c^2} \frac{\partial^2 \mathbf{E}}{\partial t^2} \quad (1.1.37)$$

$$\nabla(\nabla \cdot \mathbf{B}) - \nabla^2 \mathbf{B} = -\frac{\varepsilon}{c^2} \frac{\partial^2 \mathbf{B}}{\partial t^2} \quad (1.1.38)$$

The time and space domains can also be converted to the Fourier domains of radial frequency and wavevector using a simple conversion:

$$\nabla \rightarrow i\mathbf{k} \quad (1.1.39)$$

$$\frac{\partial}{\partial t} \rightarrow -i\omega \quad (1.1.40)$$

The wave equations become:

$$-\mathbf{k}(\mathbf{k} \cdot \tilde{\mathbf{B}}) + k^2 \tilde{\mathbf{B}} = \varepsilon \frac{\omega^2}{c^2} \tilde{\mathbf{B}} \quad (1.1.41)$$

$$-\mathbf{k}(\mathbf{k} \cdot \tilde{\mathbf{E}}) + k^2 \tilde{\mathbf{E}} = \varepsilon \frac{\omega^2}{c^2} \tilde{\mathbf{E}}. \quad (1.1.42)$$

One solution to these equations is a longitudinal wave, where  $\mathbf{k} \times \tilde{\mathbf{E}} = 0$  or  $\mathbf{k} \times \tilde{\mathbf{B}} = 0$ , which occurs only when  $\varepsilon = 0$ . This is the bulk plasma oscillation, which cannot couple to transverse electromagnetic radiation but may still be excited in EELS [33].

The relevant solution for SPR is the transverse wave, where  $\mathbf{k} \cdot \tilde{\mathbf{E}} = 0$  and  $\mathbf{k} \cdot \tilde{\mathbf{B}} = 0$ . The wave equations become:

$$k^2 \tilde{\mathbf{E}} = \varepsilon \frac{\omega^2}{c^2} \tilde{\mathbf{E}} \quad (1.1.43)$$

$$k^2 \tilde{\mathbf{B}} = \varepsilon \frac{\omega^2}{c^2} \tilde{\mathbf{B}} \quad (1.1.44)$$

These may be generalized as:

$$\boxed{k^2 = \varepsilon \frac{\omega^2}{c^2}} \quad (1.1.45)$$

Equation (1.1.45) is a generalized dispersion relation for transverse waves in dielectric media. This equation is true for any non-magnetic medium without free charge or current, including conductors. We only need to substitute the dielectric function, given in equation (1.1.13), to obtain the radiative plasmon (RP) dispersion and discover that transverse waves are prohibited in metals at  $\omega < \omega_p$ . Thus, a surface plasmon cannot exist in a bulk material.

To form a surface plasmon polariton, it is necessary to introduce a boundary between the conductor B and a non-conductive medium A ( $\varepsilon_{1A} > 0$ ), and look for solutions to Maxwell's equations at this boundary. This boundary enables the plasmons to form a surface mode, which can take lower frequencies than  $\omega_p$ . To begin, the boundary is defined as existing in the x-y plane at  $z=0$ , with the conductor at  $z < 0$  and the non-conductor at  $z > 0$  (Fig. 1.3).

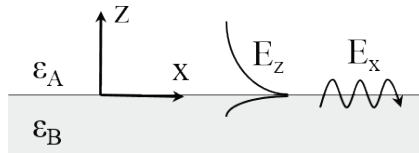


Figure 1.3: Schematic of the coordinate system along with pictorial representations of the  $x$  and  $z$  electric fields of a surface polariton in media A and B.

The solution to Maxwell's equations that we are interested in is the evanescent wave solution. The wave is defined as propagating in only the  $x$  direction at the interface, so that  $\mathbf{k} \cdot \mathbf{r} = k_x x$ , and decaying exponentially into both  $+z$  and  $-z$ . Although expressions may be written for both evanescent waves with the electric field in the plane of the interface (“ $s$ -polarized”) and waves with the magnetic field in the plane of the interface (“ $p$ -polarized”), it will soon become evident that only the  $p$ -polarized solutions will survive due to  $\mu=1$ . Beginning with the  $s$ -polarized case, we can write expressions for the fields above and below the interface:

$$\mathbf{E}_A = E_{yA} \hat{\mathbf{y}} \exp \{-i\omega t + ik_x x - k_{zA} z\} \quad (1.1.46)$$

$$\mathbf{H}_A = (H_{xA} \hat{\mathbf{x}} + H_{zA} \hat{\mathbf{z}}) \exp \{-i\omega t + ik_x x - k_{zA} z\} \quad (1.1.47)$$

$$\mathbf{E}_B = E_{yB} \hat{\mathbf{y}} \exp \{-i\omega t + ik_x x + k_{zB} z\} \quad (1.1.48)$$

$$\mathbf{H}_B = (H_{xB} \hat{\mathbf{x}} + H_{zB} \hat{\mathbf{z}}) \exp \{-i\omega t + ik_x x + k_{zB} z\}. \quad (1.1.49)$$

Then, using equations (1.1.28) and (1.1.31) and evaluating the derivatives:

$$E_{yA} k_{zA} \hat{\mathbf{x}} + ik_x E_{yA} \hat{\mathbf{z}} = i\omega \mu_0 \mu_A H_{xA} \hat{\mathbf{x}} + i\omega \mu_0 \mu_A H_{zA} \hat{\mathbf{z}} \quad (1.1.50)$$

$$-E_{yB} k_{zB} \hat{\mathbf{x}} + ik_x E_{yB} \hat{\mathbf{z}} = i\omega \mu_0 \mu_B H_{xB} \hat{\mathbf{x}} + i\omega \mu_0 \mu_B H_{zB} \hat{\mathbf{z}} \quad (1.1.51)$$

$$E_{yA} = H_{xA} \frac{i\omega \mu_0 \mu_A}{k_{zA}} \quad (1.1.52)$$

$$E_{yB} = -H_{xB} \frac{i\omega \mu_0 \mu_B}{k_{zB}} \quad (1.1.53)$$

The boundary conditions at any interface with no charge or current are:

$$\mathbf{D}_{\perp A} - \mathbf{D}_{\perp B} = \rho_s = 0 \quad (1.1.54)$$

$$\mathbf{E}_{\parallel A} - \mathbf{E}_{\parallel B} = 0 \quad (1.1.55)$$

$$\mathbf{B}_{\perp A} - \mathbf{B}_{\perp B} = 0 \quad (1.1.56)$$

$$\mathbf{H}_{\parallel A} - \mathbf{H}_{\parallel B} = \mathbf{J}_s = 0. \quad (1.1.57)$$

Applying (1.1.55) and (1.1.57):

$$E_{yA} = E_{yB} \quad (1.1.58)$$

$$H_{xA} = H_{xB} \quad (1.1.59)$$

$$\frac{\mu_A}{k_{zA}} = \frac{-\mu_B}{k_{zB}}. \quad (1.1.60)$$

For most materials with  $\mu > 0$ , equation (1.1.60) cannot be satisfied, and thus  $s$ -polarized light cannot normally be used to generate an SPP. Creating materials with negative magnetic permeability is possible, however [34], and thus “magnetic SPR” is physically possible, albeit rare.

Similarly, for the  $p$ -polarized case:

$$\mathbf{H}_A = H_{yA} \hat{\mathbf{y}} \exp\{-i\omega t + ik_x x - k_{zA} z\} \quad (1.1.61)$$

$$\mathbf{E}_A = (E_{xA} \hat{\mathbf{x}} + E_{zA} \hat{\mathbf{z}}) \exp\{-i\omega t + ik_x x - k_{zA} z\} \quad (1.1.62)$$

$$\mathbf{H}_B = H_{yB} \hat{\mathbf{y}} \exp\{-i\omega t + ik_x x + k_{zB} z\} \quad (1.1.63)$$

$$\mathbf{E}_B = (E_{xB} \hat{\mathbf{x}} + E_{zB} \hat{\mathbf{z}}) \exp\{-i\omega t + ik_x x + k_{zB} z\}. \quad (1.1.64)$$

Then, using equation (1.1.29) and evaluating the derivatives:

$$-H_{yA} k_{zA} \hat{\mathbf{x}} + ik_x H_{yA} \hat{\mathbf{z}} = -i\omega \epsilon_0 \epsilon_A E_{xA} \hat{\mathbf{x}} - i\omega \epsilon_0 \epsilon_A E_{zA} \hat{\mathbf{z}} \quad (1.1.65)$$

$$H_{yB} k_{zB} \hat{\mathbf{x}} + ik_x H_{yB} \hat{\mathbf{z}} = -i\omega \epsilon_0 \epsilon_B E_{xB} \hat{\mathbf{x}} - i\omega \epsilon_0 \epsilon_B E_{zB} \hat{\mathbf{z}} \quad (1.1.66)$$

$$E_{zA} = -H_{yA} \frac{k_x}{\omega \epsilon_0 \epsilon_A} \quad (1.1.67)$$

$$E_{zB} = -H_{yB} \frac{k_x}{\omega \epsilon_0 \epsilon_B} \quad (1.1.68)$$

$$E_{xA} = H_{yA} \frac{k_{zA}}{i\omega\epsilon_0\epsilon_A} \quad (1.1.69)$$

$$E_{xB} = -H_{yB} \frac{k_{zB}}{i\omega\epsilon_0\epsilon_B} \quad (1.1.70)$$

With the same boundary conditions (1.1.54) through (1.1.57):

$$E_{xA} = E_{xB} \quad (1.1.71)$$

$$H_{yA} = H_{yB} \quad (1.1.72)$$

$$\boxed{\frac{\epsilon_A}{k_{zA}} = \frac{-\epsilon_B}{k_{zB}}} \quad (1.1.73)$$

Since  $k_{zA}$  and  $k_{zB}$  are both positive, (1.1.73) implies that  $\epsilon_A$  and  $\epsilon_B$  must have opposite signs, *i.e.* a surface plasmon polariton can only exist at the interface of a conductor and a dielectric.

To obtain the dispersion relation of the SPP, the wave equation (1.1.43) may be used on the electric field expressions (1.1.62) and (1.1.64), giving:

$$k_{zA}^2 \mathbf{E}_A - k_x^2 \mathbf{E}_A = \epsilon_A \frac{\omega^2}{c^2} \mathbf{E}_A \quad (1.1.74)$$

$$k_{zB}^2 \mathbf{E}_B - k_x^2 \mathbf{E}_B = \epsilon_B \frac{\omega^2}{c^2} \mathbf{E}_B \quad (1.1.75)$$

An equivalent operation may also be performed on the magnetic fields. Using equation (1.1.73), these may be combined to produce the surface plasmon polariton dispersion relation:

$$\boxed{k_{SPP} = \frac{\omega}{c} \sqrt{\frac{\epsilon_A \epsilon_B}{\epsilon_A + \epsilon_B}}} \quad (1.1.76)$$

This wave has some unique properties that must be studied in more detail. First, we shall see that the SPP cannot be directly driven by light propagating through the material  $A$  that composes the interface. In order for this wave to be excited by light, it must be coupled with either an evanescent wave from total internal reflection, or via a grating. For an evanescent wave, the x-component of the wavevector is:

$$k_{ev} = \frac{\omega}{c} \sqrt{\varepsilon_C} \sin \theta \quad (1.1.77)$$

In a bulk material, light propagating through a material usually takes a dispersion relation of:

$$k_{bulk} = \frac{\omega}{c} \sqrt{\varepsilon_D} \quad (1.1.78)$$

These three dispersion relations, using air for  $\varepsilon_A$  and  $\varepsilon_D$ , indium tin oxide for  $\varepsilon_B$ , and BK-7 glass at  $60^\circ$  for  $\varepsilon_C$ , are plotted in Fig. 1.4. The SPP dispersion relation (1.1.76) is separated into real and imaginary parts and is for a real material with significant damping, which is what causes the complex shape of  $k_{SPP}$ . It is separated into three regions: 1) The upper radiative plasmon (RP) region. Here,  $real(\varepsilon_B) > 0$ ,  $imag(\varepsilon_B) \approx 0$ , and so the material is simply behaving as a dielectric. 2) The middle quasi-bound mode (QBM) region. This mode only exists due to damping ( $\Gamma > 0$ ), and so vanishes for a hypothetical material with infinite mobility. 3) The lower surface plasmon polariton (SPP) region. It is clear in Fig. 1.4 that the wavevector of light propagating through air does not match the wavevector of the SPP at any frequency. This is true no matter what material system we choose; as long as  $\varepsilon_A = \varepsilon_D$ , a SPP cannot be generated.

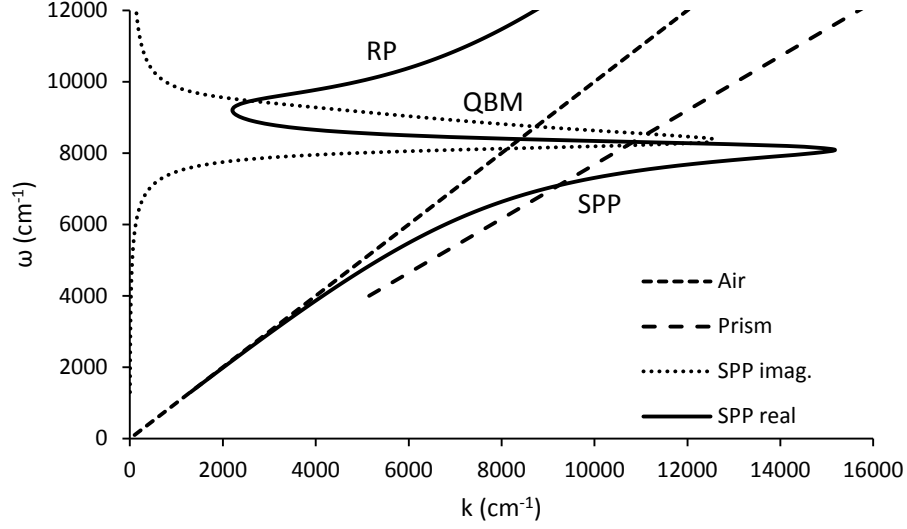


Figure 1.4: Dispersion relations for: light propagating through air (small dashes), light at a BK-7 prism interface at  $60^\circ$  (large dashes), the imaginary component of the waves at the conductor/air interface (dots), and the real component of the plasmon waves at the conductor/air interface (solid). The real component of the plasmon waves is separated into regions radiative plasmon (RP), quasi-bound mode (QBM), and surface plasmon polariton (SPP). The dispersion relation for light in air never crosses the SPP line.

On the other hand,  $k_x$  for an evanescent wave can be controlled by the angle of incidence, and thus can be made to match the SPP wavevector. In Fig. 1.4, which is for a generic conductor with the properties of indium tin oxide and an evanescent wave from BK-7 glass with a  $60^\circ$  angle of incidence, this is seen to occur at approximately  $7000 \text{ cm}^{-1}$ . Coupling can occur only at angles greater than the critical angle  $\theta_c$  between  $\epsilon_A$  and  $\epsilon_C$ , where:

$$\theta_c = \sin^{-1}\left(\frac{\sqrt{\epsilon_A}}{\sqrt{\epsilon_C}}\right) \quad (1.1.79)$$

and  $\epsilon_C > \epsilon_A$ . Ignoring grating coupling, which is out of the scope of this discussion, the consequence is that SPR can only exist when total internal reflection is present. Thus, another

material, such as a transparent prism or a fiber optic wire, is required, and the localized surface plasmon resonance (LSPR) that is commonly seen for colloidal particles (for which  $\varepsilon_A = \varepsilon_D$ ) must be a different plasmonic mode. Indeed, it can be shown that the LSPR arises due to the particle geometry and not due to direct coupling to the SPP as shown here. For particles much smaller than the light wavelength, the light's electric field can be approximated as quasi-static, which induces a dipole (or quadrupole, etc.) polarization over the particle's surface. Further discussion of this effect can be found in Maier *et al.* [1, 35].

### 1.1.3 SPR experimental considerations

Experimentally, there are two common configurations that make use of total internal reflection (TIR) to generate an SPP. One is the Otto configuration [29], in which a bulk metal is placed a short distance from the TIR interface, and the SPP propagates in the gap between the two. The other is the Kretschmann configuration (Fig. 1.5), in which a thin film of the conducting medium is deposited directly onto the TIR interface [30]. The Kretschmann configuration is significantly more popular than the Otto configuration, due to its ease of use. Most metal films are not difficult to deposit, using common methods such as magnetron sputtering or evaporation, although more specialized techniques may be required for different materials. Compared to the Otto configuration, the Kretschmann configuration also does not substantially limit the volume of the ambient medium. This feature is useful for biosensing experiments, as it permits devices like flow cells to be implemented with relatively few complications. The Kretschmann configuration is used in all of the experiments discussed in this dissertation.

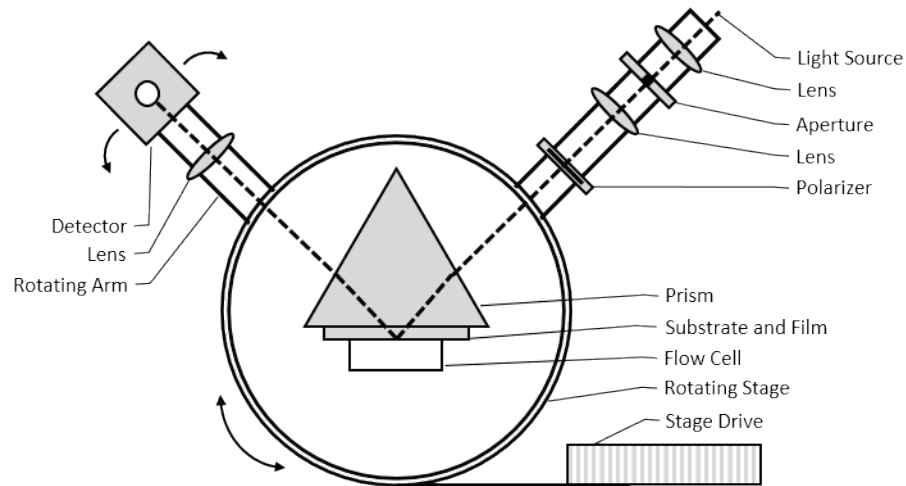


Figure 1.5: A diagram of the main optical elements in a typical Kretschmann-configuration SPR spectrometer.

In practice, the Kretschmann configuration is usually achieved by deposition of the conductor onto a flat slide or chip of the substrate, rather than directly onto a prism. This slide is then adhered to a prism using an index matching fluid, which is a liquid mixture designed to have a refractive index (RI) approximating that of the substrate. The effects of the index matching fluid on an SPR spectrum are usually minimal, and thus the system can be treated as a continuous unit. Index matching fluids are commercially available for a wide variety of substrates and frequencies. However, organic liquids with an RI higher than approximately 1.6 are rare. Elemental sulfur can be suspended to increase the RI to approximately 1.8, and arsenic tribromide up to approximately 2.3, although the higher RI fluids tend to be chemically reactive, volatile, and toxic. Materials with an RI higher than this, such as silicon (transparent in the infrared with  $n \approx 3.7$ ), present a unique challenge to the Kretschmann configuration, as no liquids exist with such a high RI. For SPR on silicon, then, the films may be deposited directly onto the prism or the slide may be placed in direct contact with the prism [36, 37]. The latter is presumably only possible for exceptionally flat materials, as any air gap between the two would result in total internal reflection from the air/prism boundary.

The spectrometers used herein use simultaneous angle and frequency interrogation to map the  $\omega - k$  space, which is accomplished by attaching a rotating  $\theta$ - $2\theta$  stage to a spectrometer. A cartoon of some of the optics used in a typical Kretschmann-configuration SPR spectrometer are seen in Fig. 1.5. The prism, matching fluid, and substrate with film are held together in a mechanical assembly, and this assembly is mounted on a rotating  $\theta$ - $2\theta$  stage. The light is routed through a linear polarizer before it enters the prism, and the data are collected as the ratio of  $p$ -polarized reflectance to  $s$ -polarized reflectance ( $R_p/R_s$ ). This ratio is taken to eliminate many of the non-SPR related effects, since only the  $p$ -polarized light may generate a surface plasmon, and many non-SPR related optical effects are not polarization dependent. These instruments are almost always modifications of other instruments; Fourier-transform infrared (FTIR) spectrometers are commonly used [20, 38, 39], as are Fourier-transform variable angle spectroscopic ellipsometers (VASEs) [12, 36]. These instruments produce an entire infrared spectrum at a given angle, and may be referred to as FT-SPR. An example of the output is presented in Fig. 1.6. This example spectrum is for a 160 nm thick film of indium tin oxide (ITO), on BK-7 glass ( $n_D=1.52$ ), using air as the ambient medium. Two main features are seen in this spectrum: the surface plasmon polariton (SPP), and the quasi-bound mode (QBM), which have the same meanings as in Fig. 1.4. The SPP excitation wavenumber is seen to be angle dependent, which corresponds to the changing wavevector of the x-component of the total internal reflected light. The QBM wavenumber is seen to be independent of angle, which is expected from the dispersion curve.

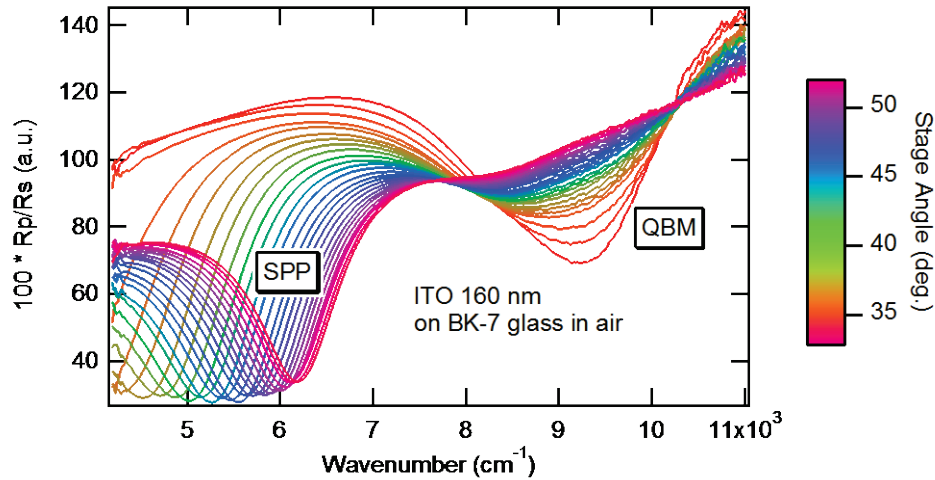


Figure 1.6: Example spectrum from a typical FT-SPR instrument at varying angles. Two excitations are seen: the surface plasmon polariton (SPP), and the quasi-bound mode (QBM).

There are a number of choices that become very important when designing SPR experiments. The simple presence of a conducting film on glass is not enough to guarantee that an SPR absorption will be seen. Factors that must be considered include: The film's identity, composition, and physical structure, which determine its conductive properties; the film's thickness, which must be within a certain range that depends on its conductive properties; and the refractive indices, transparencies, and dispersions of both the substrate and ambient materials, which determine the frequencies at which the wavevector matching will occur, and thus must be matched to the instrument's angle and frequency range. This is a complex problem that is best solved using mathematical modeling of the SPR reflectance.

## 1.2 Thin film optics

Surface plasmon resonance is an optical phenomenon, and may be explained in great detail by relatively simple optical theories. In this section, we will use the label convention as in Fig. 1.3, with the physical substrate as layer C, the film system as layer(s) B, and the external

ambient as layer A. For multiple films, we will use B1, B2, etc. and label the interfaces with numbers (Fig. 1.7). In addition, it will be necessary to specify the incident and reflected waves with superscript positive and negative symbols on both E and H.

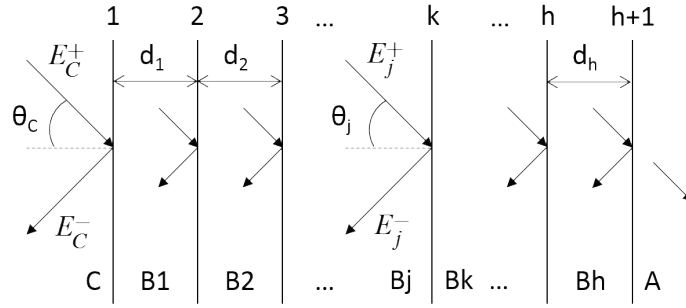


Figure 1.7: Notation convention for a system of  $h$  thin films bounded by materials  $A$  and  $C$ .

### 1.2.1 Fresnel equations for reflectance from a single thin film

For a single thin film  $B$ , the conventional method to obtain the reflectance is to use the Airy equations, sometimes referred to as the Fresnel equations (not to be confused with the Fresnel coefficients on which they are based), for reflectance from a thin film. These expressions are derived in many textbooks [40-42], and so are presented here without derivation, for reference and comparison. We begin with the Fresnel coefficients for reflection  $r$  and transmission  $t$  amplitudes at the interface  $CB$ . For  $p$ -polarized light:

$$r_{CB,p} = \frac{\varepsilon_C n_B \cos \theta_B - \varepsilon_B n_C \cos \theta_C}{\varepsilon_C n_B \cos \theta_B + \varepsilon_B n_C \cos \theta_C} \quad (1.2.1)$$

$$t_{CB,p} = \frac{2n_B n_C^2 \cos \theta_C}{\varepsilon_C n_B \cos \theta_B + \varepsilon_B n_C \cos \theta_C} \quad (1.2.2)$$

and for  $s$ -polarized light:

$$r_{CB,s} = \frac{n_C \cos \theta_C - n_B \cos \theta_B}{n_C \cos \theta_C + n_B \cos \theta_B} \quad (1.2.3)$$

$$t_{CB,s} = \frac{2n_C \cos \theta_C}{n_C \cos \theta_C + n_B \cos \theta_B} \quad (1.2.4)$$

where  $\theta_j$  is the angle of incidence, relative to the interface normal, in each medium  $j$ , and  $n_j$  is the refractive index of each medium  $j$  surrounding the interface. Equivalent expressions can be written for the  $BA$  interface. The Airy equation is built algebraically from these, and follows:

$$r_{CBA} = \frac{r_{CB} + r_{BA} \exp\{-2i\delta_B\}}{1 + r_{CB}r_{BA} \exp\{-2i\delta_B\}} \quad (1.2.5)$$

where the appropriate Fresnel coefficient may be selected for  $p$ - or  $s$ -polarization, and where

$$\delta_B = \frac{\omega}{c} d_B n_B \cos \theta_B. \quad (1.2.6)$$

and  $d_B$  is the thickness of layer  $B$ . The reflected energy, which is the experimentally measured quantity, is the square modulus of the amplitude:

$$R = |r|^2 \quad (1.2.7)$$

Since conductive media have complex refractive indices, the angle  $\theta_B$  is complex-valued. Although this is not a problem mathematically, some computer software cannot handle certain operations on complex angles. It is convenient, then, to express this angle in terms of the angle inside the first medium, which is real (the first medium is considered infinite in extent and therefore must be transparent for light to reach the conductor). Using Snell's law, we can define a convenient admittance quantity  $\gamma_j$  which avoids the complex angle, and which is true for all layers  $j$ :

$$\gamma_j \equiv n_j \cos \theta_j = (\varepsilon_j - \varepsilon_C \sin^2 \theta_C)^{\frac{1}{2}}, \quad (1.2.8)$$

The combination of equations (1.2.1) through (1.2.8), along with the Drude dielectric function for the conductor  $\epsilon_B$  given in equation (1.1.13), and the known dielectric functions of the substrate and ambient  $\epsilon_A$  and  $\epsilon_C$ , is used to produce  $R_p/R_s$ . This theory is sufficient to describe the SPR response of most single-film experiments. It is convenient for its simplicity and speed, and can be used for a large number of systems. However, when more than one thin film is involved, equation (1.2.5) is not applicable, and more complicated expressions must be derived, which quickly become cumbersome in their size and complexity. In that case, it is easier to use the transfer-matrix method, which is easily extendible to any number of films and is mathematically equivalent to the non-matrix forms of the optical equations.

### 1.2.2 Matrix method for reflectance from a system of thin films

For multiple films, we turn to a similar theory in which the reflectance is constructed from a series of  $2 \times 2$  matrices. There are several references that discuss this matrix method for a system of thin films [41-43]. In addition, a software package for Matlab has been made freely available on the Mathworks File Exchange site [44]. First, the film system is defined as in Fig. 1.7, with  $h$  number of films on substrate  $C$ , bounded by ambient material  $A$ . At any given interface  $k$ , the boundary conditions must be satisfied, which are the same as in section 1.1.2:

$$\mathbf{E}_{\parallel j} - \mathbf{E}_{\parallel k} = 0 \quad (1.2.9)$$

$$\mathbf{H}_{\parallel j} - \mathbf{H}_{\parallel k} = \mathbf{J}_s = 0. \quad (1.2.10)$$

For the tangential fields, we can write the expressions using the complex amplitudes (which contain the position- and time-dependent exponential components) as follows. For  $s$ -polarized light, the electric field is in  $y$  and the magnetic field is in  $(-x, z)$ , so that:

$$E_j^+ + E_j^- = E_k^+ + E_k^- \quad (1.2.11)$$

$$-n_j \cos \theta_j (E_j^+ - E_j^-) = -n_k \cos \theta_k (E_k^+ - E_k^-) \quad (1.2.12)$$

Similarly, for  $p$ -polarized light, the electric field is in  $(x, -z)$  and the magnetic field is in  $y$ , so that:

$$\cos \theta_j (E_j^+ + E_j^-) = \cos \theta_k (E_k^+ + E_k^-) \quad (1.2.13)$$

$$n_j (E_j^+ - E_j^-) = n_k (E_k^+ - E_k^-). \quad (1.2.14)$$

Note that the sign change for the reflected waves indicates the phase change on reflection. These four equations (1.2.11) through (1.2.14) can be written in matrix form:

$$V_j \begin{pmatrix} E_j^+ \\ E_j^- \end{pmatrix} = V_k \begin{pmatrix} E_k^+ \\ E_k^- \end{pmatrix} \quad (1.2.15)$$

where

$$V_j^s = \begin{pmatrix} 1 & 1 \\ n_j \cos \theta_j & -n_j \cos \theta_j \end{pmatrix} \quad (1.2.16)$$

for  $s$ -polarized light, and

$$V_j^p = \begin{pmatrix} \cos \theta_j & \cos \theta_j \\ n_j & -n_j \end{pmatrix} \quad (1.2.17)$$

for  $p$ -polarized light. These equations may also be written as:

$$\begin{pmatrix} E_j^+ \\ E_j^- \end{pmatrix} = V_j^{-1} V_k \begin{pmatrix} E_k^+ \\ E_k^- \end{pmatrix} = T_{jk} \begin{pmatrix} E_k^+ \\ E_k^- \end{pmatrix}, \quad (1.2.18)$$

where the transfer matrix  $T$  has been introduced, so that we can write:

$$T_{jk}^s = \frac{1}{2} \begin{pmatrix} 1 & (n_j \cos \theta_j)^{-1} \\ 1 & (-n_j \cos \theta_j)^{-1} \end{pmatrix} \begin{pmatrix} 1 & 1 \\ n_k \cos \theta_k & -n_k \cos \theta_k \end{pmatrix} \quad (1.2.19)$$

$$T_{jk}^p = \frac{1}{2} \begin{pmatrix} (\cos \theta_j)^{-1} & n_j^{-1} \\ (\cos \theta_j)^{-1} & -n_j^{-1} \end{pmatrix} \begin{pmatrix} \cos \theta_k & \cos \theta_k \\ n_k & -n_k \end{pmatrix}, \quad (1.2.20)$$

which, when evaluated, give:

$$T_{jk}^s = \frac{1}{2} \begin{pmatrix} 1 + \gamma_k / \gamma_j & 1 - \gamma_k / \gamma_j \\ 1 - \gamma_k / \gamma_j & 1 + \gamma_k / \gamma_j \end{pmatrix} \quad (1.2.21)$$

$$T_{jk}^p = \frac{1}{2} \begin{pmatrix} 1 + \varepsilon_j \gamma_k / \varepsilon_k \gamma_j & 1 - \varepsilon_j \gamma_k / \varepsilon_k \gamma_j \\ 1 - \varepsilon_j \gamma_k / \varepsilon_k \gamma_j & 1 + \varepsilon_j \gamma_k / \varepsilon_k \gamma_j \end{pmatrix}. \quad (1.2.22)$$

Here, the definition of  $\gamma_j$  is the same as before:

$$\gamma_j \equiv n_j \cos \theta_j = (\varepsilon_j - \varepsilon_c \sin^2 \theta_c)^{\frac{1}{2}}. \quad (1.2.23)$$

Thus far, the phases of the fields have been incorporated into the complex amplitudes. The exact phase at the first interface is not important and can be left incorporated. However, the phase change as the radiation traverses from one interface to another must not be neglected. For example, accounting for the phase change across layer  $k$  produces, for the tangential components of the electric field:

$$E_k(d_k) = E_k^+ \exp\{+i\delta_k\} + E_k^- \exp\{-i\delta_k\} \quad (1.2.24)$$

where the definition of  $\delta$  is the same as before:

$$\delta_j = \frac{\omega}{c} d_j \gamma_j. \quad (1.2.25)$$

This phase change can be generalized to any of the fields, as a phase matrix  $P$ :

$$P_j = \begin{pmatrix} \exp\{+i\delta_j\} & 0 \\ 0 & \exp\{-i\delta_j\} \end{pmatrix} \quad (1.2.26)$$

The total field amplitudes are then obtained by repeated multiplication of the transfer matrices (1.2.21) or (1.2.22) with the phase matrix (1.2.26) for the total number of layers in the system:

$$\begin{pmatrix} E_1^+ \\ E_1^- \end{pmatrix} = T_{01} P_1 T_{12} \cdots P_h T_{h,h+1} \begin{pmatrix} E_{h+1}^+ \\ E_{h+1}^- \end{pmatrix}. \quad (1.2.27)$$

The center product in (1.2.27) is a square matrix  $M$  known as the system transfer matrix:

$$M = \begin{pmatrix} a_{11} & a_{12} \\ a_{21} & a_{22} \end{pmatrix} = T_{01} P_1 T_{12} \cdots P_h T_{h,h+1}. \quad (1.2.28)$$

The total reflected amplitude for the entire system is given from  $M$  by:

$$r = \frac{a_{21}}{a_{11}}, \quad (1.2.29)$$

and the reflected energy is the square modulus of this amplitude, as in (1.2.7). For SPR this must be calculated twice, once for  $p$ -polarized light and once for  $s$ -polarized light, to obtain  $R_p/R_s$ .

### 1.3 References

1. S. A. Maier, *Plasmonics: fundamentals and applications* (Springer, New York, 2007).
2. L. Novotny, and B. Hecht, *Principles of nano-optics* (Cambridge University Press, Cambridge, 2006).
3. P. Vadgama, *Surfaces and interfaces for biomaterials* (CRC Press, Boca Raton, FL, 2005).
4. D. Sarid, and W. A. Challener, *Modern introduction to surface plasmons: theory, Mathematica modeling, and applications* (Cambridge University Press, Cambridge ; New York, 2010).
5. J. Pitarke, V. Silkin, E. Chulkov, and P. Echenique, "Surface plasmons in metallic structures," *Journal of Optics A: Pure and Applied Optics* **7**, S73-S84 (2005).
6. V. M. Agranovich, and D. L. Mills, *Surface polaritons: electromagnetic waves at surfaces and interfaces* (North-Holland, New York, 1982).
7. S. I. Bozhevolnyi, *Plasmonic nanoguides and circuits* (Pan Stanford, Hackensack, NJ, 2009).
8. M. L. Brongersma, and P. G. Kik, *Surface plasmon nanophotonics* (Springer, Dordrecht, 2007).

9. R. Zia, M. Selker, P. Catrysse, and M. Brongersma, "Geometries and materials for subwavelength surface plasmon modes," *Journal of the Optical Society of America A* **21**, 2442-2446 (2004).
10. J. Homola, S. Yee, and G. Gauglitz, "Surface plasmon resonance sensors: review," *Sensors and Actuators B-Chemical* **54**, 3-15 (1999).
11. J. Homola, "Present and future of surface plasmon resonance biosensors," *Analytical and Bioanalytical Chemistry* **377**, 528-539 (2003).
12. E. Sachet, M. Losego, J. Guske, S. Franzen, and J. Maria, "Mid-infrared surface plasmon resonance in zinc oxide semiconductor thin films," *Applied Physics Letters* **102**, 051111 (2013).
13. J. Guske, J. Brown, A. Welsh, and S. Franzen, "Infrared surface plasmon resonance of AZO-Ag-AZO sandwich thin films," *Optics Express* **20**, 23215-23226 (2012).
14. M. Losego, J. Guske, A. Efremenko, J. Maria, and S. Franzen, "Characterizing the Molecular Order of Phosphonic Acid Self-Assembled Monolayers on Indium Tin Oxide Surfaces," *Langmuir* **27**, 11883-11888 (2011).
15. S. Franzen, C. Rhodes, M. Cerruti, R. Gerber, M. Losego, J. Maria, and D. Aspnes, "Plasmonic phenomena in indium tin oxide and ITO-Au hybrid films," *Optics Letters* **34**, 2867-2869 (2009).
16. R. Gerber, D. Leonard, and S. Franzen, "Conductive thin film multilayers of gold on glass formed by self-assembly of multiple size gold nanoparticles," *Thin Solid Films* **517**, 6803-6808 (2009).
17. M. Losego, A. Efremenko, C. Rhodes, M. Cerruti, S. Franzen, and J. Maria, "Conductive oxide thin films: Model systems for understanding and controlling surface plasmon resonance," *Journal of Applied Physics* **106**, 024903 (2009).

18. S. Franzen, "Surface plasmon polaritons and screened plasma absorption in indium tin oxide compared to silver and gold," *Journal of Physical Chemistry C* **112**, 6027-6032 (2008).
19. C. Rhodes, S. Lappi, D. Fischer, S. Sambasivan, J. Genzer, and S. Franzen, "Characterization of monolayer formation on aluminum-doped zinc oxide thin films," *Langmuir* **24**, 433-440 (2008).
20. C. Rhodes, M. Cerruti, A. Efremenko, M. Losego, D. Aspnes, J. Maria, and S. Franzen, "Dependence of plasmon polaritons on the thickness of indium tin oxide thin films," *Journal of Applied Physics* **103**, 093108 (2008).
21. M. Cerruti, C. Rhodes, M. Losego, A. Efremenko, J. Maria, D. Fischer, S. Franzen, and J. Genzer, "Influence of indium-tin oxide surface structure on the ordering and coverage of carboxylic acid and thiol monolayers," *Journal of Physics D-Applied Physics* **40**, 4212-4221 (2007).
22. C. Rhodes, S. Franzen, J. Maria, M. Losego, D. Leonard, B. Laughlin, G. Duscher, and S. Weibel, "Surface plasmon resonance in conducting metal oxides," *Journal of Applied Physics* **100**, 054905 (2006).
23. S. Brewer, A. Allen, S. Lappi, T. Chasse, K. Briggman, C. Gorman, and S. Franzen, "Infrared detection of a phenylboronic acid terminated alkane thiol monolayer on gold surfaces," *Langmuir* **20**, 5512-5520 (2004).
24. S. Brewer, and S. Franzen, "Indium tin oxide plasma frequency dependence on sheet resistance and surface adlayers determined by reflectance FTIR spectroscopy," *Journal of Physical Chemistry B* **106**, 12986-12992 (2002).
25. S. Brewer, and S. Franzen, "Optical properties of indium tin oxide and fluorine-doped tin oxide surfaces: correlation of reflectivity, skin depth, and plasmon frequency with conductivity," *Journal of Alloys and Compounds* **338**, 73-79 (2002).

26. R. Wood, "On a remarkable case of uneven distribution of light in a diffraction grating spectrum," *Philosophical Magazine* **4**, 396-402 (1902).
27. R. Ritchie, "The interaction of swift electrons with surface excitations," *Journal of Physics-Condensed Matter* **5**, A17-A24 (1993).
28. A. Otto, "Optical excitation of nonradiative surface plasma waves," *Physica Status Solidi* **42**, K37-K39 (1970).
29. A. Otto, "Excitation of nonradiative surface plasma waves in silver by method of frustrated total reflection," *Zeitschrift Fur Physik* **216**, 398-410 (1968).
30. E. Kretschmann, and H. Raether, "Radiative decay of non radiative surface plasmons excited by light," *Zeitschrift Fur Naturforschung Part A-Astrophysik Physik Und Physikalische Chemie A* **23**, 2135 (1968).
31. M. Ordal, L. Long, R. Bell, S. Bell, R. Bell, R. Alexander, and C. Ward, "Optical properties of the metals Al, Co, Cu, Au, Fe, Pb, Ni, Pd, Pt, Ag, Ti, and W in the infrared and far infrared," *Applied Optics* **22**, 1099-1119 (1983).
32. P. Johnson, and R. Christy, "Optical Constants of the Noble Metals," *Physical Review B* **6**, 4370-4379 (1972).
33. J. Howard, "Introduction to Plasma Physics," (Lecture Notes, 2002).
34. Y.-C. Lai, C.-K. Chen, T.-Y. Huang, I.-W. Un, Y.-H. Yang, and T.-J. Yen, "Enriching the Symmetry of Maxwell Equations through Unprecedented Magnetic Responses of Artificial Metamaterials and Their Revolutionary Applications," *Symmetry* **3**, 283-304 (2011).
35. S. Maier, and H. Atwater, "Plasmonics: Localization and guiding of electromagnetic energy in metal/dielectric structures," *Journal of Applied Physics* **98** (2005).

36. S. Patskovsky, A. V. Kabashin, M. Meunier, and J. H. Luong, "Sensing properties of surface plasmon resonance in different multilayer Si-based structures," in *Photonics North* (International Society for Optics and Photonics, 2004), pp. 467-473.
37. S. Patskovsky, A. Kabashin, M. Meunier, J. Luong, T. VoDinh, W. Grundfest, D. Benaron, and G. Cohn, "Surface plasmon resonance sensor with silicon-based prism coupling," *Advanced Biomedical and Clinical Diagnostic Systems* **4958**, 144-148 (2003).
38. N. Menegazzo, L. Kegel, Y. Kim, D. Allen, and K. Booksh, "Adaptable infrared surface plasmon resonance spectroscopy accessory," *Review of Scientific Instruments* **83** (2012).
39. N. Menegazzo, L. Kegel, Y. Kim, and K. Booksh, "Characterization of a Variable Angle Reflection Fourier Transform Infrared Accessory Modified for Surface Plasmon Resonance Spectroscopy," *Applied Spectroscopy* **64**, 1181-1186 (2010).
40. M. Born, E. Wolf, and A. B. Bhatia, *Principles of optics: electromagnetic theory of propagation, interference and diffraction of light* (Cambridge University Press, New York, 1999).
41. O. S. Heavens, *Optical properties of thin solid films* (Butterworths Scientific Publications, London,, 1955).
42. Z. E. Knittl, *Optics of thin films; an optical multilayer theory* (Wiley, London, New York,, 1976).
43. H. A. Macleod, *Thin-film optical filters* (CRC Press/Taylor & Francis, Boca Raton, FL, 2010).
44. J. T. Guske, "SPR XPhase," (2013),  
<http://www.mathworks.com/matlabcentral/fileexchange/41090>.

## **2. Reprint: Infrared surface plasmon resonance of AZO-Ag-AZO sandwich thin films**

J. T. Guske, J. Brown, A. Welsh, and S. Franzen. "Infrared surface plasmon resonance of AZO-Ag-AZO sandwich thin films," *Optics Express* **20** (21), 23215-23226 (2012)

This paper was published in *Optics Express* and is made available as an electronic reprint with the permission of OSA. The paper can be found at the following URL on the OSA website: <http://www.opticsinfobase.org/oe/abstract.cfm?uri=oe-20-21-23215>. Systematic or multiple reproduction or distribution to multiple locations via electronic or other means is prohibited and is subject to penalties under law.

# Infrared surface plasmon resonance of AZO-Ag-AZO sandwich thin films

Joshua T. Guske,<sup>1</sup> Jeff Brown,<sup>2</sup> Alex Welsh,<sup>2</sup> and Stefan Franzen<sup>1,\*</sup>

<sup>1</sup>*Department of Chemistry, North Carolina State University  
2620 Yarbrough Drive, Raleigh, North Carolina 27695-8204, USA*

<sup>2</sup>*Acree Technologies, Inc.  
1980 Olivera Rd. Suite D, Concord, California 94520, USA*

*\*[Stefan.Franzen@ncsu.edu](mailto:Stefan.Franzen@ncsu.edu)*

**Abstract:** Near-infrared surface plasmon resonance (SPR) spectra were collected of thin multilayer films of aluminum-doped zinc oxide (AZO) / silver (Ag) / AZO on BK-7 glass in the Kretschmann configuration in air, with the silver layer thickness varying from 5 nm to 50 nm. The SPR results were interpreted by modeling the reflectance with a five-layer transfer-matrix method, with the aid of a simplex algorithm. The model indicated that the Ag plasma frequency was significantly higher than the bulk value, possibly due to Schottky effect charge transfer from the AZO to the Ag layer. Continuous silver films were made as thin as 10 nm, indicating an inhibition of metal island formation for Ag deposited on AZO.

©2012 Optical Society of America

**OCIS codes:** (240.0310) Thin Films; (240.6680) Surface Plasmons; (250.5403) Plasmonics; (310.0310) Thin Films; (310.6860) Thin Films, Optical Properties.

## 2.1 Introduction

Surface plasmon resonance (SPR) for biosensing has traditionally been performed on noble metal surfaces such as gold and silver. These have a few advantages over other kinds of metals: they display SPR bands in both the visible and near-infrared frequencies, their surface chemistry is well-characterized and they are easily functionalized, and films are

readily prepared by a variety of deposition methods. However, noble metal films suffer from a number of disadvantages. First, they are mechanically fragile and are easily degraded by handling. Second, they tend to form discrete islands, rather than a continuous film, when the film thickness is less than a critical value. Third, silver films tarnish rapidly in ambient conditions. Because of these problems, there has been a drive to produce SPR-compatible films that are chemically and mechanically robust. One alternative is to use new materials; SPR has been demonstrated on highly conducting indium tin oxide (ITO) [1-6], titanium nitride [7], various metals [8, 9], and transition metal silicides [10]. Several other materials such as graphene are under consideration [9]. Another alternative is to use layers of other materials to mediate the undesired behavior. Layers underneath the SPR-active film can reduce the onset of island formation [11, 12], and layers above can improve the chemical and mechanical stability [13-22]. The latter approach will be discussed herein.

### *2.1.1 Sandwich thin films*

The thin films used in this study can be described as “sandwich” films, with an ABA layer structure. For typical sandwich films described in the literature, A is an insulating or weakly conducting transparent metal oxide or similar compound, such as ZnO, In<sub>2</sub>O<sub>3</sub>, ZnS, SnO<sub>2</sub>, or TiO<sub>2</sub>. Doped variants, such as ITO, are also used. The B layer is metal, typically Ag, Al, Au, or Cu. Films like these were originally developed for heat-reflecting transparent window coatings [23-30], where they provide greater heat reflection than single films of conducting metal oxides and greater transparency than single films of metals [31]. Sandwich films have also seen widespread use as transparent electrodes for electronic devices [32-41], where they provide a much lower resistivity than can be achieved with conducting metal oxides alone, while maintaining comparable transparency. Similar structures are also used for plasmonic waveguides [42, 43].

Another advantage of using the sandwich layer structure is in the prevention of island formation. Most transition metals, when deposited on insulating substrates, form a discontinuous film with an island-like structure when the amount of deposited material is less than a critical value. On bare glass substrates, silver does not form a continuous film less than

approximately 25 nm thick, but if an AZO base layer is included, silver can form continuous films as thin as 10 nm [11]. This behavior can be interpreted as the wetting or non-wetting of the substrate surface by the metal. Greater wetting (a lower contact angle) means the metal film will transition from island-like to continuous at lower coverage, so that continuous films can be made thinner. As a result, there has been a considerable amount of research concerning the conditions that favor wetting. For a given metal, wetting is improved on less insulating substrates [44]. More specifically, as the substrate's band gap ( $E_g$ ) decreases, plasma frequency increases, and high frequency dielectric constant ( $\epsilon_\infty$ ) increases, the work of adhesion increases and wetting improves, most likely due to increased charge transfer between the metal and the substrate [45, 46]. Thus, metal island formation is inhibited on the low band gap, moderately high dielectric constant ZnO ( $E_g=3.3$  eV and  $\epsilon_\infty=4.1$ ) compared to, for example, SiO<sub>2</sub> ( $E_g=8.9$  eV and  $\epsilon_\infty=2.4$ ),  $\alpha$ -Al<sub>2</sub>O<sub>3</sub> ( $E_g=8.9$  eV and  $\epsilon_\infty=2.9$ ), and MgO ( $E_g=7.8$  eV and  $\epsilon_\infty=2.95$ ) [44, 45]. Island formation is expected to also be inhibited on doped ZnO (*e.g.* AZO, GZO) compared to pure ZnO, as the dopants increase the plasma frequency [47]. Note that transition metal seeding can also improve wetting [11, 44, 48, 49], without increasing the film transmissivity.

To date we have not found any reports of an SPR study on sandwich films. However, there are multiple reports of SPR with a single overlayer. Bao *et al.* [13] reported SPR sensing on 55 nm Ag films with variable thickness ZnO overlayers. Other kinds of overlayers have also been used for SPR sensors, including a silicon-carbon alloy [14], ITO [15], amorphous carbon [16, 17], antimony-doped SnO<sub>2</sub> [18, 19], and silicates [20-22]. In addition, the approach we have taken to extracting information from the SPR spectra by modeling appears to be unique.

### 2.1.2 *Surface plasmon resonance*

Surface plasmon resonance (SPR) is a phenomenon in which electrons oscillate at the interface between a conducting and a dielectric medium. When this oscillation is driven by electromagnetic radiation, an electromagnetic wave called the Surface Plasmon Polariton (SPP) is generated, which can be understood as an electromagnetic wave that has been

confined to the conducting surface, decaying exponentially into both of the surrounding media. The wavevector of the SPP is highly dependent on the electronic properties of the conductor used, and on the refractive index of the material close to the interface. Because of this, SPR has been used in numerous applications that detect a change in the index of refraction of one of the two materials. The most prominent example is the use of SPR for biosensing, in which binding of biomolecules to the surface causes a small change in the refractive index of the dielectric medium near the interface, which can be detected by a change in the reflectivity from the metal surface. Several review articles and book chapters have been published on this topic [50-53].

In this paper, we have used Kretschmann's geometry [54, 55], in which a thin conducting film is attached to a glass prism, and the light strikes the film through the prism. This configuration is well-suited for biosensing work, as it permits a relatively high-volume flow cell to be attached on top of the SPR-active conducting material. However, the goal of the current study was not to demonstrate biosensing capability, but to assess the optical and material effects of the sandwich thin film configuration.

## **2.2 Materials and methods**

### *2.2.1 Film deposition*

Three-layer films of AZO, Ag, and AZO were deposited on glass microscope slides ultrasonically cleaned in acetone for 5 min. prior to use. To achieve high quality thin Ag films it is beneficial to employ a seed layer. ZnO is well known as an excellent seed layer to promote the growth of adherent, crystalline films of Ag [12]. AZO was chosen instead of undoped ZnO for this work to facilitate sputtering. The top layer of AZO was included as a preventative measure against agglomeration of the Ag films into islands when exposed to atmosphere.

The AZO films were deposited from a 99.99% purity metallic Al:Zn target (4% atomic Al) and the Ag films from a 99.99% purity Ag targets. Prior to all depositions the chamber base pressure was below  $1 \times 10^{-6}$  mTorr using a cryogenic pump. All layers were deposited without any heating of the substrate, other than what is provided by the sputtering process.

The microscope slides were rotated to achieve improved uniformity with the magnetrons positioned 5" from the substrate platen. The AZO layers were deposited using a 2" magnetron by pulsed DC magnetron sputtering at 50 W at a frequency of 200 kHz and positive pulse time of 1.6  $\mu$ s with 5 mTorr Ar and 0.40 mTorr O<sub>2</sub>. Four point probe and Hall Effect testing found the AZO films to be highly resistive for the thicknesses employed in this testing. The Ag films were deposited from a 3" magnetron with 150 W applied DC power at 5 mTorr Ar. A shutter in front of the substrate allowed both targets to be presputtered for >2 minutes prior to film deposition. The layer thicknesses were estimated based on a combination of deposition rate measured by QCM, total thickness measured by profilometry, and optical modeling of individual films in TFCalc.

### 2.2.2 SPR analysis

The films were analyzed via a Kretschmann geometry SPR setup in the near infrared. The film substrate was attached to a 60° triangular BK-7 glass prism ( $n_D=1.517$ ;  $n=1.506$  at  $\lambda=1$   $\mu$ m) using index matching fluid ( $n_D=1.520$ , Cargille Laboratories Inc.). The prism/film assembly was mounted in a custom-built SPR unit (GWC Technologies, Inc.) attached to an FTIR spectrometer (Thermo Scientific). The light from the instrument was routed through a CaF<sub>2</sub> beamsplitter, through a linear polarizer, reflected by the film in the Kretschmann configuration on a  $\theta$ - $2\theta$  stage, and detected by an extended-range InGaAs detector. Angle of incidence and polarization were controlled manually. The instrument software collected 32 scans at 32  $\text{cm}^{-1}$  resolution within the spectral range 4200  $\text{cm}^{-1}$  to 11000  $\text{cm}^{-1}$  wavenumber (2.38  $\mu$ m to 0.909  $\mu$ m wavelength) at each angle of incidence. The spectra are presented on the left side of Figs. 2.1 and 2.2 as  $p$ -polarized reflectance divided by  $s$ -polarized reflectance ( $R_p/R_s$ ). No other spectral processing or manipulation has been performed on the experimental spectra.

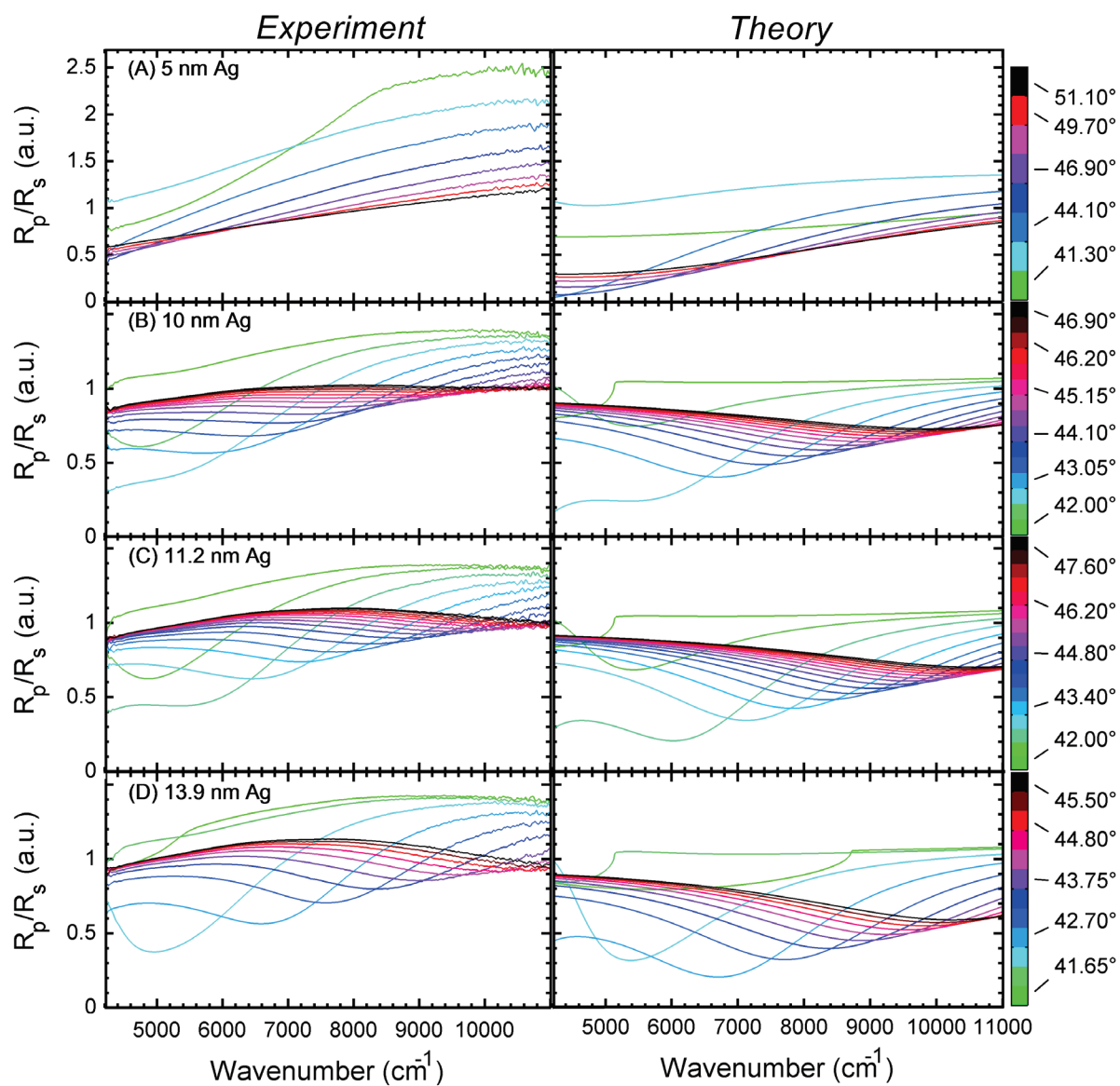


Figure 2.1: Experimental (left) and theoretical (right) FTIR-SPR spectra from 4200  $\text{cm}^{-1}$  to 11000  $\text{cm}^{-1}$  (2.38  $\mu\text{m}$  to 0.909  $\mu\text{m}$ ) for (A) the 23 nm AZO / 5 nm Ag / 23 nm AZO film, (B) the 23 nm AZO / 10 nm Ag / 23 nm AZO film, (C) the 23 nm AZO / 11.2 nm Ag / 23 nm AZO film, and (D) the 42.0 nm AZO / 13.9 nm Ag / 22.4 nm AZO film. The summary for all films is shown in Table 2.1.

**Table 2.1: Summary of fitted parameters for the AZO/Ag/AZO films.**

<b>AZO/Ag/AZO</b>				
<b>thicknesses (nm)</b>		$\omega_p$ (cm <sup>-1</sup> )		
<b>±standard deviation</b>	$\epsilon_\infty$	<sup>1)</sup>	$\Gamma$ (cm <sup>-1</sup> )	$\epsilon_{AZO}$
23 / 5.0 / 23 ±5.0%	15.46	78932	1647	1.758
23 / 10.0 / 23 ±2.5%	23.44	87588	436.1	1.489
23 / 11.2 / 23 ±2.3%	26.02	88563	482.1	1.672
42.0 / 13.9 / 22.4 ±1.8%	20.87	80906	564.7	1.340
21.9 / 15.8 / 48.5 ±1.6%	29.04	83699	453.8	1.953
27.5 / 20.0 / 27.1 ±1.3%	23.06	77634	492.5	1.543
23 / 30.0 / 23 ±1.0%	39.57	94524	626.5	1.957
23 / 50.0 / 23 ±1.0%	45.23	100918	498.2	2.297
Average:	27.84	86596	650.1	1.751
Bulk Ag:	3.158	72053	390.6	

## 2.3 Modeling

### 2.3.1 SPR spectra

Computer simulations of the spectra were performed in Matlab, using a multilayer transfer-matrix formalism [56, 57] for reflectance from a 5-layer model (Glass / AZO / Ag / AZO / Air). The model assumes the layers are homogeneous parallel planes, and that there are no magnetic effects. The glass refractive index, as a function of wavenumber, was taken from the Schott, Inc. website, and interpolated with a cubic spline. The air refractive index was simulated as constant 1.000. The silver dielectric function was initially taken to be that of the bulk material, but the modeling results were poor, so the spectra were re-modeled using a Drude dielectric function:

$$\varepsilon_{Ag} = \varepsilon_{\infty} + \frac{\omega_p^2}{i\omega\Gamma - \omega^2} \quad (2.1)$$

This dielectric function (Eq. 2.1) has three adjustable constants:  $\varepsilon_{\infty}$ ,  $\omega_p$ , and  $\Gamma$ , which were treated as unknowns in the modeling program. Finally, the AZO dielectric function was treated as an unknown adjustable constant ( $\varepsilon_{AZO}$ ), without an imaginary component. Using the Drude model for AZO did not improve the modeling results. The relevant constants ( $\varepsilon_{\infty}$ ,  $\omega_p$ ,  $\Gamma$ , and  $\varepsilon_{AZO}$ ) were adjusted according to a simplex algorithm that sought to minimize the variance between the experimental and theoretical spectra (Figs. 2.1 and 2.2). The experimental spectra were baseline corrected before this process took place.

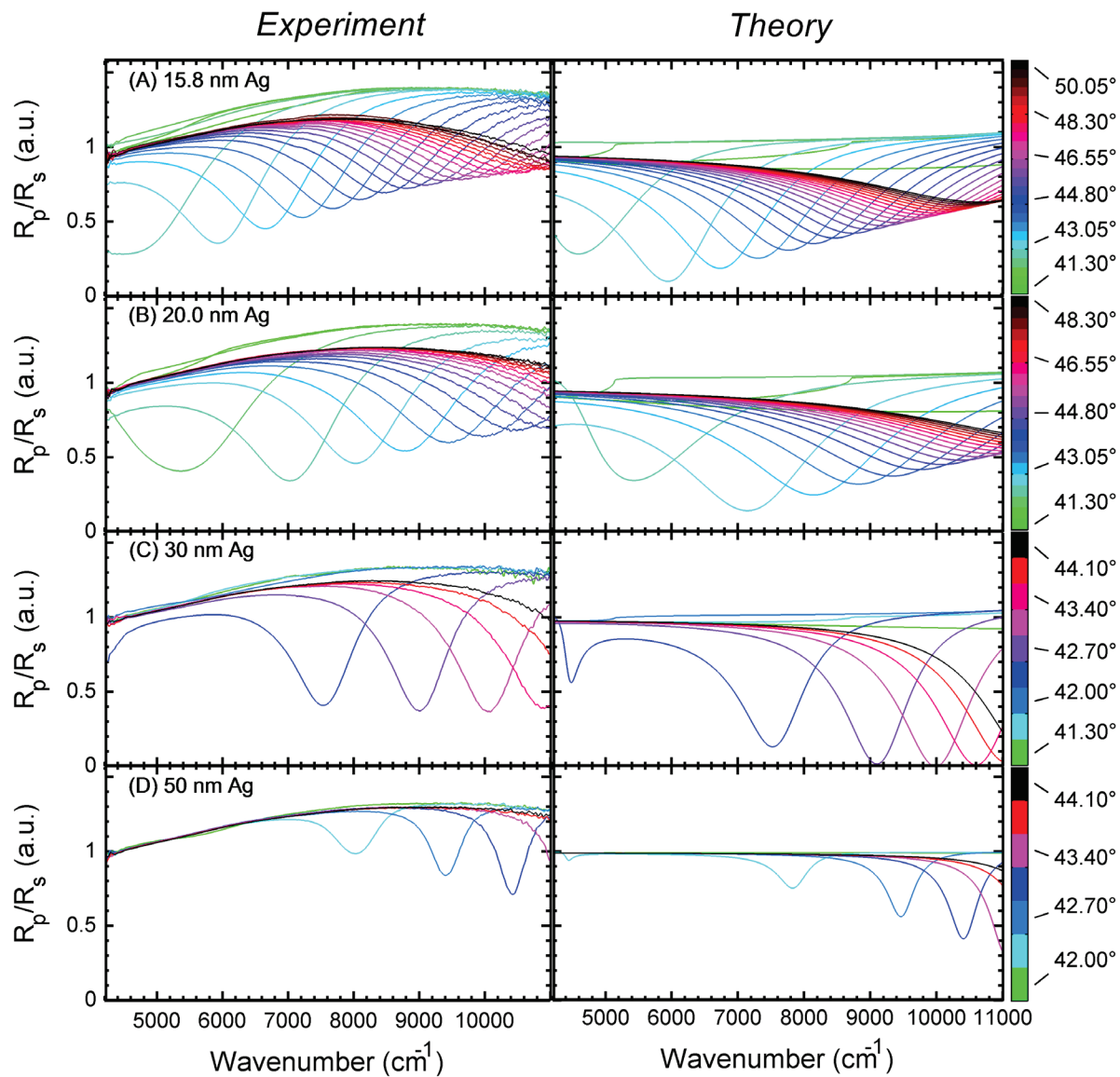


Figure 2.2: Experimental (left) and theoretical (right) FTIR-SPR spectra from 4200  $\text{cm}^{-1}$  to 11000  $\text{cm}^{-1}$  (2.38  $\mu\text{m}$  to 0.909  $\mu\text{m}$ ) for (A) the 21.5 nm AZO / 15.8 nm Ag / 48.5 nm AZO film, (B) the 27.5 nm AZO / 20.0 nm Ag / 27.1 nm AZO film, (C) the 23 nm AZO / 30 nm Ag / 23 nm AZO film, and (D) the 23 nm AZO / 50 nm Ag / 23 nm AZO film. The summary for all films is shown in Table 2.1.

### 2.3.2 Bulk silver

For comparison, the values of  $\varepsilon_\infty$ ,  $\omega_p$ , and  $\Gamma$  were obtained from a Drude model fit to the bulk silver dielectric function (Fig. 2.3). Several data sources were used: ATI: Acree Tech Inc. spectroscopic ellipsometry data; Sopra: Sopra S. A. database; Ordal: Ordal, *et al.* [58]; J&C: Johnson and Christy [59]. These dielectric functions and their fit are displayed in Fig. 2.3, and the results are also listed in Table 2.1. For the fitting procedure, the Drude dielectric function (Eq. 2.1) was split into its real and imaginary components, such that  $\varepsilon = \varepsilon_1 + i\varepsilon_2$ :

$$\varepsilon_1 = \varepsilon_\infty - \frac{\omega_p^2}{\Gamma^2 + \omega^2} \quad (2.2)$$

$$\varepsilon_2 = \frac{\omega_p^2 \Gamma}{\Gamma^2 \omega + \omega^3} \quad (2.3)$$

The fitting procedure for the bulk silver dielectric function used the same simplex algorithm as for the SPR spectra, and sought to fit both the real (Eq. 2.2) and imaginary (Eq. 2.3) components simultaneously. To achieve this, the following value ( $Q$ , Eq. 2.4) was minimized, based on the coefficient of determination ( $R^2$ , Eq. 2.5) of the two fits:

$$Q = 2 - (R_{\varepsilon_1}^2 + R_{\varepsilon_2}^2) \quad (2.4)$$

$$R^2 = 1 - \frac{\sum_i (y_i - \hat{y}_i)^2}{\sum_i (y_i - \bar{y})^2} \quad (2.5)$$

In Eq. 2.5,  $y_i$  are the experimental data points,  $\hat{y}_i$  are the modeled data points, and  $\bar{y}$  is the average of all  $y_i$ . Note that this definition of  $R^2$  is technically only valid for linear regression, and we have used it here only to produce an acceptable fit to the data. To avoid bias toward the data sets with higher populations, the fitting was done independently for each data source, and the results were averaged.

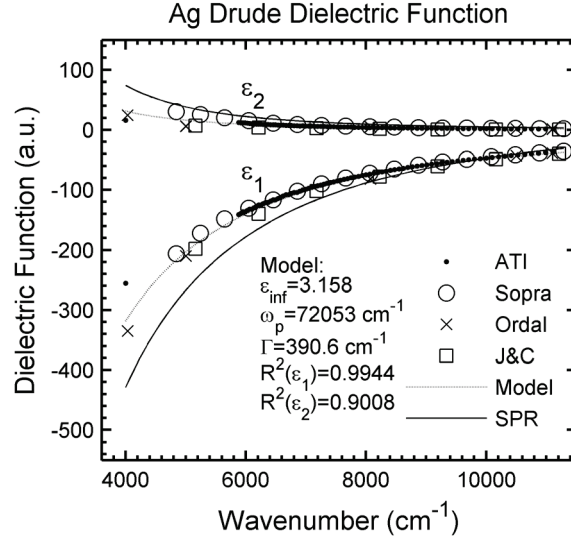


Figure 2.3: Complex dielectric function ( $\epsilon = \epsilon_1 + i\epsilon_2$ ) for bulk silver from 4000 to 11290  $\text{cm}^{-1}$  wavenumber (2.5  $\mu\text{m}$  to 0.886  $\mu\text{m}$  wavelength), from the following data sources: ATI: Acree Tech Inc.; Sopra: Sopra S. A. Database; Ordal: Ordal, et al.[58]; J&C: Johnson and Christy[59]. Model: Drude model fit, using the means across data sources of the parameters  $\epsilon_\infty$ ,  $\omega_p$ , and  $\Gamma$  given by the method in the text. The reported  $R^2$  values are the averages. SPR: Average result from SPR modeling (*cf.* Table 2.1).

### 2.3.3 Sensitivities

The sensitivities of these films to refractive index changes were estimated by theoretical modeling, in a similar fashion as Homola *et al.*[50]. Due to the low refractive index of the BK7 glass used ( $n_D=1.518$ ), and the limited angle range accessible by our instrument, it is not possible to study the sensitivity directly on these films. Using the material constants obtained by fitting (Table 2.1), three of the sandwich films, corresponding to 10nm, 20nm, and 50nm Ag, were modeled on Schott SF10 glass ( $n_D=1.728$ ) in water. A 20nm silver film was also modeled without AZO layers. The dispersion of the water was taken into account by interpolating the complex dielectric function [60]. Modes analyzed included both angle

interrogation (with wavenumber fixed at  $7600\text{ cm}^{-1}$ ), and wavenumber and wavelength interrogation (with angle fixed at  $52.4^\circ$ ). The results are shown in Table 2.2.

**Table 2.2: Estimated sensitivities of the films to refractive index changes. Sensitivities expressed in units per refractive index unit (RIU):  $S_\theta$ : angle interrogation,  $S_\nu$ : wavenumber interrogation,  $S_\lambda$ : wavelength interrogation.**

<b>Film</b>	<b><math>S_\theta</math> (degrees/RIU)</b>	<b><math>S_\nu</math> (<math>\text{cm}^{-1}</math>/RIU)</b>	<b><math>S_\lambda</math> (<math>\mu\text{m}</math>/RIU)</b>
10 nm Ag Sandwich	57.6553	-46325.3	12.040
20 nm Ag Sandwich	54.2281	-77312.8	13.359
50 nm Ag Sandwich	54.6001	-115443.8	14.276
20 nm Plain Ag	58.0800	-118088.9	20.552

## 2.4 Transmission

Optical transmission spectra of the films were collected between wavelengths of 190 nm and 1100 nm, by placing the films in a homemade sample holder placed in the beam of the spectrometer. The glass was not transparent below approximately 260 nm. The results are shown in Fig. 2.4.

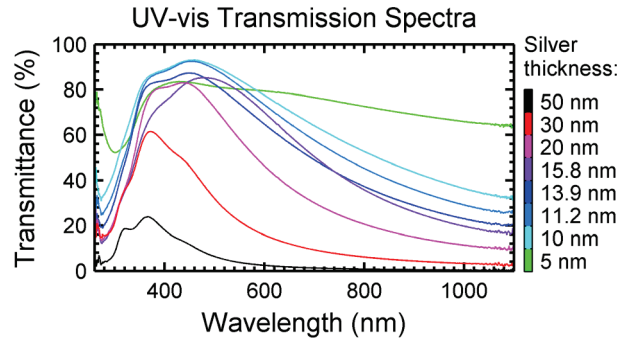


Figure 2.4: UV-vis transmission spectra of the AZO/Ag/AZO films.

## 2.5 Results

The results from the FTIR-SPR measurements are shown alongside the results from the modeling in Figs. 2.1 and 2.2. In all but the 5 nm film, the spectral minima have strong angle dependence, which is characteristic of a typical SPR response in the film system. It is easy to show that this SPR response is due to the silver layer by modeling using a three-layer system omitting the AZO layers (Glass / Ag / Air), and using the bulk dielectric function for Ag. Such models do show some spectral features, and appear somewhat similar to the theoretical results for the five-layer model shown in Figs. 2.1 and 2.2, although the precise locations and intensities of the resonances do not match. In contrast, similar features are not seen for AZO alone, by any reasonable estimation of its properties. The five-layer theoretical model appears to accurately predict most of the spectral features for the films with Ag thickness greater than 5 nm. However, the experimental spectra have a curved background, with higher  $R_p/R_s$  at larger wavenumbers, that is not predicted by the model. This effect is possibly due to scattering losses in  $R_s$  from film roughness. The model assumes the films are perfectly smooth, and does not estimate scattering. In addition, plain BK7 glass in the absence of any film does not show this effect, indicating that the effect is not an instrumental artifact. To correct for this, the curved background was subtracted from the experimental results before calculating the goodness of fit.

The effects of changing the thickness of the Ag layer are readily apparent. For the 5 nm Ag film (Fig. 2.1(A)), no SPR features are present at any angle accessible by the instrument, and the spectra display a larger intensity variation than is observed for the other films. These effects are similar to what is observed in the SPR spectra of layer-by-layer deposited films of silver and gold nanoparticles on glass, when the density of the nanoparticles is not high, and is possibly indicative that the film is not electrically contiguous. As the Ag films are made thicker (Figs. 2.1 and 2.2), the SPR responses gain intensity, the peak widths narrow, and the sensitivity to angle of incidence increases. These effects are consistent with theory. Finally, when the Ag film is thicker than 30 nm (Fig. 2.2(C) and 2.2(D)), the SPR responses lose intensity due to damping. By 70 nm Ag, no spectral features are evident (not shown).

The modeling results indicate that the values of  $\epsilon_\infty$ ,  $\omega_p$ , and  $\Gamma$  are significantly higher than for bulk silver for all films (Table 2.1 and Fig. 2.3). The experimental-theoretical match is good. In contrast, modeling using the bulk dielectric function of Ag produces poor results. In addition, the dispersion of the glass has also been accounted for, and the dielectric function of the AZO has been allowed to vary from film to film. Therefore, we believe that these values are the result of a real effect in the film, and are not simply due to a neglected aspect of the modeling.

The estimations of sensitivity to changes in refractive index are shown in Table 2.2. Although the silver layer thickness plays a role in the sensitivity by wavenumber and wavelength interrogation, it is clear from the results that the plain silver film has the highest sensitivity for all interrogation modes. Although only three sandwich films were modeled, the sensitivities of the other sandwich films are expected to be comparable. Note that due to the water dispersion, the wavenumber and wavelength interrogation mode sensitivities are nonlinear with refractive index.

The transmission spectra are presented in Fig. 2.4. As the silver layer thickness increases, the films become less transparent. For all but the 5 nm Ag film, the films show a maximum transmittance intensity between 360 and 500 nm, which blue-shifts as the thickness of the film increases. Also in these films, the transmittance decreases uniformly at wavelengths higher than 500 nm, due to increased reflection. In contrast, the 5 nm film transmittance

remains between 60 and 80% for all wavelengths higher than 500 nm, which is most likely an indication that the film is discontinuous and does not support planar SPR. For all films, the minima seen at approximately 265 nm (270 nm for 5 nm Ag) are most likely attributable to silver inter-band transitions.

## 2.6 Discussion

It is clear from the results that the optical properties of the silver are substantially different than bulk silver when in the sandwich configuration. While the higher damping constant is expected, the higher plasma frequency and high-frequency dielectric constant seem to contradict initial expectations; we would expect these values to be slightly lower, rather than higher, due to the inevitable imperfections of the deposition process. As explained below, one possible cause of the higher plasma frequency is the Schottky effect. If this is true, it could be a facile way to systematically engineer the plasma frequency in other SPR devices.

First, the plasma frequencies of the films were observed to be higher than that of bulk silver. One possible explanation is that there is charge transfer from the surrounding AZO to the Ag layer (a band-bending or Schottky effect). This effect is related to the difference in work functions of the two materials, and would likely be small because the work functions of Ag and AZO are similar (4.14-4.46 eV for Ag, depending on crystal orientation, and 3.7-4.62 eV for AZO, depending on doping) [61-63]. Unfortunately, there is not enough information to discern the magnitude of the charge transfer; even if work functions are chosen arbitrarily, the width of the transition region and the charge carrier density in the AZO must be known to discern the amount of additional electron density in the silver layer [64]. Additional experiments will need to be conducted to determine these parameters.

Second, the damping constant ( $\Gamma$ ) was also observed to be higher than that of bulk silver. This can be explained in terms of lower electron mobility ( $\mu$ ), to which  $\Gamma$  shares an inverse relationship:

$$\Gamma = \frac{e}{m\mu} \quad (2.6)$$

Here,  $m$  is the charge carrier effective mass,  $e$  is the elementary charge constant, and  $\mu$  is the mobility. Note that the mobility is frequency dependent in visible frequencies. In turn, the low mobility can be explained by the silver having a finite grain size, which introduces grain boundaries that reduce the electron mean free path. This explanation is in itself not particularly remarkable, as grain boundaries are expected in a sputtered polycrystalline film. However, note that  $\Gamma$  increases dramatically for the 5 nm silver film, which could be indicative of islanding or a similar kind of discontinuity. In addition,  $\Gamma$  should theoretically decrease with the thickness of the Ag layer [65], which is not seen in our results. This inconsistency is yet to be explained. The damping constant may also be artificially higher due to beam divergence in the instrument, causing a slight spread in the incident angles. This effect has not been accounted for in the modeling. The fact that  $\Gamma$  remains relatively constant for films as thin as 10 nm supports that the films are continuous down to 10 nm, which is a direct consequence of the sandwich stack.

Third, the high-frequency dielectric constant ( $\epsilon_\infty$ ) was also observed to be higher than that of bulk silver. The cause of this is currently unknown. Its effect on the Drude dielectric function is simple: it is an additive scaling term for the real part ( $\epsilon_1$ ). Essentially, the higher plasma frequency causes  $\epsilon_1$  to diverge significantly from the bulk value at lower frequencies, while the higher  $\epsilon_\infty$  brings  $\epsilon_1$  closer to the bulk value at higher frequencies (Fig. 2.3). This could potentially indicate that the effect causing the higher plasma frequency is frequency-dependent.

In the modeling, the AZO dielectric function was modeled as constant, with no dispersion. Substituting a dispersive dielectric function (the Drude model, Eq. 2.1) did not improve the modeling results. However, if the AZO is made more conductive in the future, it may be necessary to use a conductive dielectric function model.

The lower sensitivity of the sandwich films compared to plain silver (Table 2.2) can be understood as a consequence of the top AZO layer, which acts as a barrier, preventing the analyte from reaching the most sensitive region closest to the metal. This same barrier is anticipated to provide better chemical and mechanical stability to the films, though proving this will require additional experiments.

The observations of onset of a SPR response as a function of film thickness is predicted theoretically, but there have been limited means to study this effect experimentally. We recently demonstrated a similar effect for ITO thin films.[3] In the case of ITO the skin depth, which lies between 100 and 150 nm at wavenumbers less than  $7,000\text{ cm}^{-1}$ , is much greater than Ag, which has a skin depth of 23 nm between  $6,000$  and  $12,000\text{ cm}^{-1}$ . The skin depth correlates roughly to the thickness, which gives the onset of the SPR. The SPR as a function of thickness is observed at ca. 120 nm for ITO [3]. Here, we can predict that the onset of SPR will be less than 10 nm for Ag. In both conducting materials a similar decrease in the SPR effect is also observed as the film thickness increased above twice the skin depth of the film. The maximum effect is observed when the film thickness is approximately 25% greater than the skin depth. One of the significant differences between Ag and ITO is observed in the very thin films. In ITO we have observed the equivalent of the localized surface Plasmon resonance (LSPR), which we have called the capacitive Plasmon resonance to indicate that charge separation is normal to the film. This is observed at ca.  $8900\text{ cm}^{-1}$  in highly conductive ITO. Since the SPP of Ag is much higher and is outside of the spectral window of observation, no such effect is observed in ultrathin Ag films, in which the film thickness is significantly less than the skin depth.

In conclusion, using non-conductive AZO layers to prevent islanding of an SPR-active silver layer in a sandwich configuration seems to be a viable method of fabricating a robust and transparent SPR device, but there are still experiments that need to be performed. First, the sandwich configuration could potentially offer a previously unrealized method of controlling the observed plasma frequency and high-frequency dielectric constant, and thus the SPR responses, of the silver layers. Characterizing the dependence of these properties as a function of AZO thicknesses, doping levels, and deposition parameters is a high priority. Second, we are interested in functionalization of the AZO in order to construct a device. In principle, functionalization could be easily performed with thiols, which are known to form high-quality self-assembled monolayers on AZO.[66] Third, in order to use a device in an aqueous environment with the current angle range of our instrument, it is necessary to deposit the film system on a material with a higher index of refraction. Lastly, it remains to

be determined whether the films are resistant to tarnishing, oxidation, corrosion, and scratching. Initial results are promising, but will require a long-term study compared to a control.

## **2.7 Conclusions**

The films produced here are continuous down to 10 nm thickness of Ag. In contrast, films of silver on plain glass show islanding up to approximately 20-25 nm thickness. The surrounding AZO layers are able to inhibit islanding.

The modeling process, using a five-layer transfer-matrix method in conjunction with a simplex algorithm, was able to extract the dielectric function of the silver layers. This process could be applied to other SPR-active materials, which would allow us to more accurately estimate the effects of thin-film deposition.

In the ultra-thin Ag films studied using FT-SPR, the plasma frequency of the silver layer was demonstrably higher than its bulk value. If this can be shown to be due to the Schottky effect, it opens a technological door: film systems could be deliberately engineered to utilize this effect for SPR work.

## **2.8 Acknowledgments**

This work was supported in part by the National Science Foundation grant number 554076. The authors would like to acknowledge Stephen Weibel, Marta Cerruti, and Misun Kang for their helpful contributions.

## 2.9 References

1. C. Rhodes, S. Franzen, J. P. Maria, M. Losego, D. N. Leonard, B. Laughlin, G. Duscher, and S. Weibel, "Surface plasmon resonance in conducting metal oxides," *J Appl Phys* **100**, 054905 (2006).
2. S. Franzen, "Surface plasmon polaritons and screened plasma absorption in indium tin oxide compared to silver and gold," *J. Phys. Chem. C* **112**, 6027-6032 (2008).
3. C. Rhodes, M. Cerruti, A. Efremenko, M. Losego, D. E. Aspnes, J. P. Maria, and S. Franzen, "Dependence of plasmon polaritons on the thickness of indium tin oxide thin films," *J. Appl. Phys.* **103**, 093108 (2008).
4. S. Franzen, C. Rhodes, M. Cerruti, R. W. Gerber, M. Losego, J. P. Maria, and D. E. Aspnes, "Plasmonic phenomena in indium tin oxide and ITO-Au hybrid films," *Opt. Lett.* **34**, 2867-2869 (2009).
5. M. D. Losego, A. Y. Efremenko, C. L. Rhodes, M. G. Cerruti, S. Franzen, and J. P. Maria, "Conductive oxide thin films: Model systems for understanding and controlling surface plasmon resonance," *J. Appl. Phys.* **106**, 024903 (2009).
6. M. A. Noginov, L. Gju, J. Livenere, G. Zhu, A. K. Pradhan, R. Mundle, M. Bahoura, Y. A. Barnakov, and V. A. Podolskiy, "Transparent conductive oxides: Plasmonic materials for telecom wavelengths," *Appl. Phys. Lett.* **99**, 021101 (2011).
7. N. C. Chen, W. C. Lien, C. R. Liu, Y. L. Huang, Y. R. Lin, C. Chou, S. Y. Chang, and C. W. Ho, "Excitation of surface plasma wave at TiN/air interface in the Kretschmann geometry," *J. Appl. Phys.* **109**, 043104 (2011).
8. J. W. Cleary, G. Medhi, M. Shahzad, I. Rezadad, D. Maukonen, R. E. Peale, G. D. Boreman, S. Wentzell, and W. R. Buchwald, "Infrared surface polaritons on antimony," *Optics Express* **20**, 2693-2705 (2012).

9. P. R. West, S. Ichii, G. V. Naik, N. K. Emani, V. M. Shalaev, and A. Boltasseva, "Searching for better plasmonic materials," *Laser Photonics Rev.* **4**, 795-808 (2010).
10. R. Soref, R. E. Peale, and W. Buchwald, "Longwave plasmonics on doped silicon and silicides," *Optics Express* **16**, 6507-6514 (2008)
11. K. Fukuda, S. H. N. Lim, and A. Anders, "Coalescence of magnetron-sputtered silver islands affected by transition metal seeding (Ni, Cr, Nb, Zr, Mo, W, Ta) and other parameters," *Thin Solid Films* **516**, 4546-4552 (2008).
12. G. T. West, P. J. Kelly, and J. W. Bradley, "A comparison of thin silver films grown onto zinc oxide via conventional magnetron sputtering and HiPIMS deposition," *IEEE T. Plasma Sci.* **38**, 3057-3061 (2010).
13. M. Bao, G. Li, D. M. Jiang, W. J. Cheng, and X. M. Ma, "ZnO sensing film thickness effects on the sensitivity of surface plasmon resonance sensors with angular interrogation," *Mater. Sci. Eng. B-Adv.* **171**, 155-158 (2010).
14. L. Touahir, J. Niedziolka-Jonsson, E. Galopin, R. Boukherroub, A. C. Gouget-Laemmel, I. Solomon, M. Petukhov, J. N. Chazalviel, F. Ozanam, and S. Szunerits, "Surface plasmon resonance on gold and silver films coated with thin layers of amorphous silicon-carbon alloys," *Langmuir* **26**, 6058-6065 (2010).
15. S. Szunerits, X. Castel, and R. Boukherroub, "Surface plasmon resonance investigation of silver and gold films coated with thin indium tin oxide layers: Influence on stability and sensitivity," *J. Phys. Chem. C* **112**, 15813-15817 (2008).
16. M. R. Lockett, M. F. Phillips, M. R. Shortreed, S. C. Weibel, and L. M. Smith, "Surface plasmon resonance compatible carbon thin films," *Abstr. Pap. Am. Chem. Soc.* **233** (2007).

17. M. R. Lockett, S. C. Weibel, M. F. Phillips, M. R. Shortreed, B. Sun, R. M. Corn, R. J. Hamers, F. Cerrina, and L. M. Smith, "Carbon-on-metal films for surface plasmon resonance detection of DNA arrays," *J. Am. Chem. Soc.* **130**, 8611-8613 (2008).
18. M. Manesse, R. Sanjines, V. Stambouli, R. Boukherroub, and S. Szunerits, "Preparation and characterization of antimony-doped SnO<sub>2</sub> thin films on gold and silver substrates for electrochemical and surface plasmon resonance studies," *Electrochem. Commun.* **10**, 1041-1043 (2008).
19. M. Manesse, R. Sanjines, V. Stambouli, C. Jorel, B. Pelissier, M. Pisarek, R. Boukherroub, and S. Szunerits, "Preparation and characterization of silver substrates coated with antimony-doped SnO<sub>2</sub> thin films for surface plasmon resonance studies," *Langmuir* **25**, 8036-8041 (2009).
20. K. S. Phillips, J. H. Han, M. Martinez, Z. Z. Wang, D. Carter, and Q. Cheng, "Nanoscale glassification of gold substrates for surface plasmon resonance analysis of protein toxins with supported lipid membranes," *Anal. Chem.* **78**, 596-603 (2006).
21. S. Szunerits, and R. Boukherroub, "Preparation and characterization of thin films of SiO<sub>x</sub> on gold substrates for surface plasmon resonance studies," *Langmuir* **22**, 1660-1663 (2006).
22. S. Szunerits, Y. Coffinier, S. Janel, and R. Boukherroub, "Stability of the gold/silica thin film interface: Electrochemical and surface plasmon resonance studies," *Langmuir* **22**, 10716-10722 (2006).
23. L. Holland, and G. Siddall, "Heat-reflecting windows using gold and bismuth oxide films," *Brit. J. Appl. Phys.* **9**, 359-361 (1958).
24. J. C. C. Fan, F. J. Bachner, G. H. Foley, and P. M. Zavracky, "Transparent heat-mirror films of TiO<sub>2</sub>/Ag/TiO<sub>2</sub> for solar-energy collection and radiation insulation," *Appl. Phys. Lett.* **25**, 693-695 (1974).

25. H. Kostlin, and G. Frank, "Optimization of transparent heat mirrors based on a thin silver film between antireflection films," *Thin Sol. Films* **89**, 287-293 (1982).
26. B. E. Yoldas, and T. Okeefe, "Deposition of optically transparent IR reflective coatings on glass," *Appl. Opt.* **23**, 3638-3643 (1984).
27. C. A. Bishop, and R. P. Howson, "The performance of large area optical filters using DC magnetron sputtered metal thin-films in oxide metal-oxide sandwiches," *Sol. Energ. Mater.* **13**, 175-184 (1986).
28. E. Kusano, J. Kawaguchi, and K. Enjouji, "Thermal-stability of heat-reflective films consisting of oxide-Ag-oxide deposited by DC magnetron sputtering," *J. Vac. Sci. Technol. A* **4**, 2907-2910 (1986).
29. G. Leftheriotis, P. Yianoulis, and D. Patrikios, "Deposition and optical properties of optimised ZnS/Ag/ZnS thin films for energy saving applications," *Thin Sol. Films* **306**, 92-99 (1997).
30. N. B. Abaffy, J. G. Partridge, J. du Plessis, and D. G. McCulloch, "Optically absorbing trilayer films fabricated using a filtered cathodic vacuum arc," *Phys. Status Solidi. A* **205**, 1439-1442 (2008).
31. P. H. Berning and A. F. Turner, "Induced transmission in absorbing films applied to band pass filter design," *J. Opt. Soc. Am.* **47**, 230-239 (1957).
32. M. Bender, W. Seelig, C. Daube, H. Frankenberger, B. Ocker, and J. Stollenwerk, "Dependence of film composition and thicknesses on optical and electrical properties of ITO-metal-ITO multilayers," *Thin Sol. Films* **326**, 67-71 (1998).
33. Kloppel, W. Kriegseis, B. K. Meyer, A. Scharmann, C. Daube, J. Stollenwerk, and J. Trube, "Dependence of the electrical and optical behaviour of ITO-silver-ITO multilayers on the silver properties," *Thin Sol. Films* **365**, 139-146 (2000).

34. M. Sawada, M. Higuchi, S. Kondo, and H. Saka, "Characteristics of indium-tin-oxide/silver/indium-tin-oxide sandwich films and their application to simple-matrix liquid-crystal displays," *Jpn. J. Appl. Phys.* 1 **40**, 3332-3336 (2001).
35. M. Fahland, P. Karlsson, and C. Charton, "Low resistivity transparent electrodes for displays on polymer substrates," *Thin Sol. Films* **392**, 334-337 (2001).
36. Y. S. Jung, Y. W. Choi, H. C. Lee, and D. W. Lee, "Effects of thermal treatment on the electrical and optical properties of silver-based indium tin oxide/metal/indium tin oxide structures," *Thin Sol. Films* **440**, 278-284 (2003).
37. X. J. Liu, X. Cai, J. S. Qiao, H. F. Mao, and N. Jiang, "The design of ZnS/Ag/ZnS transparent conductive multilayer films," *Thin Sol. Films* **441**, 200-206 (2003).
38. D. R. Sahu, S. Y. Lin, and J. L. Huang, "ZnO/Ag/ZnO multilayer films for the application of a very low resistance transparent electrode," *Appl. Surf. Sci.* **252**, 7509-7514 (2006).
39. D. R. Sahu, and J. L. Huang, "Characteristics of ZnO-Cu-ZnO multilayer films on copper layer properties," *Appl. Surf. Sci.* **253**, 827-832 (2006).
40. D. R. Sahu, and J. L. Huang, "High quality transparent conductive ZnO/Ag/ZnO multilayer films deposited at room temperature," *Thin Sol. Films* **515**, 876-879 (2006).
41. C. Guillen, and J. Herrero, "Transparent conductive ITO/Ag/ITO multilayer electrodes deposited by sputtering at room temperature," *Opt. Comm.* **282**, 574-578 (2009).
42. S. I. Bozhevolnyi, *Plasmonic nanoguides and circuits* (Pan Stanford, 2009)
43. R. Zia, M. D. Selker, P. B. Catrysse, and M. L. Brongersma, "Geometries and materials for subwavelength surface plasmon modes," *J. Opt. Soc. Am. A* **21**, 2442-2446 (2004)

44. R. Lazzari, and J. Jupille, "Silver layers on oxide surfaces: morphology and optical properties," *Surf. Sci.* **482**, 823-828 (2001).
45. M. Stoneham, "Systematics of metal-insulator interfacial energies - a new rule for wetting and strong catalyst support interactions," *Appl. Surf. Sci.* **14**, 249-259 (1983).
46. F. Didier, and J. Jupille, "Simple views on metal/oxide interfaces: Contributions of the long-range interactions to the adhesion energy," *J. Adhesion* **58**, 253-261 (1996).
47. V. Singh, R. M. Mehra, A. Yoshida, and A. Wakahara, "Doping mechanism in aluminum doped zinc oxide films," *J. Appl. Phys.* **95**, 3640-3643 (2004).
48. M. G. Nicholas, T. M. Valentine, and M. J. Waite, "The wetting of alumina by copper alloyed with titanium and other elements," *J. Mat. Sci.* **15**, 2197-2206 (1980).
49. Anders, E. Byon, D.-H. Kim, K. Fukuda, and S. H. N. Lim, "Smoothing of ultrathin silver films by transition metal seeding," *Sol. State Comm.* **140**, 225-229 (2006).
50. J. Homola, S. S. Yee, and G. Gauglitz, "Surface plasmon resonance sensors: review," *Sensor. Actuat. B-Chem.* **54**, 3-15 (1999).
51. J. Homola, "Present and future of surface plasmon resonance biosensors," *Anal. Bioanal. Chem.* **377**, 528-539 (2003).
52. J. Ā. Homola and M. Piliarik, "Surface plasmon resonance (SPR) sensors" in *Surface Plasmon Resonance Based Sensors*, O. S. Wolfbeis, ed. (Springer Berlin Heidelberg, 2006), 45-67.
53. X. D. Hoa, A. G. Kirk, and M. Tabrizian, "Towards integrated and sensitive surface plasmon resonance biosensors: A review of recent progress," *Biosens. Bioelectron.* **23**, 151-160 (2007).

54. E. Kretschmann, and H. Raether, "Radiative decay of non radiative surface plasmons excited by light," *Z. Naturforsch. Pt. A* **23**, 2135-2136 (1968).
55. E. Kretschmann, "Decay of non radiative surface plasmons into light on rough silver films. Comparison of experimental and theoretical results," *Opt. Comm.* **6**, 185-187 (1972).
56. O. S. Heavens, *Optical Properties of Thin Solid Films* (Butterworths Scientific Publications, London, 1955).
57. H. A. Macleod, *Thin-Film Optical Filters* (CRC Press/Taylor & Francis, Boca Raton, FL, 2010), Chap. 2.
58. M. A. Ordal, L. L. Long, R. J. Bell, S. E. Bell, R. R. Bell, R. W. Alexander, and C. A. Ward, "Optical properties of the metals Al, Co, Cu, Au, Fe, Pb, Ni, Pd, Pt, Ag, Ti, and W in the infrared and far infrared," *Appl. Opt.* **22**, 1099-1119 (1983).
59. P. B. Johnson and R. W. Christy, "Optical constants of the noble metals," *Phys. Rev. B* **6**, 4370-4379 (1972).
60. D. J. Segelstein, "The complex refractive index of water," Thesis (M.S.), Dept. of Physics. University of Missouri, Kansas City (1981).
61. M. Chelvayohan, and C. H. B. Mee, "Work function measurements on (110), (100) and (111) surfaces of silver," *J. Phys. C Sol. State* **15**, 2305-2312 (1982).
62. X. Jiang, F. L. Wong, M. K. Fung, and S. T. Lee, "Aluminum-doped zinc oxide films as transparent conductive electrode for organic light-emitting devices," *Appl. Phys. Lett.* **83**, 1875-1877 (2003).
63. T. W. Kim, D. C. Choo, Y. S. No, W. K. Choi, and E. H. Choi, "High work function of Al-doped zinc-oxide thin films as transparent conductive anodes in organic light-emitting devices," *Appl. Surf. Sci.* **253**, 1917-1920 (2006).

64. B. G. Streetman, *Solid State Electronic Devices* (Prentice-Hall, Englewood Cliffs, N.J., 1980).
65. T. Sun, B. Yao, A. P. Warren, K. Barmak, M. F. Toney, R. E. Peale, and K. R. Coffey, “Dominant role of grain boundary scattering in the resistivity of nanometric Cu films,” *Phys. Rev. B* **79**, 041402(R) (2009).
66. C. L. Rhodes, S. Lappi, D. Fischer, S. Sambasivan, J. Genzer, and S. Franzen, “Characterization of monolayer formation on aluminum-doped zinc oxide thin films,” *Langmuir* **24**, 433-440 (2008).

### **3. Reassessment of data: Infrared surface plasmon resonance of AZO-Ag-AZO sandwich thin films**

#### **3.1 Introduction**

When fitting SPR spectra, one must exercise caution in the interpretation of the results. There are many variables that must be accounted for, some of which can have very large effects on the spectra: the incident angles, the refractive indices of the glass and ambient environment, the film thicknesses, and the film dielectric functions, which may contain additional variables depending on the model used. Many of these variables are co-variant, meaning that they have similar effects on the modeled results, and thus there can be multiple sets of values that produce similar spectra.

In the recently published article “Infrared surface plasmon resonance of AZO-Ag-AZO sandwich thin films,” [1] the modeling results suggested that the plasma frequency of the silver was significantly higher than the bulk value. Since plasma frequency is proportional to the square root of the charge carrier density, and the ZnO/Ag interface is known to form a Schottky barrier [2, 3], it was suggested that a charge transfer mechanism was responsible for the abnormally high plasma frequencies. When the work was performed, there were several modeling variables that were assumed to be known: The incident angles, which were taken from previous experiments, and the film thicknesses, which were reported to be known via an in-situ quartz crystal microbalance. In addition, the AZO dielectric function was taken to be constant. Since then, new information has been revealed, and it is necessary to assess whether or not our original conclusions are still valid.

#### **3.2 Experiment**

The film thicknesses were analyzed by X-ray reflectivity (XRR), producing some discrepancies between the previously reported AZO thicknesses and the ones obtained via XRR. For the XRR measurement, the films were scanned over  $\theta$ - $2\theta$ , producing a complex interference pattern in the reflected intensity. The results were then fitted to a multilayer

transfer-matrix model. Assuming known sample composition, X-ray wavelength, and incident angles, the film thicknesses were extracted. The results of this procedure are displayed in Table 3.1, along with the previously reported thicknesses. In all of the new fitting attempts in this report, the new thicknesses from XRR have been used. Note that the XRR data was collected approximately two years after the films were initially fabricated. While AZO and Ag are known to both be slightly unstable in air, the films were stored in a desiccator and do not appear to have significantly altered optical properties.

The fitting method was conducted in Matlab. To model the SPR spectra, the multilayer transfer-matrix method was used. For fitting the theoretical curves to the experimental data, a simplex algorithm was used to adjust the fitting parameters to attempt to minimize a combined sum of squares error (SSE), which was simply the sum of the SSE from each angle measured. The experimental data were background corrected before calculating the SSE. Because the fitting process is time-intensive, film G was chosen as a model film in order to compare the results of the different fitting parameters.

**Table 3.1: Film thicknesses for the AZO-Ag-AZO sandwich thin films, as originally reported, and as measured by XRR.**

<b>Film ID</b>	<b>Previous Thicknesses AZO/Ag/AZO (nm)</b>	<b>XRR Thicknesses AZO/Ag/AZO (nm)</b>
A	23 / 5 / 23	19.3 / 5.8 / 19.1
B	23 / 10 / 23	16.4 / 10.0 / 17.4
C	23 / 11.2 / 23	24.7 / 12.1 / 20.2
D	42 / 13.9 / 22.4	17.7 / 14.0 / 32.5
E	21.9 / 15.8 / 48.5	18.1 / 16.6 / 45.3
F	27.5 / 20 / 27.1	22.5 / 20.1 / 26.7
G	23 / 30 / 23	50.5 / 31.1 / 21.6
H	23 / 50 / 23	58.7 / 52.3 / 23.0

Several sets of fitting parameters were defined. In all cases, the film thicknesses were assumed to be those from the XRR experiment, and the dielectric function of air was assumed to be constant 1.000569. The BK-7 glass refractive index was assumed to be exactly as reported on the Esco, Inc. website [4], and was cubic spline interpolated. With these parameters set, there remain the AZO dielectric function, the silver dielectric function, and the angles of incidence to consider.

The AZO dielectric function was allowed to vary one of several ways: according to the Drude model, set as bulk ZnO, or taken as scalar value. In the Drude model, there are a minimum of three variables to account for:  $\epsilon_\infty$ ,  $\omega_p$ , and  $\Gamma$ . Note that in the limit of  $\omega_p$  approaching zero, the Drude model is equivalent to the scalar-valued dielectric function  $\epsilon_\infty$ , and thus fitting the scalar value is only useful for convenience, as it reduces the time required for optimization. Conduction electrons in AZO are generated primarily by two sources: oxygen vacancies, and aluminum substitutions. In these films, the AZO most likely has few oxygen vacancies, as it was deposited in oxygen in order to make the layers relatively non-

conductive. However, the aluminum is still present, and thus it is still reasonable to expect a small amount of conductivity for the AZO, especially at low frequencies. Therefore, as with most conductors, the AZO layers may be modeled using a Drude dielectric function.

The bulk ZnO dielectric function, which is the square of the refractive index, was measured in this frequency range by Bond et al. in 1965 [5]. Although ZnO is birefringent, our films are not expected to have a preferred orientation relative to the incident light, so an average was taken of the ordinary and extraordinary dielectric functions. The average bulk ZnO dielectric function is then linear, with an equation of  $\epsilon_1 = 1.93 \times 10^{-5} \omega (\text{/cm}^{-1}) + 3.62$ .

The silver layer dielectric function may also either be allowed to vary according to the Drude model or taken to be that of bulk silver. At these frequencies, bulk silver fits the Drude model very well, with constants  $\epsilon_\infty=2.65$ ,  $\omega_p=70619 \text{ cm}^{-1}$ , and  $\Gamma=399 \text{ cm}^{-1}$ . These values were previously obtained by a nonlinear regression fit of multiple sets of data, fitting both the real and imaginary components simultaneously, and then averaging across the data sets [1].

Finally, we consider the possibility that the angles reported in the article might be slightly inaccurate. The values were reported as the internal angles inside the BK-7 prism, and are the values that we have been reporting for several years. However, most of our previous work focused on conducting metal oxides like ITO, which are significantly less conductive than the silver sandwiches, and thus less sensitive to incident angle, requiring less precision. Moreover, angle calibration on an SPR device can be difficult, due to the custom nature of many of the instruments, and the high level of precision required. One option is to calibrate it with a standard, a sample of known composition and thickness, usually pure evaporated or sputtered gold on SF-10 or BK-7 glass. The results are then fit to the theoretical reflectance model, using the bulk values for the metal. This was attempted on our instruments with several samples: a standard 40 nm gold sample on SF-10, a 20 nm silver sample on BK-7, and a 50 nm silver sample on BK-7. However, the results were unpredictable and did not produce a good fit to any theoretical model for all three films. As a possible recourse, we may perform the angle calibration on our AZO/Ag/AZO sandwich films, and compare the consistency of the results for the entire film set.

### 3.3 Results

#### 3.3.1 Method 1: Drude AZO, bulk Ag

In the previously published fitting procedure, the possibility that AZO was slightly conductive was considered by modeling the AZO layers with a Drude dielectric function. This method did not produce substantially better fits to the experimental spectra versus using a constant dielectric function (the limit of  $\omega_p=0$ ), and thus was ruled out. We attempt it here again due to the adjusted thicknesses, using film G as a model case.

Using literature value of  $m^*=0.27m_e$  [3] and estimate of  $\mu=10 \text{ cm}^2\text{V}^{-1}\text{s}^{-1}$  (via Hall Effect on other AZO films), the damping ( $\Gamma=e/m^*\mu$ ) can be set to  $3457.7 \text{ cm}^{-1}$ . Then, the fitting process may be limited to only the AZO  $\epsilon_\infty$  and  $\omega_p$ . The values for  $\epsilon_\infty$  and  $\omega_p$  are expected to be highly covariant, as an increase in  $\epsilon_\infty$  causes  $\epsilon_1$  to increase, while an increase in  $\omega_p$  causes  $\epsilon_1$  to decrease.

As can be seen in Fig. 3.1, the fitting parameters are highly covariant, as expected. The minimum is located at ( $\epsilon_\infty=1.7859$ ,  $\omega_p=2774.6 \text{ cm}^{-1}$ ), with a sum squared error of 86.2. These values generate the SPR spectrum seen in Fig. 3.2, which is shown alongside the background-corrected experimental spectrum for comparison.

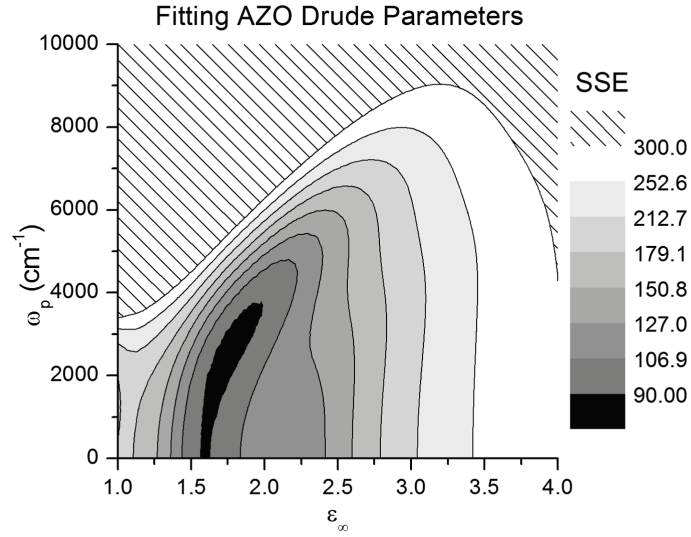


Figure 3.1: Contour map of sum squared error for film G, as a function of AZO Drude model parameters plasma frequency ( $\omega_p$ ) and high-frequency dielectric constant ( $\epsilon_\infty$ ), using constrained value for the damping ( $\Gamma=3457.7$  cm<sup>-1</sup>) and using the bulk silver dielectric function. The minimum of 86.2 is located at ( $\epsilon_\infty=1.7859$ ,  $\omega_p=2774.6$  cm<sup>-1</sup>).

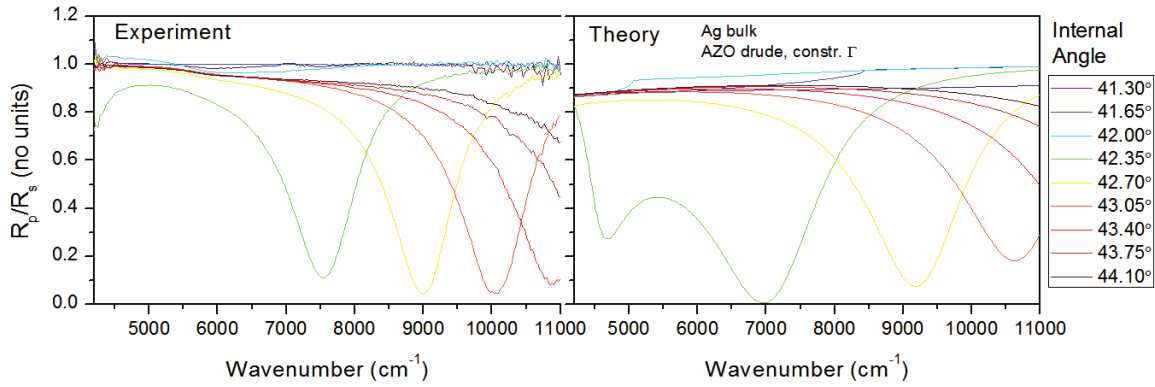


Figure 3.2: Left: The background-corrected experimental FT-SPR spectrum for film G. Right: Resulting theoretical FT-SPR spectrum at the SSE minimum of the AZO Drude model parameter space in Fig. 3.1 ( $\epsilon_{\infty}=1.7859$ ,  $\omega_p=2774.6 \text{ cm}^{-1}$   $\Gamma=3457.7 \text{ cm}^{-1}$ ), using the bulk silver dielectric function.

### 3.3.2 Method 2: Bulk ZnO, bulk Ag

The SPR spectra may also be modeled using the bulk dielectric function of ZnO. With the film thicknesses and angles set to their known values, and using the bulk silver dielectric function, there are then no adjustable parameters to fit, and only one SPR spectrum is possible, seen in Fig. 3.3, which is shown alongside the background-corrected experimental spectrum for comparison. The sum squared error by this method is 281.1.

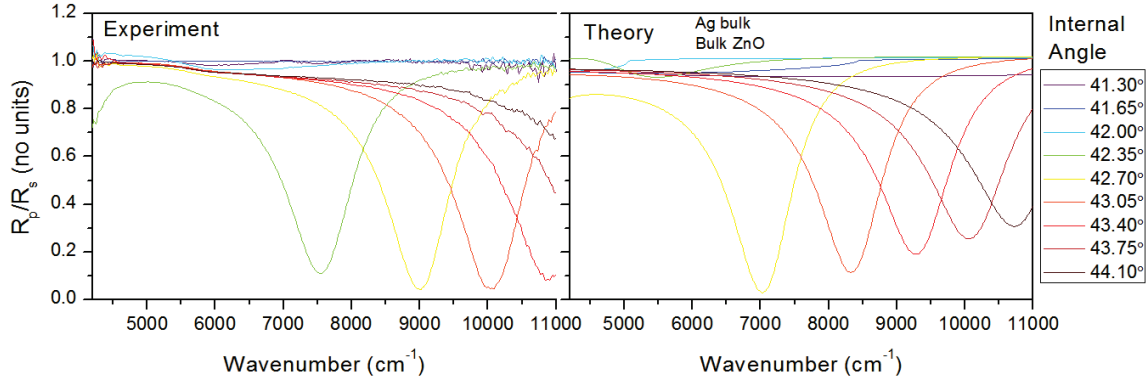


Figure 3.3: Left: The background-corrected experimental FT-SPR spectrum for film G. Right: Resulting theoretical FT-SPR spectrum using the bulk silver dielectric function and the bulk ZnO dielectric function. With the angles fixed at their previously reported values, there are no parameters to optimize, and only one SPR spectrum is possible. The sum squared error by this method is 281.1.

### 3.3.3 Method 3: Constant AZO, Drude Ag

The spectra were then refit in the same manner as the original publication. The silver dielectric function was allowed to vary according to the Drude model, while the AZO dielectric function was set as a constant. In this manner there are four fitting parameters that must be simultaneously optimized: for silver,  $\epsilon_\infty$ ,  $\omega_p$ , and  $\Gamma$ , and for AZO,  $\epsilon_{AZO}$ . The optimized values for film G are then ( $\epsilon_\infty=32.90$ ,  $\omega_p=9.386 \times 10^4 \text{ cm}^{-1}$ ,  $\Gamma=600 \text{ cm}^{-1}$ , and  $\epsilon_{AZO}=2.360$ ), with an SSE of 8.123. The SPR spectrum that results from these values is shown in Fig. 3.4 next to the background-corrected experimental spectrum.

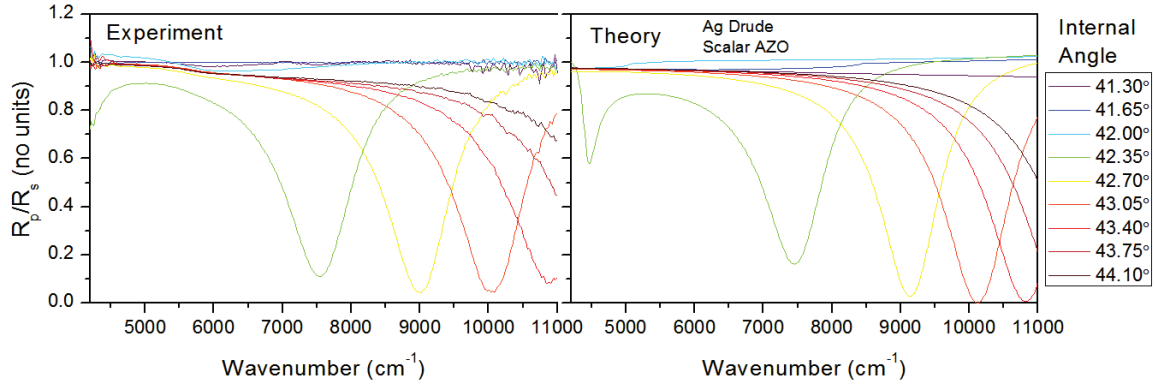


Figure 3.4: Left: The background-corrected experimental FT-SPR spectrum for film G. Right: Resulting theoretical FT-SPR spectrum, returning to the original fitting method. The silver Drude model parameters ( $\epsilon_\infty$ ,  $\omega_p$ , and  $\Gamma$ ) were allowed to vary freely, as was the AZO scalar dielectric function ( $\epsilon_{AZO}$ ). The SSE minimum in the four-dimensional parameter space is then 8.123, at ( $\epsilon_\infty=32.90$ ,  $\omega_p=9.386 \times 10^4 \text{ cm}^{-1}$ ,  $\Gamma=600 \text{ cm}^{-1}$ , and  $\epsilon_{AZO}=2.360$ ).

### 3.3.4 Method 4: Free angles

One possibility that has not yet been investigated is that the angles of incidence are incorrectly reported. Slight changes of angle are capable of producing extremely large changes in an SPR spectrum. Assuming that the relationship between the spectrometer's micrometer position and the external angle is linear (*i.e.* the spacing between the angles is constant), there are only two parameters that must be adjusted: the starting angle ( $\theta_{\text{start}}$ ), and the increment ( $\theta_{\text{incr}}$ ). The sum squared error (SSE) were plotted as a contour map vs. the fitting parameters in Fig. 3.5. There is one minimum, which is located at ( $\theta_{\text{start}} = 31.65^\circ$ ,  $\theta_{\text{incr}} = 0.67^\circ$ ), with an SSE of 5.09. The SPR spectrum produced at this minimum is shown in Fig. 3.6 next to the background-corrected experimental spectrum.

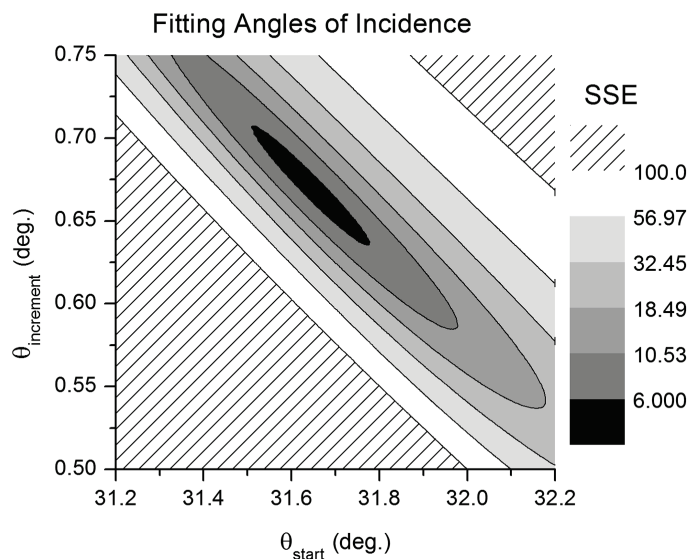


Figure 3.5: Contour map of the SSE for fitting film G in the angle space, with the starting angle on the x-axis and the angle increment on the y-axis. The minimum SSE of 5.09 is located at ( $\theta_{\text{start}} = 31.65^\circ$ ,  $\theta_{\text{incr}} = 0.67^\circ$ ), which produces the SPR spectrum seen on the right side of Fig. 3.6.

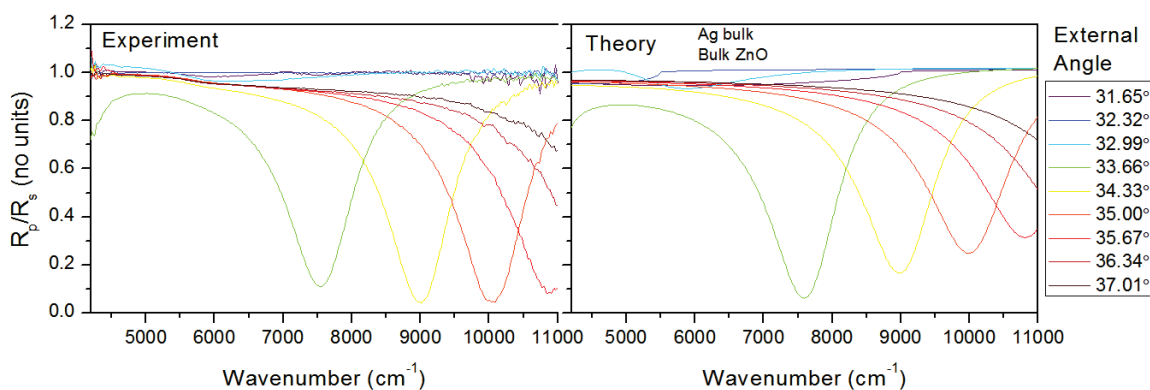


Figure 3.6: Left: The background-corrected experimental FT-SPR spectrum for film G. Right: Resulting theoretical FT-SPR spectrum, allowing angles of incidence to vary freely. The best fit is obtained by the parameters ( $\theta_{\text{start}} = 31.65^\circ$ ,  $\theta_{\text{incr}} = 0.67^\circ$ ), and produces an SSE of 5.09.

### 3.4 Discussion

We can quantitatively compare the different fitting methods using the sum squared errors (SSE), because all fits were performed on the same film G and the method of calculating the SSE was identical for all the fitting methods. The SSEs for the various fitting methods are shown in Table 3.2. We can identify two methods that produce a good fit to the experimental data: Method 3, which was permitting the Ag Drude parameters to vary, with AZO dielectric function as a varying scalar, and Method 4, which was allowing the angles to vary while keeping the materials parameters at their bulk values.

**Table 3.2: Comparison of fitting results, using the sum squared error, for each fitting method described.**

Method Name	Description	SSE	Results
Method 1	Drude AZO, Bulk Ag	86.2	Poor fit
Method 2	Bulk ZnO, Bulk Ag	281.1	Poor fit
Method 3	Constant AZO, Drude Ag	8.123	Good fit, similar results as original
Method 4	Free Angles, Bulk ZnO, Bulk Ag	5.09	Good fit, new angles similar to physically measured

Method 3 is identical to the method used in the original paper, and produces similar results. In the original paper, the values produced by this method are ( $\epsilon_{\infty}=39.57$ ,  $\omega_p=9.452 \times 10^4 \text{ cm}^{-1}$ ,  $\Gamma=626 \text{ cm}^{-1}$ , and  $\epsilon_{AZO}=1.957$ ), and the new values are ( $\epsilon_{\infty}=32.90$ ,  $\omega_p=9.386 \times 10^4 \text{ cm}^{-1}$ ,  $\Gamma=600 \text{ cm}^{-1}$ , and  $\epsilon_{AZO}=2.360$ ). In both cases, the silver,  $\epsilon_{\infty}$ ,  $\omega_p$ , and  $\Gamma$  are all significantly higher than the values of bulk silver, and  $\epsilon_{AZO}$  is lower than bulk ZnO. As before, this suggests that the materials have altered properties compared to the bulk, and that the silver is somehow gaining a significant amount of free electron density [1].

Method 4 also produced an acceptable fit to the data, by allowing the angles to vary while holding the materials parameters at their bulk values. From a modeling perspective, this method is unconventional, since the SPR response is so highly angle dependent that many SPR spectra may be incorrectly “fit” by freely adjusting the angles without constraints. Because of this limitation, it is important to ensure that the fitting results are within a few fractions of a degree of the expected values. Working backwards from the previously reported internal angles, we may extract the external angles using Snell’s law, the known prism geometry, and the known prism refractive index at  $6000\text{ cm}^{-1}$ , which is the approximate center point of the surface plasmon polariton responses at these angles in ITO, the material used to produce the original values. We may also compare these angles to ones physically measured on the instrument. The external angles by all three methods are reported in Table 3.3. The fitting results are within a few tenths of a degree of the physically measured angle, and can therefore be considered acceptable.

These two fitting methods therefore both produce acceptable results. Comparing the spectra of Fig. 3.4 to Fig. 3.6, it is clear that Method 3 produces a more accurate approximation of the resonance intensities, while Method 4 produces a more accurate approximation of the resonance frequencies.

The plausibilities of these results are more difficult to assess, however. The results of Method 3 indicate that the silver has dramatically altered optical properties compared to bulk silver, and more specifically that it has a higher plasma frequency, high-frequency dielectric constant, and damping constant than bulk silver. As in [1], this could potentially be attributed to a Schottky effect charge transfer from the AZO into the silver. It is known that AZO and silver form a Schottky barrier [2, 3], but it is notprecedented for this effect to have an effect on the optical properties of the layers. On the other hand, from Method 4, the calculated angles are not very different from either the physically measured angles or the angles back-calculated via Snell’s law, which is significantly more plausible.

**Table 3.3: Comparison of angles measured on the instrument, back-calculated using Snell's law, and the fitting results from the free angle calculation. The fitting results are close to both the physically measured angle and the Snell angle, and thus can be considered acceptable.**

<b>Stage Index</b>	<b>Measured Angle (deg.)</b>	<b>Snell Angle (deg.)</b>	<b>Fitting Results, Film G (deg.)</b>
2.00	33.22	31.27	31.65
2.25	33.83	31.84	32.32
2.50	34.45	32.40	32.99
2.75	35.06	32.96	33.66
3.00	35.67	33.52	34.33
3.25	36.29	34.08	35.00
3.50	36.90	34.64	35.67
3.75	37.51	35.20	36.34
4.00	38.13	35.75	37.01
4.25	38.74	36.30	37.68
4.50	39.35	36.85	38.35
4.75	39.97	37.40	39.02
5.00	40.58	37.95	39.69
5.25	41.19	38.50	40.36
5.50	41.81	39.05	41.03
5.75	42.42	39.59	41.70
6.00	43.03	40.14	42.37
6.25	43.65	40.68	43.04
6.50	44.26	41.22	43.71
6.75	44.87	41.76	44.38
7.00	45.49	42.30	45.05
7.25	46.10	42.84	45.72
7.50	46.71	43.38	46.39
7.75	47.33	43.91	47.06

**Table 3.3 Continued**

8.00	47.94	44.45	47.73
8.25	48.55	44.99	48.40
8.50	49.17	45.52	49.07
8.75	49.78	46.06	49.75
9.00	50.39	46.59	50.42
9.25	51.01	47.12	51.09
9.50	51.62	47.65	51.76

---

### **3.5 Conclusions**

With the new film thicknesses from XRR, the infrared FT-SPR spectrum of a model film, Film G, were re-fitted using a variety of techniques. The sum squared error between the experimental and theoretical spectra indicated that two of these techniques were superior: 1) Allowing the silver dielectric function to vary freely according to the Drude model, and 2) allowing the angles of incidence to vary freely while holding the dielectric functions at their bulk values. The first of these produced similar results to the initial results reported in [1], with the silver layer having higher plasma frequency, high-frequency dielectric function, and damping constant than bulk. The second of these produced angles that were comparable to both the physically measured angles and the previously reported angles.

Although both of these modeling techniques produced an acceptable fit, it is more plausible that the angles of the instrument are slightly miscalibrated than that the silver layer is gaining enough electron density to change its optical properties. This conclusion, if true, will invalidate the conclusion of the previous paper that the silver is gaining free electron density from a charge transfer effect. To test this, we can scan the films on other FT-SPR instruments, and we can scan additional angle calibration standards in the existing instrument.

### 3.6 Acknowledgments

I would like to thank Edward Sachet for performing the X-ray reflectivity measurement and analysis. This work was funded in part by the National Science Foundation grant number 554076.

### 3.7 References

1. J. Guske, J. Brown, A. Welsh, and S. Franzen, "Infrared surface plasmon resonance of AZO-Ag-AZO sandwich thin films," *Optics Express* **20**, 23215-23226 (2012).
2. L. J. Brillson, and Y. Lu, "ZnO Schottky barriers and Ohmic contacts," *Journal of Applied Physics* **109**, 121301 (2013).
3. H. Sheng, S. Muthukumar, N. W. Emanetoglu, and Y. Lu, "Schottky diode with Ag on (112-bar 0) epitaxial ZnO film," *Applied Physics Letters* **80**, 2132-2134 (2002).
4. Esco Optics Inc., "BK-7 Optical Glass," <http://www.escooptics.com/material-data/bk7-optical-glass>, Accessed April 4, 2013.
5. W. L. Bond, "Measurement of the Refractive Indices of Several Crystals," *Journal of Applied Physics* **36**, 1674-1677 (1965).

## 4. Trilayer AZO-Ag-AZO films for SPR deposited by PLD: Influence of AZO conductivity

**Abstract:** Trilayer films of aluminum-doped zinc oxide (AZO) / Ag / AZO were fabricated on calcium fluoride and BK-7 glass substrates using pulsed laser deposition (PLD). The films were analyzed via surface plasmon resonance (SPR) spectroscopy in two separate instruments with similar results. The AZO layers were fabricated with varying Al doping concentrations and in varying oxygen environments, which allowed control of the AZO plasma frequency. This allowed the AZO plasmonic quasi-bound mode (QBM) to be observed over a range of frequencies. The AZO plasma frequencies and damping frequencies were obtained from the theoretical spectra and were used to calculate the AZO resistivities, which were the same order of magnitude as the resistivities measured via four-point probe on pure AZO films. The highly angle-dependent silver surface plasmon polariton (SPP) mode was also observed, and was compared qualitatively to the theoretical models. For most films, the experimental-theoretical match was good, but could be significantly improved by minor adjustments to film thicknesses. Deposition rates from stylus profilometry had a high standard deviation, which gives validity to these adjustments. However, SPP results for two films were highly inconsistent with the theoretical models, even with extreme thickness adjustments. This indicated that additional confounding effects may be present, possibly from experimental variations in the film fabrication procedures.

### 4.1 Introduction

Silver and gold are well known as SPR-active materials and have been used for this purpose for as long as SPR has been known to exist. There are good reasons for using these materials: Their plasma frequencies are in the right range to observe plasmonic effects in the visible

spectral range, with sharp, intense peaks. They have mature functionalization chemistries for the construction of biosensors. The frequency of the SPP absorption is very highly angle sensitive compared to less conductive materials like the transparent conducting oxides indium tin oxide (ITO) and aluminum zinc oxide (AZO). In addition, gold is chemically inert, reacting only with very strong acids.

However, there are a number of disadvantages of silver and gold. Both scratch easily, which limits the durability of SPR devices. Silver will tarnish and oxidize over time. Both have the tendency to form islands rather than a continuous film for ultrathin films less than approximately 20 nm thick. Unlike the transparent conducting oxides ITO and AZO, they are opaque. In addition, the bare films are somewhat less suitable for work in the infrared than the visible, because in order to obtain maximum SPR intensity in the near-IR, the films must be made thinner (30-35 nm) compared to the films used in the visible (50-60 nm). This broadens the plasmonic absorption dramatically. Lastly, gold and silver are not normally considered plasmonically tunable in the sense that AZO and ITO are considered tunable by simply controlling the oxygen and doping chemistry [1-3]. Instead, more sophisticated methods such as alloying [4] or the construction of nanoparticle composites [5] must be used to modify the plasmonic response of these noble metals.

Every single one of these disadvantages can be mediated by surrounding the metal film with layers of other materials. For silver-based devices, the improved chemical and mechanical stability has been demonstrated for a number of overlayer materials [6-8], and is a very active area of research in the SPR community. In addition, SPR biosensor device sensitivity can be increased for angle interrogation modes when a dielectric overlayer is used, compared to a plain metallic film [6]. The islanding of deposited metal films is also reduced by using semiconductors or weak conductors like ZnO for adhesion and capping layers [9-11]. Device transparency can be improved relative to plain silver or gold, by making a symmetric sandwich stacking, which creates an interference effect known as induced transmission [12-14] that has been used for many years for heat-reflective windows and transparent electrodes (*cf.* references 23-41 in the work reproduced in section 2.3 [15]).

Lastly, it can be demonstrated that the surrounding films can be used to modulate the SPR response. In Figs. 4.1, and 4.2, the SPR reflectances ( $R_p/R_s$ ) have been theoretically modeled using the multilayer transfer matrix method, for a bare 30 nm silver film (left) and a 20 nm ZnO / 30 nm Ag / 20 nm ZnO multilayer film (right). In Fig. 4.1 the films are on calcium fluoride in water, using a 60° calcium fluoride prism, and in Fig. 4.2 the films are on BK-7 glass in air, using a 60° BK-7 prism.

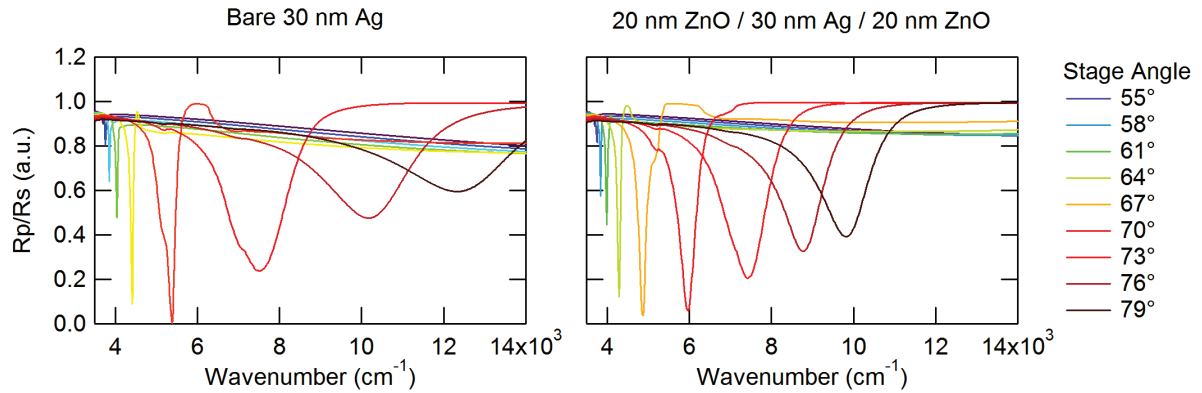


Figure 4.1: Theoretical SPR reflectance ( $R_p/R_s$ ) showing the difference between a bare 30 nm silver film (left) and a 20 nm ZnO / 30 nm Ag / 20 nm ZnO film (right). Both films were modeled on calcium fluoride in water, using a  $60^\circ$  calcium fluoride prism.

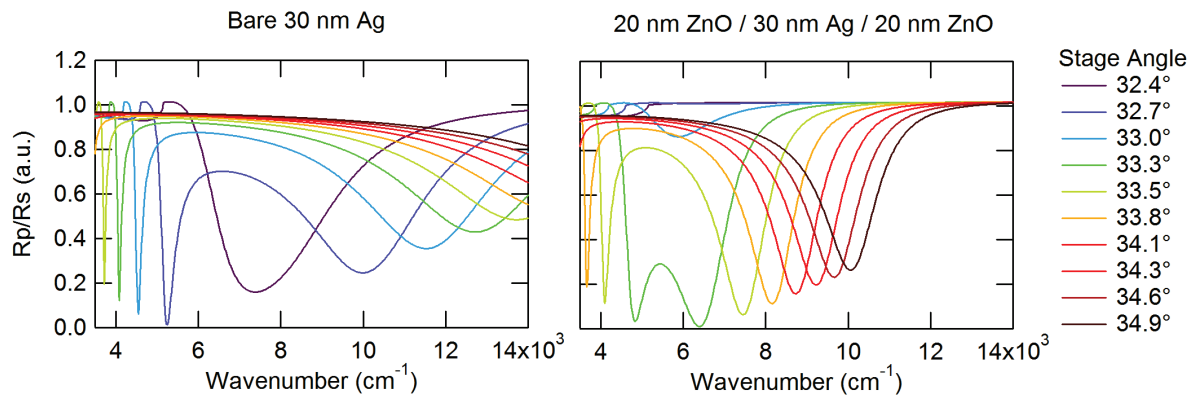


Figure 4.2: Theoretical SPR reflectance ( $R_p/R_s$ ), as in Fig. 2.1 except on glass and in air, showing the difference between a bare 30 nm silver film (left) and a 20 nm ZnO / 30 nm Ag / 20 nm ZnO film (right). Both films were modeled on BK-7 glass in air, using a  $60^\circ$  BK-7 glass prism. The “doubling” of the resonances is due to the glass dispersion, which causes the light’s wavevector to interact with the SPP wavevector at multiple frequencies.

The results are readily apparent: Surrounding the silver with ZnO causes a large shift in the frequencies of the resonances. This is an inherent effect caused mainly by the presence of the ZnO top layer, and is not caused by a change in the properties of the layers themselves, as the bulk dielectric functions have been used for all the layers. It can be described as the change in the surface plasmon polariton wavevector ( $k_{spp}$ ) arising from change in the dielectric function of the ambient medium at the SPR-active interface ( $\epsilon_A$ ), in the same manner that SPR biosensors operate. The relationship between  $k_{spp}$  and  $\epsilon_A$  is given in Eq. (4.1), where  $\epsilon_B$  is the complex dielectric function of the conductor. The ZnO has a significantly higher dielectric function  $\epsilon_A$  than either the water in Fig. 4.1 or the air in Fig. 4.2, which shifts  $k_{spp}$  and thus the resonances. The difference is greater in going from air to ZnO than from water to ZnO, and so the shifts in Fig. 4.2 are greater than in Fig. 4.1.

$$k_{spp} = \frac{\omega}{c} \sqrt{\frac{\epsilon_A \epsilon_B}{\epsilon_A + \epsilon_B}} \quad (4.1)$$

This simple explanation is only partially accurate, however, because there is a dependence on the thicknesses of the ZnO layers. The multilayer reflection model, introduced in section 1.2.2 of this work, must be used to account for these effects. From the theoretical model, we can predict that the bottom layer thickness has very little effect on the SPR spectra until the thickness approaches the wavelength of the light, at which point interference effects begin to appear (Fig. 4.3A). In comparison, the top ZnO layer thickness has a much greater effect on the SPR spectra (Fig. 4.3B). Comparing Fig. 4.3B to Fig. 4.2, it is evident that the silver SPR wavevector can be tuned over a very large spectral range by controlling the thickness and composition of an overlayer material.

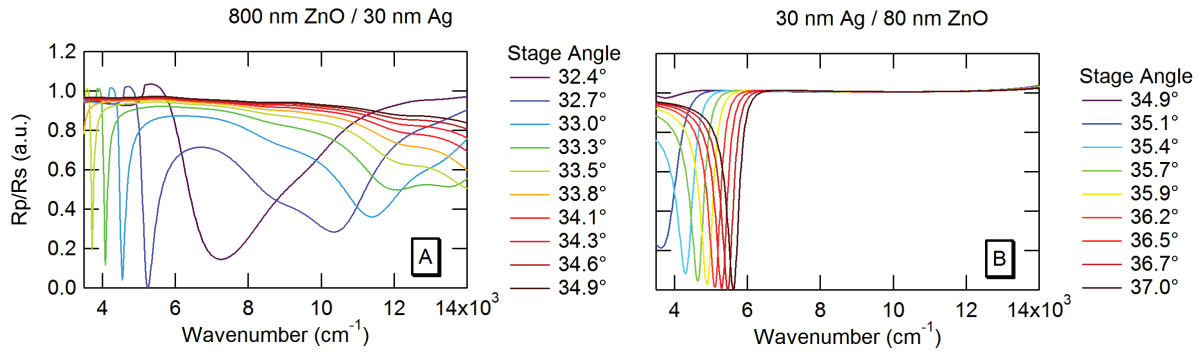


Figure 4.3: Theoretical FT-SPR spectra of (A): a 30 nm Ag film with an 800 nm ZnO underlayer, showing the onset of interference effects compared to Fig. 4.2, and (B): a 30 nm Ag film with an 80 nm ZnO overlayer, showing the high dependence on the thickness of the ZnO top layer. Note that unlike previous figures, the angle ranges for the left and right sides of this figure are different.

The plasmonic tuning and other benefits associated with these films are potentially very valuable to the SPR community, for the reasons already mentioned. Therefore, we are interested in the development of a reliable deposition method. The films' SPR response, as the primary effect of interest, was used as the primary characterization metric, in addition to the usual thin-film characterization methods.

Previously, pulsed DC reactive magnetron sputtering was used to deposit these sandwich structure thin films for use in SPR [15]. For the current work, the film deposition methods were developed via pulsed laser deposition (PLD) in a single-chamber process. PLD was used instead of another deposition process for a couple of reasons. First, the PLD system was capable of handling multiple targets, which eased development of the single-chamber process. This allowed the samples to be kept in vacuum between layers, which was believed to help prevent islanding of the silver films [15]. Second, it is known that high-quality ZnO-based films (e.g. AZO, GZO) can be fabricated with ease via PLD with little or no substrate heating [16-23].

In this work, both BK-7 glass and calcium fluoride substrates have been used. Although the substrate material can certainly play a role in the crystallinity of ZnO-based materials [3, 23-25], films for SPR need only be optically uniform on a micrometer-length scale. Similar results were observed on both substrates with good reproducibility. The substrate may become important for later work, however, as the deposition process is refined.

## 4.2 Experiment

### 4.2.1 Film depositions

Targets of AZO and ZnO were fabricated using the sintered oxide method. Powdered ZnO (99.9%, Alfa Aesar) and  $\alpha$ -Al<sub>2</sub>O<sub>3</sub> (99.99%, Alfa Aesar) were mixed in the appropriate ratios and ball milled in ethanol for 1 hour. The mixture was separated and allowed to dry overnight. The powder was then die-pressed into 1.25 inch diameter pellets at 8000 psi, which were sintered in an oven at 1250-1350 °C for 3 hours, or 8 hours for the undoped target. Three targets were used for this study: undoped ZnO, 3at% Al-doped ZnO, and 4at% Al-doped ZnO.

Film depositions took place via a single-chamber PLD process using a KrF excimer laser (248 nm wavelength, Coherent COMPex Pro 102F). The AZO or ZnO target of choice and a target of Ag (99.99%, Kurt Lesker, Inc.) were each pre-ablated for 1000 pulses at 7 Hz in low vacuum ( $\sim 1 \times 10^{-4}$  Torr) to remove contaminants before depositions. The sapphire window to the chamber was cleaned after each film deposition using aqua regia and UV ozonolysis. The glass, sapphire, and CaF<sub>2</sub> substrates were cleaned using UV ozonolysis immediately before deposition. For both the AZO and ZnO layers, the deposition settings were as follows. The targets were rotated and a rocking mirror was used to raster the laser beam over as much of the target area as possible, in order to increase film uniformity and target consumption. The laser energy setting was 250 mJ, which produced approximately 180 mJ inside the chamber as measured by a laser energy meter (Coherent LabMax TOP). The substrates were not heated during deposition. Background pressure was allowed to reduce to  $\sim 2 \times 10^{-5}$  Torr before each deposition. For the AZO and ZnO layers only, additional deposition parameters were as follows. The spot size on the target was a rounded rectangle

with dimensions of approximately 6.7mm×2.5mm, producing an energy density of approximately 1.1 J cm<sup>-2</sup>. The target-substrate distance was 10 cm. The films were deposited in an O<sub>2</sub> environment that varied from 1 to 20 mTorr, which allowed the oxygen vacancies in the films to be systematically controlled. Oxygen vacancies are a major source of charge carriers in ZnO-based materials, which allows the conductivities to be systematically controlled. For the silver layers, additional deposition parameters were as follows. The spot size on the target was a rounded rectangle with dimensions of approximately 3.6mm×1.7mm, producing an energy density of approximately 2.9 J cm<sup>-2</sup>. The target-substrate distance was 6 cm. The films were deposited in vacuum.

Deposition rates were calculated on both monolithic films and multilayer films via measurement of film thicknesses with stylus profilometry. For the deposition rates, no statistical difference was found between the top and bottom layer films of AZO, nor between the films deposited individually for both AZO and Ag. In addition, O<sub>2</sub> pressure did not have a statistically significant effect on the deposition rates of AZO. The rates were as follows: 4at% Al:ZnO, 0.0314 nm/pulse ± 5.3%; 3at% Al:ZnO, 0.0305 nm/pulse ± 11.1%; undoped ZnO, 0.0266 nm/pulse ± 11.4%; Ag, 0.00879 nm/pulse ± 25.3%. The uncertainties in these values are high, and so it is likely that the reported thicknesses are moderately inaccurate.

The use of varying Al doping concentrations along with varying oxygen pressures during deposition of the AZO or ZnO layers permitted systematic variation of the AZO or ZnO plasma frequencies and resistivities. A series of sandwich films were produced in this manner on both the BK-7 glass and CaF<sub>2</sub> substrates to assess this effect on the SPR responses. Four (for CaF<sub>2</sub>) or five (for glass) deposition parameters were used, which are listed in Table 4.1. In addition, the resistivities of pure AZO films (in the absence of Ag) deposited by these methods were assessed by a four-point probe. The AZO / Ag / AZO film thicknesses were attempted to be held at 80 nm / 20 nm / 80 nm, but after repetitions of the thickness measurements by stylus profilometry, the averages of the deposition rates changed slightly.

**Table 4.1: Methodology for the AZO / Ag / AZO sandwich films and sheet resistances for pure AZO deposited by the same method.**

<b>Method / Figure Name</b>	<b>Al doping (at%)</b>	<b>O2 pressure (mTorr)</b>
A	0	20.0
C	3	20.0
E	4	10.0
G	3	10.0
I	4	2.0

#### 4.2.2 SPR analysis

Two fourier-transform surface plasmon resonance (FT-SPR) spectrometers were used to analyze the films. In both, the Kretschmann configuration was used [26], in which the film was deposited onto a particular substrate material, which was then adhered to an equilateral prism of the same material using an index matching fluid. The choice of substrate and prism material and the external medium varied from instrument to instrument, according to the angle and frequency ranges that were available.

Instrument 1 was comprised of a  $\theta$ - $2\theta$  stage attachment (GWC Technologies, Inc.) connected to the external beam port of a Thermo Scientific FT-IR spectrometer. The substrate and prism materials were BK-7 glass, and the ambient material was air. The index matching fluid was Cargille Series M 1.52. The stage attachment used the light source, software, and CaF<sub>2</sub> beam splitter of the spectrometer, but contained separate polarizer and extended-range InGaAs detector.

Instrument 2 was a variable angle SPR accessory that was designed to fit inside the measurement chamber of a Bruker FT-IR spectrometer [27]. The substrate and prism materials were calcium fluoride, and the ambient material was water. The index matching

fluid was Cargille Series M 1.42. The accessory used the light source, software, CaF<sub>2</sub> beamsplitter, and detectors (liquid N<sub>2</sub>-cooled mercury cadmium telluride, and InGaAs) of the spectrometer, with a separate polarizer.

#### 4.2.3 Theoretical modeling

The SPR responses were modeled using the multilayer transfer matrix method for reflectance, which is described in detail in section 1.2.2. A Matlab software package for SPR containing this method is available on the Mathworks File Exchange site [28]. The method computes the reflectance by considering the boundary conditions that govern the transfer of the electric and magnetic fields through each interface, and also the phase changes as the light traverses each material. The dielectric function of each material in the spectral region of interest is required, and the layers are assumed to be perfectly parallel, homogeneous, and non-magnetic.

The AZO dielectric function was modeled as a hybrid between the Drude model and bulk ZnO dielectric functions, by replacing the high-frequency dielectric constant  $\epsilon_\infty$  with the bulk dielectric function  $\epsilon_{bulk}$ :

$$\epsilon_{AZO} = \epsilon_{bulk}(\omega) - \frac{\omega_p^2}{\omega^2 + i\omega\Gamma} \quad (4.2)$$

The ZnO bulk dielectric function was obtained by taking the average of the ordinary and extraordinary dielectric functions at each frequency, as measured by Bond [29]. The bulk ZnO dielectric function is then linear, with an equation of  $\epsilon_{bulk} = 1.93 \times 10^{-5} \omega$  ( $/\text{cm}^{-1}$ ) + 3.62. The Drude parameters  $\omega_p$  and  $\Gamma$  in Eq. (4.2) were estimated from the experimental results of each film. The silver was modeled as bulk. In these frequency ranges, the bulk silver dielectric function fits the Drude model very well, with the values  $\epsilon_\infty=2.65$ ,  $\omega_p=70619 \text{ cm}^{-1}$ , and  $\Gamma=399 \text{ cm}^{-1}$ , which were obtained by the method described in [15]. The calcium fluoride dielectric function was obtained by spectroscopic ellipsometry and then cubic spline interpolated. The BK-7 glass dielectric function was obtained from the Esco Optics, Inc. website [30] and then cubic spline interpolated. The water dielectric function was obtained

from Segelstein [31], and the real and imaginary parts were cubic spline interpolated. The air dielectric function was assumed to be constant and real 1.000569.

Figure 4.4: AZO plasma frequency series for Instrument 1, for the films on BK-7 glass in air, showing experimental results (left) and theoretical results (right). (A, B): Undoped ZnO, deposited at 20.0 mTorr O<sub>2</sub>. Thicknesses 91.8 / 25.0 / 91.8 nm. ZnO  $\omega_p=5000\text{ cm}^{-1}$ ,  $\Gamma=2000\text{ cm}^{-1}$ . (C, D): 3at% Al AZO, deposited at 20.0 mTorr O<sub>2</sub>. Thicknesses 84.9 / 25.0 / 84.9 nm. AZO  $\omega_p=7000\text{ cm}^{-1}$ ,  $\Gamma=2000\text{ cm}^{-1}$ . (E, F): 4at% Al AZO, deposited at 10.0 mTorr O<sub>2</sub>. Thicknesses 87.6 / 25.0 / 87.6 nm. AZO  $\omega_p=9000\text{ cm}^{-1}$ ,  $\Gamma=2000\text{ cm}^{-1}$ . (G, H): 3at% Al AZO, deposited at 10.0 mTorr O<sub>2</sub>. Thicknesses 84.9 / 25.0 / 84.9 nm. AZO  $\omega_p=10000\text{ cm}^{-1}$ ,  $\Gamma=2000\text{ cm}^{-1}$ . (I, J): 4at% Al AZO, deposited at 2.0 mTorr O<sub>2</sub>. Thicknesses 76.7 / 20.0 / 76.7 nm. AZO  $\omega_p=12000\text{ cm}^{-1}$ ,  $\Gamma=2000\text{ cm}^{-1}$ . Discrepancies between theory and experiment are most likely due to error in measured thicknesses.

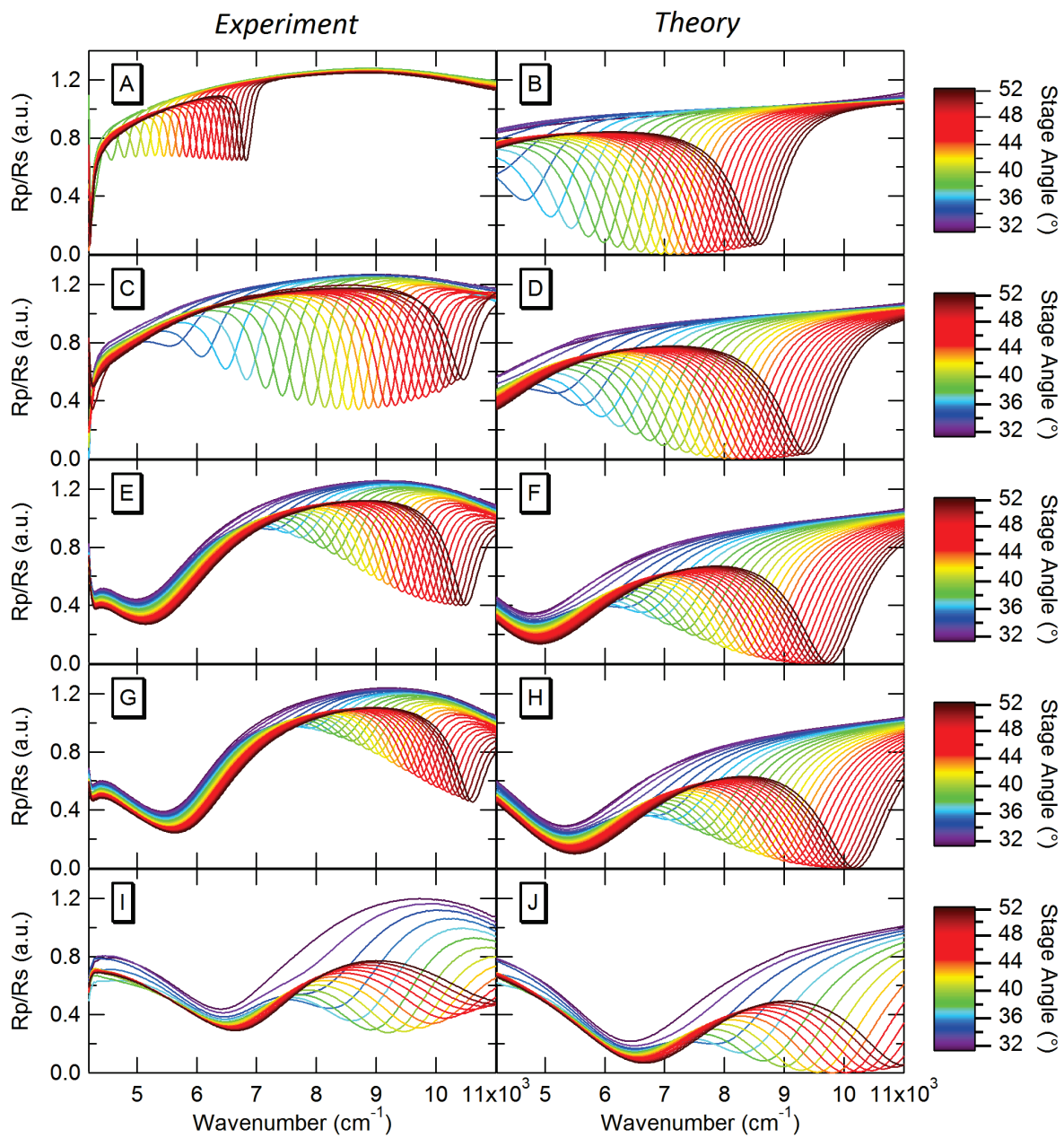
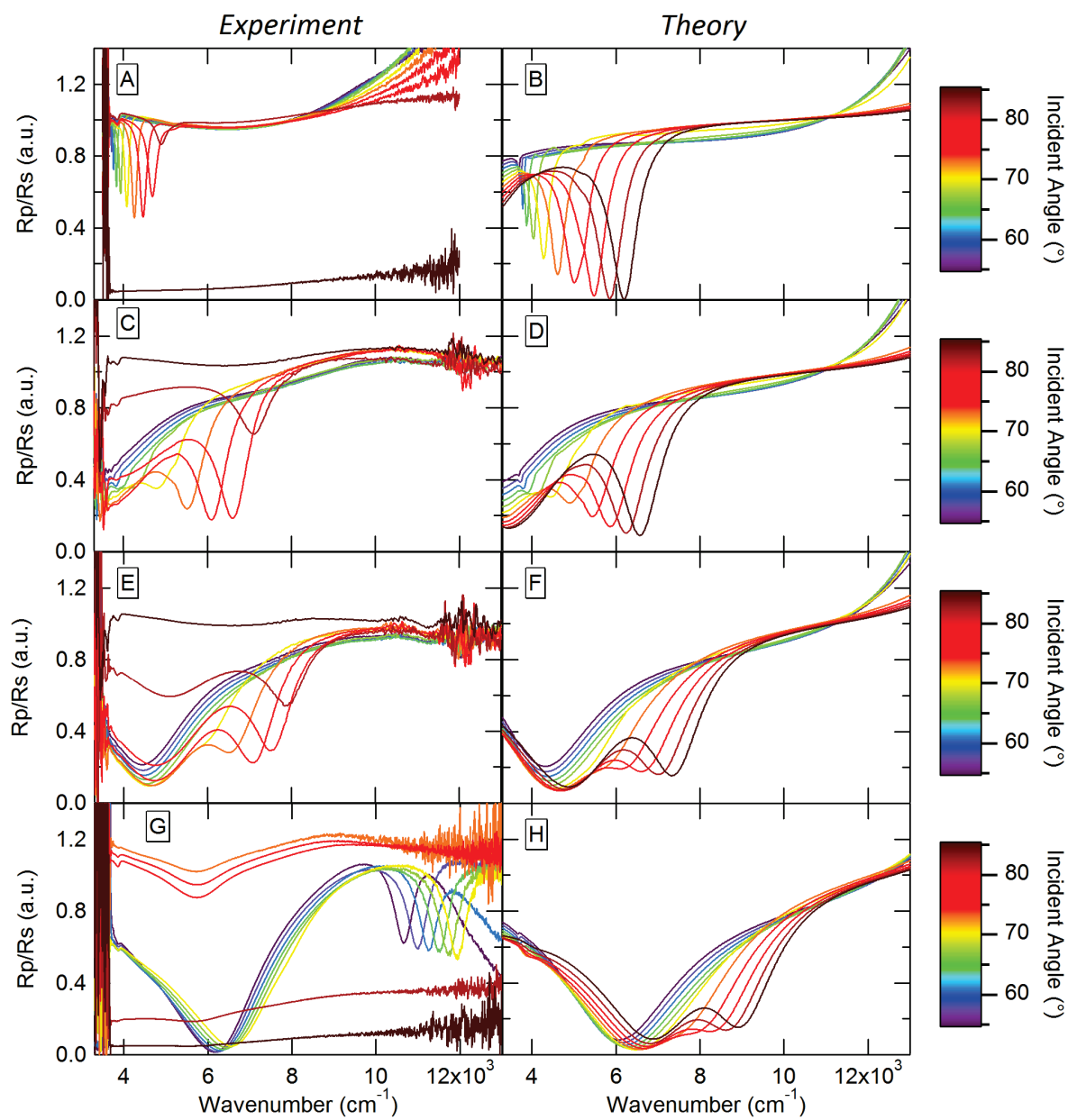


Figure 4.5: AZO plasma frequency series for Instrument 2, for the films on CaF<sub>2</sub> in water, showing experimental results (left) and theoretical results (right). (A, B): Undoped ZnO, deposited at 20.0 mTorr O<sub>2</sub>. Thicknesses 80.0 / 25.0 / 80.0 nm. ZnO  $\omega_p=4000\text{ cm}^{-1}$ ,  $\Gamma=2000\text{ cm}^{-1}$ . (C, D): 3at% Al AZO, deposited at 20.0 mTorr O<sub>2</sub>. Thicknesses 84.9 / 25.0 / 84.9 nm. AZO  $\omega_p=6000\text{ cm}^{-1}$ ,  $\Gamma=2000\text{ cm}^{-1}$ . (E, F): 4at% Al AZO, deposited at 10.0 mTorr O<sub>2</sub>. Thicknesses 87.6 / 25.0 / 87.6 nm. AZO  $\omega_p=8000\text{ cm}^{-1}$ ,  $\Gamma=2000\text{ cm}^{-1}$ . (G, H): 3at% Al AZO, deposited at 10.0 mTorr O<sub>2</sub>. Thicknesses 84.9 / 25.0 / 84.9 nm. AZO  $\omega_p=11000\text{ cm}^{-1}$ ,  $\Gamma=2000\text{ cm}^{-1}$ .



### 4.3 Results

Figures 4.4 and 4.5 show the results of the experimental SPR measurements (left side) and theoretical modeling (right side) of the AZO plasma frequency series. The film deposition methods for Fig. 4.5 A-H correspond to Fig. 4.4 A-H. The figure names for the experimental measurements correspond to the method names (A, C, E, G, and I) in Table 4.1.

Two primary features are seen in the spectra of Figs. 4.4 and 4.5. First, the highly angle-dependent feature is the surface plasmon polariton associated with the silver. The experimental-theoretical match can be seen to be highly dependent on the sample. This variability will be addressed in the discussion section. Second, the broad angle independent feature that appears as the AZO plasma frequency is increased can be identified as the quasi-bound mode (QBM) from the bottom AZO layer. In the theoretical modeling, the AZO dielectric function must be adjusted by the two parameters  $\omega_p$  and  $\Gamma$  in Eq. (4.2). The values of these parameters, which are listed in Table 4.2, were estimated by the experimental-theoretical match of the QBM feature. These values can be used to calculate the film resistivities, using the relation:

$$\rho = (n\mu e)^{-1} = \frac{\Gamma}{\omega_p^2 \epsilon_0}. \quad (4.3)$$

These calculated resistivities are listed in Table 4.3, along with the measured resistivities of pure AZO films deposited by the same methods.

**Table 4.2: AZO Drude term parameters  $\omega_p$  and  $\Gamma$  for the AZO layers, in the right hand sides of Figs. 4.4 and 4.5.**

<b>Figure Name</b>	<b>BK-7 AZO <math>\omega_p</math> (cm-1)</b>	<b>BK-7 AZO <math>\Gamma</math> (cm-1)</b>	<b>CaF2 AZO <math>\omega_p</math> (cm-1)</b>	<b>CaF2 AZO <math>\Gamma</math> (cm-1)</b>
B	5000	2000	4000	2000
D	7000	2000	6000	2000
F	9000	2000	8000	2000
H	10000	2000	11000	2000
J	12000	3000	N/A	N/A

**Table 4.3: The AZO resistivities, as measured by four-point probe and as calculated from the optical parameters listed in Table 4.2.**

<b>Method / Figure Name</b>	<b>Measured AZO <math>\rho</math> (m<math>\Omega</math> cm)</b>	<b>Calculated AZO <math>\rho</math>, BK-7 (m<math>\Omega</math> cm)</b>	<b>Calculated AZO <math>\rho</math>, CaF2 (m<math>\Omega</math> cm)</b>
A / B	Over limit	4.80	7.49
C / D	8.91	2.45	3.33
E / F	1.94	1.48	1.87
G / H	4.31	1.20	0.991
I / J	1.16	1.25	N/A

There are also several less prominent features in the spectra. First, for the films on BK-7 glass (Fig. 4.4), the experimental spectra have a substantially curved background that is not accounted for in the theoretical model. This curved background is believed to be caused by differences in detector sensitivity for the two polarizations. Second, for the films on calcium fluoride (Fig. 4.5), with the exception of Film G, there is a dramatic reduction in signal intensity at the two highest angles. This can be attributed to the sample geometry. At the

highest angles, which reach up to  $85^\circ$ , the light is at glancing incidence. Only a portion of the light ray actually makes it to the thin film, while the rest is reflected from the prism surfaces and the edges of the sample substrate.

#### 4.4 Discussion

Before discussing the surface plasmon polariton features, we will discuss the AZO quasi-bound mode (QBM) features. First, we note that the feature is due entirely to the bottom AZO layer. The top AZO layer does not contribute to this feature, and if the bottom layer is removed, the feature disappears completely. Second, we can identify this as the QBM, as opposed to a true surface plasmon polariton mode, because for each of the resonances seen, at the frequencies that the resonance appears, the AZO dielectric function  $\epsilon_{AZO}$  is positive, which eliminates the condition necessary for SPP formation [32]. Third, the feature is related to the zero-crossing of the real part of the dielectric function, and so it tracks the AZO plasma frequency, and thus the material's resistivity by Eq. (4.3). As seen in Table 4.3, the resistivity estimates by this method are the same order of magnitude as the measured resistivities. However, the relationship is imprecise.

Next, we will discuss the silver surface plasmon polariton features. In Figs. 4.4 and 4.5, there is a wide range of variability in the experimental-theoretical matches. Due to this variability, the differences in the experimental setups between the BK-7 glass set and the  $\text{CaF}_2$  set, and the measurement artifacts of the curved background and the signal reduction at glancing incidence, any quantitative comparison of the spectra will add little value to the discussion. We therefore will limit the discussion to qualitative comparisons.

When comparing experiment to theory, we first compare the frequencies of each resonance at each given angle, combined with the overall spacing between the resonances. Parameters that affect resonance frequency include the thickness of the AZO top layer, and the angles of incidence. Then, the intensities are compared. The relative intensities of the resonances to each other are more important than the absolute intensities, which may be reduced by other effects in the system such as scattering that the model does not consider. The primary factor affecting relative intensities is the thickness of the silver layer, although

the AZO top layer thickness also has a minor effect. Lastly, the widths of the resonances can be compared. Both the Ag and AZO top layer thicknesses contribute to the peak widths.

There are several other parameters that can contribute to the spectra that can be eliminated. First, the silver dielectric function was assumed to be that of bulk silver. Any deviation from the bulk dielectric function would most likely arise from grain boundary scattering in the film, which is assumed to be polycrystalline, which would increase the damping constant for the silver  $\Gamma_{\text{Ag}}$  and cause the SPR resonances to become more broad and less intense. While it is likely that this grain boundary scattering is present in the silver layer, as a consequence of the assumed polycrystalline film, its effects on the SPR spectra are minor compared to the effects of the Ag thickness and AZO top layer thickness. Second, the dielectric functions of the semi-infinite materials (BK-7 glass,  $\text{CaF}_2$ , water, and air) were assumed to be exactly as reported in section 4.2.3. Deviations from the reported values could conceivably arise for the BK-7 and  $\text{CaF}_2$  based on the manufacturing process. Although these deviations are likely to be small, these dielectric functions can have significant effects on the spectra, and so it may be necessary in the future to measure the dielectric functions for each film substrate.

For the films on BK-7 glass (Fig. 4.4), we can make several comparisons of the Ag surface plasmon polariton resonances. First, the resonances of films C, E, and G are seen to differ in a number of respects from the theoretical prediction. Each is more narrow, has a lower absolute intensity, and is at slightly different frequencies than the theoretical model would predict. For film I, the measured resonances are slightly broader and the relative intensities are different than the model predicts. For these four films C, E, G, and I, the discrepancies between the experimental and theoretical results can be greatly improved by minor adjustments in film thicknesses. As an example, this has been performed for film C in Fig. 4.6, with the adjusted film thicknesses of 73 nm / 28 nm / 73 nm for AZO / Ag / AZO. Compared to the original thicknesses of 84.9 nm / 25.0 nm / 84.9 nm, the adjusted AZO thickness falls only 2.5 nm outside of the rate standard deviation of 11.1%, while the Ag thickness falls within the rate standard deviation of 25.3%. Similar results can be obtained for films E, G, and I, and this would lead us to naively conclude that the measured thicknesses

are inaccurate. However, this explanation is not satisfactory for film A (Fig. 4.7). The thicknesses required to match the theory B to the experiment A are 130 nm / 40 nm / 130 nm for AZO / Ag / AZO, which compared to the original thicknesses of 91.8 nm / 25.0 nm / 91.8 nm are well outside the standard deviation range. In addition, at these thicknesses, artifacts begin to appear at high frequencies that are not seen in the experimental spectrum (Fig. 4.7). Adjustments to the incident angle are also not sufficient to explain the spectrum of film A. We conclude, therefore, that at least for film A and possibly for all the films on glass, the anomalous effects seen in the experimental spectra must be caused by some additional effect that has not yet been considered, possibly related to the film's microstructure.

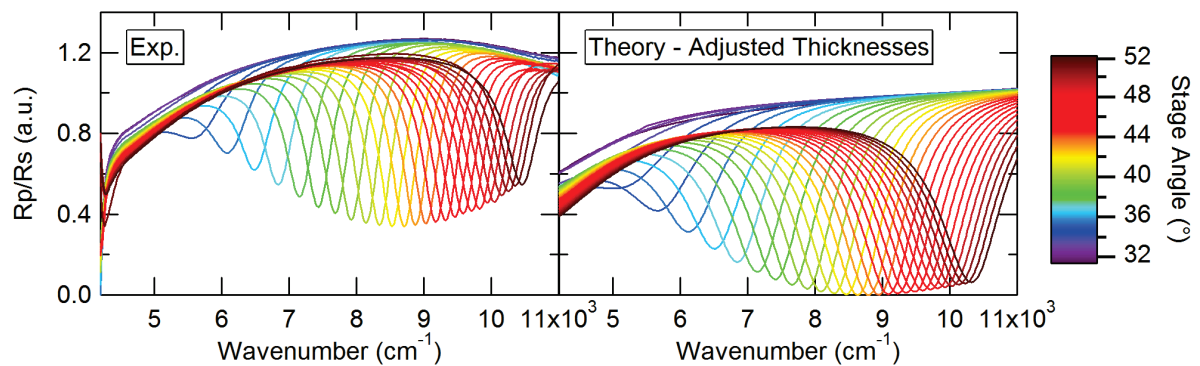


Figure 4.6: The experimental SPR spectrum of Film C on glass (left), compared to the theoretical spectrum that is obtained when the thicknesses are adjusted to 73 nm / 28 nm / 73 nm for AZO / Ag / AZO (right).

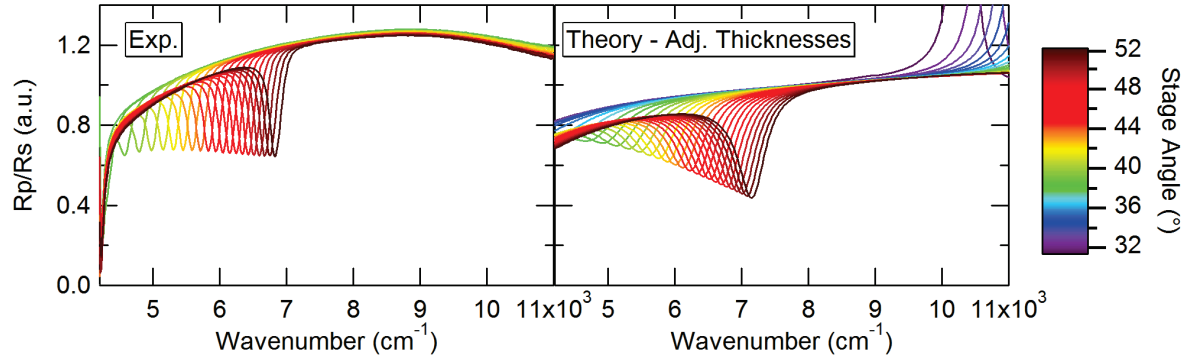


Figure 4.7: The experimental SPR spectrum of Film A on glass (left), compared to the theoretical spectrum that is obtained when the thicknesses are adjusted to 130 nm / 40 nm / 130 nm for AZO / Ag / AZO (right).

Similar conclusions can be drawn from the films on  $\text{CaF}_2$  (Fig. 4.5). As mentioned before, the dramatic reduction in intensity at high angles is due to the limitations of the sample geometry at glancing incidence. With the exception of this geometric effect, the theoretical spectra B, D, and F can each be matched very well to the experimental spectra A, C, and E by minor adjustments in the film thicknesses. However, for film G, the resonances seen at  $11000\text{-}12000\text{ cm}^{-1}$  cannot be explained by the simple theory. Unlike the film A on glass, however, the theory does not even come close to a satisfactory explanation. To test the film preparation methods, a duplicate of film G on  $\text{CaF}_2$  was synthesized, with different results. On the duplicate, no surface plasmon polariton resonances were seen at any angle, and only the AZO quasi-bound mode was observed. We conclude that some unreliability remains in the film deposition protocol.

#### 4.5 Conclusions

Trilayer films of aluminum-doped zinc oxide (AZO) / Ag / AZO were fabricated on calcium fluoride and BK-7 glass substrates using pulsed laser deposition (PLD). As a research tool, PLD is a good choice because it allows good control over a large number of deposition

parameters. However, with more variables to control, the films that are produced are also more variable, as we have observed in these results.

The films were analyzed via surface plasmon resonance (SPR) spectroscopy in two separate instruments with similar results. Because of the high sensitivity of SPR spectroscopy, this is notable. The instruments operated at very different angle ranges, with different substrate refractive indices, and very different ambient environments. The instruments operated in much of the same frequency range, however, and thus can be considered complimentary in many respects. For many of the films, good quality was observed on both the amorphous BK-7 glass substrates and the cubic crystalline calcium fluoride substrates. However, effects of the substrate on the films may become a concern as the deposition techniques are refined. In addition, ZnO-based materials are known to be moisture sensitive [33, 34], and while we have not observed significant degradation of the materials in these experiments, it could limit the durability or alter the SPR responses of the films over time.

The AZO layers were fabricated with varying Al doping concentrations and in varying oxygen environments, which allowed control of the AZO plasma frequency. This allowed the AZO plasmonic quasi-bound mode (QBM) to be tuned over a range of frequencies. The AZO plasma frequencies and damping frequencies were obtained from the theoretical spectra and were used to calculate the AZO resistivities, which were the same order of magnitude as the resistivities measured via four-point probe on pure AZO films. In Table 4.3, we can see that the measured AZO resistivity bears only a loose correlation to the plasma frequency. The origin of the variability in these numbers is uncertain, but note that the film thickness is required to convert the sheet resistance, as measured by four-point probe, into resistivity, which may explain at least part of the variance.

The highly angle-dependent silver surface plasmon polariton (SPP) mode was also observed, and was compared qualitatively to the theoretical models. For most films, the experimental-theoretical match was good, but could be significantly improved by minor adjustments to film thicknesses. Deposition rates from stylus profilometry had a high standard deviation, which gives validity to these adjustments. However, SPP results for two

films, film A on glass and film G on CaF<sub>2</sub>, were highly inconsistent with the theoretical models, even with extreme thickness adjustments. This indicated that additional confounding effects may be present, possibly from experimental variations in the film fabrication procedures.

#### 4.6 Acknowledgments

I would like to thank Edward Sachet for the undoped ZnO target and for the CaF<sub>2</sub> dielectric function, J.-P. Maria for the use of the PLD system and other instruments, and the Booksh lab at the University of Delaware for the use of their SPR instrument, substrates, and time. This work was funded by NSF grants 1112017 and 1111618.

#### 4.7 References

1. M. Losego, A. Efremenko, C. Rhodes, M. Cerruti, S. Franzen, and J. Maria, "Conductive oxide thin films: Model systems for understanding and controlling surface plasmon resonance," *Journal of Applied Physics* **106**, 024903 (2009).
2. C. Rhodes, S. Franzen, J. Maria, M. Losego, D. Leonard, B. Laughlin, G. Duscher, and S. Weibel, "Surface plasmon resonance in conducting metal oxides," *Journal of Applied Physics* **100**, 054905 (2006).
3. E. Sachet, M. Losego, J. Guske, S. Franzen, and J. Maria, "Mid-infrared surface plasmon resonance in zinc oxide semiconductor thin films," *Applied Physics Letters* **102**, 051111 (2013).
4. D. Bobb, G. Zhu, M. Mayy, A. Gavrilenko, P. Mead, V. Gavrilenko, and M. Noginov, "Engineering of low-loss metal for nanoplasmonic and metamaterials applications," *Applied Physics Letters* **95** (2009).
5. R. Gerber, D. Leonard, and S. Franzen, "Conductive thin film multilayers of gold on glass formed by self-assembly of multiple size gold nanoparticles," *Thin Solid Films* **517**, 6803-6808 (2009).

6. S. Szunerits, A. Shalabney, R. Boukherroub, and I. Abdulhalim, "Dielectric coated plasmonic interfaces: their interest for sensitive sensing of analyte-ligand interactions," *Reviews in Analytical Chemistry* **31**, 15-28 (2012).
7. G. Hass, J. B. Heaney, H. Herzig, J. F. Osantowski, and J. J. Triolo, "Reflectance and durability of Ag mirrors coated with thin layers of Al<sub>2</sub>O<sub>3</sub> plus reactively deposited silicon oxide," *Applied Optics* **14**, 2639-2644 (1975).
8. E. Širbegović, I. Tucak, and M. Čevro, "An investigation of the durability of front surface Ag mirrors using oxide protecting layers," *Vacuum* **43**, 763-765 (1992).
9. F. Didier, and J. Jupille, "Simple Views on Metal/Oxide Interfaces: Contributions of the Long-Range Interactions to the Adhesion Energy," *The Journal of Adhesion* **58**, 253-261 (1996).
10. A. M. Stoneham, "Systematics of metal-insulator interfacial energies: A new rule for wetting and strong catalyst-support interactions," *Applications of Surface Science* **14**, 249-259 (1983).
11. G. T. West, P. J. Kelly, and J. W. Bradley, "A Comparison of Thin Silver Films Grown Onto Zinc Oxide via Conventional Magnetron Sputtering and HiPIMS Deposition," *Plasma Science, IEEE Transactions on* **38**, 3057-3061 (2010).
12. P. H. Berning, and A. F. Turner, "Induced Transmission in Absorbing Films Applied to Band Pass Filter Design," *J. Opt. Soc. Am.* **47**, 230-239 (1957).
13. T. W. Allen, and R. G. DeCorby, "Assessing the maximum transmittance of periodic metal-dielectric multilayers," *J. Opt. Soc. Am. B* **28**, 2529-2536 (2011).
14. H. A. Macleod, *Thin-film optical filters* (CRC Press/Taylor & Francis, Boca Raton, FL, 2010).

15. J. Guske, J. Brown, A. Welsh, and S. Franzen, "Infrared surface plasmon resonance of AZO-Ag-AZO sandwich thin films," *Optics Express* **20**, 23215-23226 (2012).
16. A. Singh, R. Mehra, N. Buthrath, A. Wakahara, and A. Yoshida, "Highly conductive and transparent aluminum-doped zinc oxide thin films prepared by pulsed laser deposition in oxygen ambient," *Journal of Applied Physics* **90**, 5661-5665 (2001).
17. N. A. Estrich, Gallium-Doped Zinc Oxide as a Conductive Antireflection Coating for Silicon Solar Cell Applications (North Carolina State University, [Raleigh, North Carolina], 2012).
18. A. Suzuki, T. Matsushita, N. Wada, Y. Sakamoto, and M. Okuda, "Transparent Conducting Al-Doped ZnO Thin Films Prepared by Pulsed Laser Deposition," *Japanese Journal of Applied Physics* **35**, L56-L59 (1996).
19. G. A. Hirata, J. McKittrick, J. Siqueiros, O. A. Lopez, T. Cheeks, O. Contreras, and J. Y. Yi, "High transmittance--low resistivity ZnO:Ga films by laser ablation," (AVS, Mineapolis, Minnesota (USA), 1996), pp. 791-794.
20. M. Hiramatsu, K. Imaeda, N. Horio, and M. Nawata, "Transparent conducting ZnO thin films prepared by XeCl excimer laser ablation," *Journal of Vacuum Science & Technology A: Vacuum, Surfaces, and Films* **16**, 669-673 (1998).
21. R. Mehra, A. Singh, M. Kumar, A. Yoshida, V. Kumar, and S. Agarwal, "Transparent conducting ZnO : Al thin films prepared by ArF excimer laser ablation," *Proceeding of the Tenth International Workshop on the Physics of Semiconductor Devices, Vols I and II* **3975**, 1198-1205 (2000).
22. H. Kim, C. Gilmore, J. Horwitz, A. Pique, H. Murata, G. Kushto, R. Schlaf, Z. Kafafi, and D. Chrisey, "Transparent conducting aluminum-doped zinc oxide thin films for organic light-emitting devices," *Applied Physics Letters* **76**, 259-261 (2000).

23. H. Kim, J. Horwitz, S. Qadri, and D. Chrisey, "Epitaxial growth of Al-doped ZnO thin films grown by pulsed laser deposition," *Thin Solid Films* **420**, 107-111 (2002).
24. J. Mass, P. Bhattacharya, and R. S. Katiyar, "Effect of high substrate temperature on Al-doped ZnO thin films grown by pulsed laser deposition," *Materials Science and Engineering: B* **103**, 9-15 (2003).
25. M. Karger, and M. Schilling, "Epitaxial properties of Al-doped ZnO thin films grown by pulsed laser deposition on SrTiO<sub>3</sub>(001)," *Physical Review B* **71**, 075304 (2005).
26. E. Kretschmann, and H. Raether, "Radiative decay of non radiative surface plasmons excited by light," *Zeitschrift Fur Naturforschung Part a-Astrophysik Physik Und Physikalische Chemie A* **23**, 2135 (1968).
27. N. Menegazzo, L. Kegel, Y. Kim, D. Allen, and K. Booksh, "Adaptable infrared surface plasmon resonance spectroscopy accessory," *Review of Scientific Instruments* **83** (2012).
28. J. T. Guske, "SPR XPhase," (2013),  
<http://www.mathworks.com/matlabcentral/fileexchange/41090>.
29. W. L. Bond, "Measurement of the Refractive Indices of Several Crystals," *Journal of Applied Physics* **36**, 1674-1677 (1965).
30. Esco Optics Inc., "BK-7 Optical Glass," <http://www.escooptics.com/material-data/bk7-optical-glass>, Accessed April 4, 2013.
31. D. J. Segelstein, "The complex refractive index of water," Masters Thesis, (Department of Physics. University of Missouri-Kansas City, Kansas City, 1981).
32. S. A. Maier, *Plasmonics: fundamentals and applications* (Springer, New York, 2007).

33. Y. Kishimoto, O. Nakagawara, H. Seto, Y. Koshido, and Y. Yoshino, "Improvement in moisture durability of ZnO transparent conductive films with Ga heavy doping process," *Vacuum* **83**, 544-547 (2008).
34. O. Nakagawara, Y. Kishimoto, H. Seto, Y. Koshido, Y. Yoshino, and T. Makino, "Moisture-resistant ZnO transparent conductive films with Ga heavy doping," *Applied Physics Letters* **89** (2006).

## 5. Infrared AZO surface plasmon resonance: relation to material properties

Thin conductive films of aluminum-doped zinc oxide (AZO) were prepared by pulsed laser deposition (PLD) on CaF<sub>2</sub> substrates for an infrared surface plasmon resonance (SPR) study. The films' SPR response in the Kretschmann configuration was studied in air in the near-IR, and in water in the mid-IR. Their charge carrier densities  $n$  and mobilities  $\mu$  were determined via Hall Effect. Theoretical modeling of the air-environment SPR spectra enabled extraction of the Drude plasma frequency ( $\omega_p$ ), damping constant ( $\Gamma$ ), and high-frequency dielectric constant ( $\epsilon_\infty$ ), which were used to model the water-environment spectra. A small degree of plasmonic tuning was observed by varying the oxygen pressure during deposition. The water-environment SPR spectra were complex, and showed multiple resonances. This effect was shown to arise due to interactions between the surface plasmons and the molecular vibrations of the water. Theoretical results for  $\epsilon_\infty$  matched literature values. However, the charge carrier effective masses  $m^*$  required to match the Hall Effect results to the SPR results were significantly higher than literature values.

### 5.1 Introduction

Zinc oxide-based materials, such as aluminum-doped zinc oxide (AZO) and gallium-doped zinc oxide (GZO) have received a significant amount of attention in recent years [1]. As transparent conducting oxide (TCO) materials, they are promising as electrodes for applications such as light-emitting diodes, photovoltaics, and flat-panel displays. They could potentially replace indium tin oxide (ITO) for these applications, due to the rarity of In<sub>2</sub>O<sub>3</sub> [2]. Compared to ITO, doped ZnO-based materials have similar electrical characteristics. Charge carrier densities are typically  $\sim 10^{21}$  cm<sup>-3</sup> (n-type), while typical Hall mobilities are  $\sim 10$  cm<sup>2</sup>V<sup>-1</sup>s<sup>-1</sup>. As with most TCOs, the mobility at high charge carrier concentrations is

limited by ionized impurity scattering [3, 4]. Zinc oxide also has many other interesting and potentially useful properties. In particular, it is strongly piezoelectric, easily forms wire-like nanostructures, and is luminescent [1, 5]. It can be deposited epitaxially on a variety of substrates, notably GaN, *c*-plane sapphire, and *a*-plane sapphire [5]. However, films can be water-sensitive [6, 7].

Thin films of ZnO-based TCOs can have been prepared using a wide variety of deposition methods [1-17]. Pulsed laser deposition (PLD) has been used for many years [18-26], and was the method of choice for this study. In PLD, a high-energy laser is used to ablate a target, coating a substrate with the desired material. One advantage of PLD over sputtering is the ability to independently control the ambient deposition environment, which in ZnO allows precise control over the oxygen chemistry without requiring postdeposition annealing steps [1]. In addition, PLD tends to produce smoother and more homogeneous films with lower deposition temperatures than sputtering. Elevated substrate temperature is known to improve the crystallinity of ZnO, causing an increase in grain size [20, 21, 24]. However, if the species at the substrate surface are sufficiently energetic, their translational mobility will be high enough to produce a crystalline film even at room temperature [11].

The doping mechanism in AZO is complex, with contributions from Zn interstitials, Al<sub>Zn</sub> substitutions and interstitials, and oxygen vacancies [1, 4, 12]. However, it is well known that the charge carrier density can be varied by adjusting the oxygen content of the films, which is performed in PLD by varying the oxygen pressure during deposition [19-21, 26]. This effect opens the possibility of plasmonic tuning, as is seen in ITO [27].

Surface plasmon resonance (SPR) is an optical technique that measures the response of a surface wave, called the surface plasmon polariton (SPP), at the interface of a conductor and a dielectric [28]. This wave may only be excited by light when the momentum of the light exceeds that of a wave in vacuum, which is most commonly achieved by an evanescent wave from total internal reflection. In the Kretschmann geometry, a thin film of the conductor is prepared on a substrate of known refractive index, and the substrate is attached, film side out, to a prism using an index matching fluid. As the incident angle and/or frequency of the light is changed, the evanescent wavevector changes. When it matches the wavevector of the SPP,

the light excites a surface plasmon, which is seen as a reduction in the reflected intensity. This process only occurs for *p*-polarized light, so the ratio of reflectances  $R_p/R_s$  is used to eliminate most non-SPR related features.

The great power of SPR is in its sensitivity to the materials. SPR has been used for many years on silver and gold films in the visible spectrum. With these noble metals, it is used for biosensing devices [29, 30] that operate by detecting a change in the dielectric refractive index when a biomolecule adheres to the film surface. However, SPR is also very sensitive to the properties of the conductor itself. By optical modeling of the thin film reflectance, the optical constants of the film can be determined. In this manner, SPR can be used to study novel plasmonic materials systems, including the surface plasmon resonances of conducting metal oxides.

## 5.2 Method

A target of ZnO doped with 4 at% Al was fabricated with the sintered oxide method. Powdered  $\alpha$ -Al<sub>2</sub>O<sub>3</sub> (99.99% metals basis, Alfa Aesar) and ZnO (99.9% metals basis, Alfa Aesar) were mixed in the appropriate mass ratio and ball milled in ethanol for one hour. The mixture was allowed to dry completely, and was die-pressed into a disc at 8000 psi. The disc was then sintered in an oven at 1250 °C for three hours. The resulting target was ground to the appropriate diameter and sanded to 400 grit.

Film depositions were performed by pulsed laser deposition (PLD), using a KrF excimer ultraviolet laser (248 nm wavelength, Coherent COMPex Pro 102F). The beam energy at the source was kept constant at 250 mJ. Inside the vacuum chamber, this setting produced an energy of 175 mJ on average, as measured by a laser energy meter (Coherent LabMax TOP). The beam was rastered over the target using a rocking mirror, and the target was rotated to increase target consumption and film uniformity. The beam was focused to a spot size of approximately 6.7mm×2.5mm, producing an energy density of approximately 1.0 J cm<sup>-2</sup>.

Three AZO films were produced. Before each deposition, the sapphire ultraviolet window to the chamber was cleaned in aqua regia and UV ozonolysis. The calcium fluoride substrates were also cleaned via UV ozonolysis immediately before use. The target-substrate distance

was 10 cm, and the substrates were rotated. The substrates were not heated. The vacuum chamber was allowed to pump down to  $2.0 \times 10^{-5}$  Torr before each deposition. The AZO films were deposited in oxygen, either at 1.0 mTorr O<sub>2</sub> (for films A and B), or 5.0 mTorr O<sub>2</sub> (for film C). Films A and B were prepared identically to assess method reproducibility.

The deposition rate was measured with stylus profilometry (Veeco Dektak 150) by a series of depositions onto glass, which produced an overall rate of 0.0314 nm/pulse,  $\pm$  5.3%. Neither deposition onto calcium fluoride nor changing oxygen pressure were found to statistically alter the deposition rate. The AZO film thicknesses by this method were kept constant at 200 nm. This thickness was chosen as the theoretical optimum for SPR for this material at these frequencies.

The films were then analyzed using surface plasmon resonance (SPR) spectroscopy. The SPR instrument was a custom unit designed to work as a modular attachment to an FTIR spectrometer, which has been described previously [31]. The SPR spectra were measured using the Kretschmann geometry, in which the substrate was attached to an equilateral CaF<sub>2</sub> prism using refractive index matching fluid (Cargille M-series 1.42). The spectra were collected as the ratio of *p*-polarized reflectance to *s*-polarized reflectance ( $R_p/R_s$ ), over an angle range of 55 to 82 or 85 degrees incidence relative to the sample normal, with three degree increments per scan. Two experimental setups were used for each of the same three films. First, the films were measured in air, using a near-IR InGaAs detector, with 16 cm<sup>-1</sup> resolution. Second, a flow cell was attached and the films were measured in deionized water, using a mid-IR liquid N<sub>2</sub>-cooled mercury cadmium telluride detector, with 8 cm<sup>-1</sup> resolution.

Theoretical modeling of the SPR response as  $R_p/R_s$  was performed by a three-layer transfer matrix method [32], along with a simplex algorithm to match the theoretical model to the experimental data. The matrix method calculates the reflectance at each polarization by considering the boundary conditions at each interface along with the phase change as the light propagates through each material. This assumes that the interfaces are perfectly parallel, and that the materials are homogeneous and non-magnetic. A software package of this model has been made freely available on the Mathworks File Exchange website [33]. The AZO dielectric function (relative permittivity) was modeled using the Drude model:

$$\varepsilon_{AZO} = \varepsilon_{\infty} - \frac{\omega_p^2}{\omega^2 + i\omega\Gamma}. \quad (5.1)$$

In this equation,  $\varepsilon_{\infty}$  is the dielectric constant at high frequency, which is the limit of the model as  $\omega \rightarrow \infty$ . The units of frequency  $\omega$  in this model are normally rad/s, but here are expressed as wavenumber ( $\text{cm}^{-1}$ ) for convenience. The constant  $\omega_p$  is the plasma frequency, which is related to materials parameters by:

$$\omega_p^2 \equiv \frac{ne^2}{\varepsilon_0 m^*}, \quad (5.2)$$

where  $n$  is the charge carrier density,  $e$  is the elementary charge,  $\varepsilon_0$  is the permittivity of free space, and  $m^*$  is the mass of the electrons, which is usually a fraction of the free electron rest mass  $m_e$ . The damping constant  $\Gamma$  is similarly related to materials parameters by:

$$\Gamma = e/\mu m^*, \quad (5.3)$$

where  $\mu$  is the charge carrier mobility. The  $\text{CaF}_2$  dielectric function was obtained via spectroscopic ellipsometry, and is displayed in Fig. 5.1. The water dielectric function was obtained from [34], and is also displayed in Fig. 5.1. The  $\text{CaF}_2$  and water dielectric functions were cubic spline interpolated for use in the model. The air dielectric function was modeled as constant 1.000569.

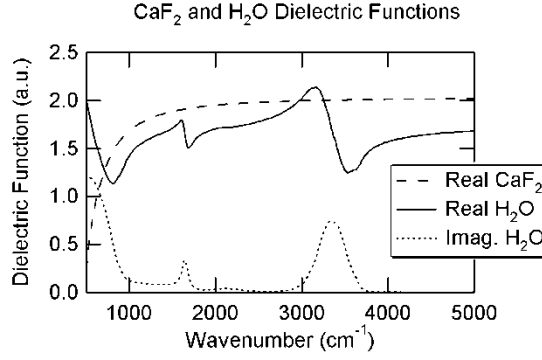


Figure 5.1: The dielectric functions of calcium fluoride, from spectroscopic ellipsometry, and water, from [34]. The water dielectric function has a significant imaginary component due to molecular vibrations.

For the AZO, there are three adjustable parameters:  $\epsilon_{\infty}$ ,  $\omega_p$ , and  $\Gamma$ , which must be related to the experimental results. There are several ways that this may be performed. In this paper, two methods were chosen and the results were compared. First, the three parameters were adjusted freely, fitting the theoretical SPR spectra for the air environment to the experimental spectra as closely as possible. The parameters were adjusted using a modified Nelder-Mead simplex algorithm, which attempted to minimize the combined sum squared error of the normalized spectra for the first six angles of measurement. The numerical results of this method were then used to generate the spectra for the water experiment. Second, the parameters may be calculated using the materials properties in equations (5.2) and (5.3). The values of  $n$  and  $\mu$  may be determined from van der Pauw method Hall Effect measurements, while estimates of  $m^*$  and  $\epsilon_{\infty}$  may be obtained from the literature. In addition, the results may be validated using four-point probe sheet resistance measurements, since resistivity is related to  $n$  and  $\mu$  by:

$$\rho = (n\mu e)^{-1} \quad (5.4)$$

For the Hall Effect, indium metal was used as the contact material, and the magnet was 0.510 T. For both Hall Effect and four-point probe measurements, the measurements occurred at

room temperature, and film thicknesses were assumed to be 200 nm. Applied current varied but was kept near the ohmic maximum.

### 5.3 Results

The results of the air-environment near-IR SPR analysis are shown on the left side of Fig. 5.2 for films A, B, and C, and the theoretical results are displayed on the right side. Two primary features can be seen in each of the spectra. First, the shallow dip at approximately  $5000\text{ cm}^{-1}$  can be identified as the surface plasmon polariton (SPP) of the AZO. Second, the large positive peak at  $8000\text{-}11000\text{ cm}^{-1}$  is caused by a strong reduction in  $R_s$  that is believed to be related to the quasi-bound mode. Both of these primary features are seen to shift to lower frequencies for film C compared to films A and B, which is a consequence of a lower plasma frequency, the result of the higher oxygen pressure during deposition. Lastly, there are significant deviations from the theory at the highest angles. The large positive peak is seen to be significantly less intense than the theory predicts. This could possibly be due to some uncorrected background intensity in  $R_s$ , such that its value is farther from zero than the model predicts. In addition, a strong overall reduction in intensity can be observed at the two or three highest angles. This effect is believed to be due to the limitations of the sample geometry. At glancing incidence, the majority of the beam is scattered or reflected from other areas of the prism or substrate, and does not contact the thin film.

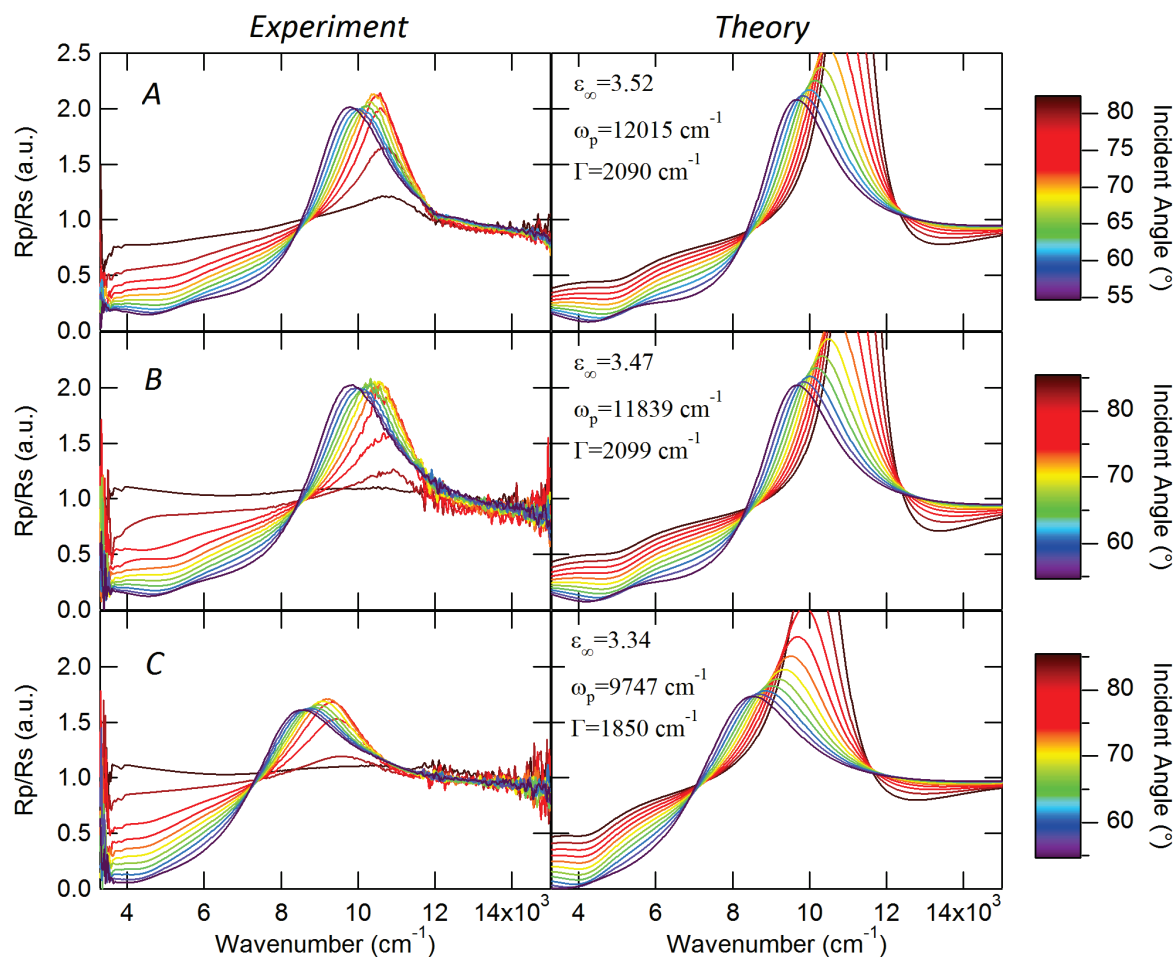


Figure 5.2: (Left side) Near-IR SPR spectra of the AZO films A, B, and C, in an air environment. (Right side) Theoretical modeling results for the same films. Films A and B were prepared identically, while film C was prepared in a higher pressure oxygen environment.

The mid-IR SPR results for the same films, but using water as the ambient medium, are displayed in Fig. 5.3. These spectra are significantly more complex than the near-IR spectra in air. This is a consequence of the increased complexity of the water dielectric function (Fig. 5.1) in the mid-IR, which is due to molecular vibrations. As in Fig. 5.2, at the highest angles

the experimental spectra  $R_p/R_s$  is closer to unity than the model predicts. This is due to limitations of the sample geometry, as described previously.

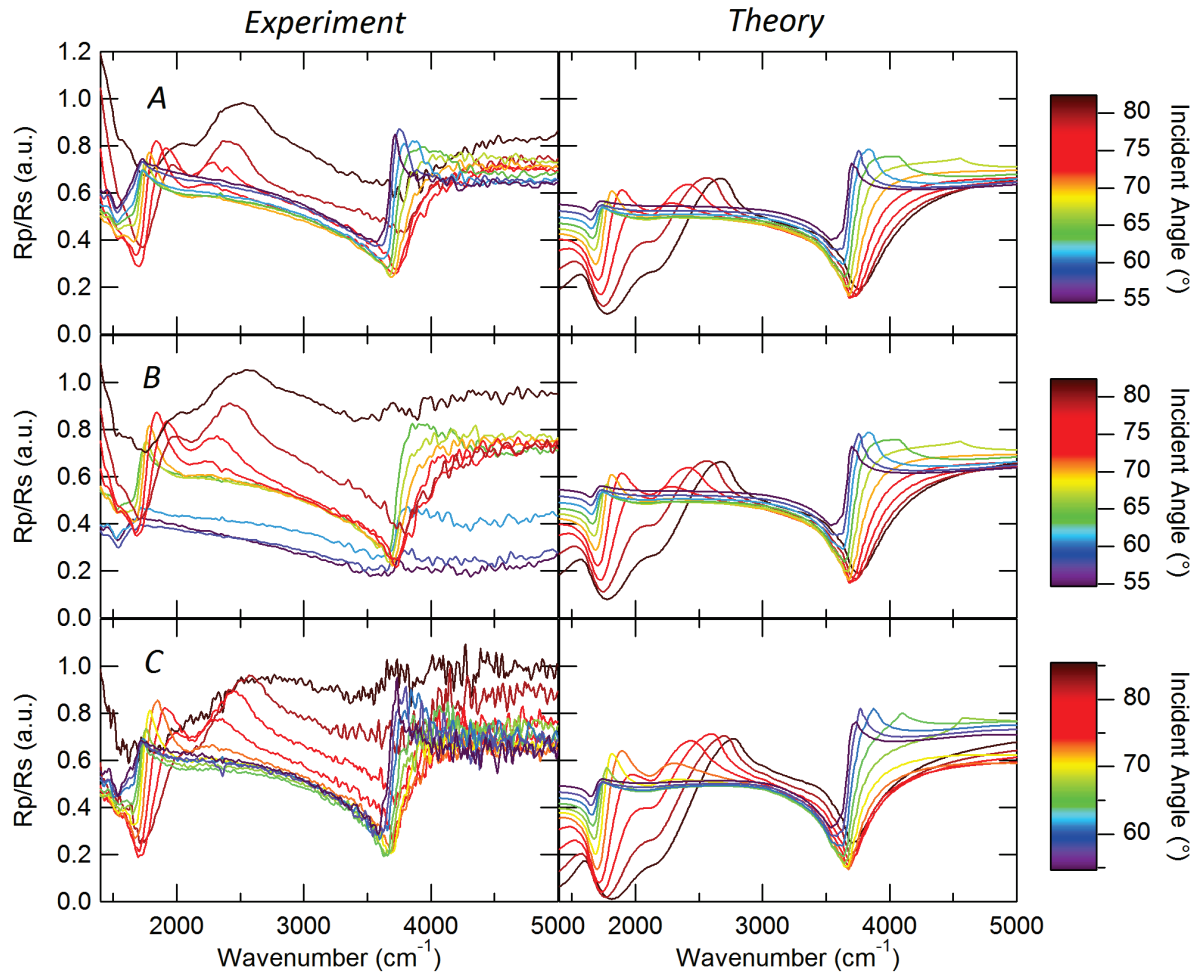


Figure 5.3: (Left side) Mid-IR SPR spectra of the AZO films A, B, and C, in a water environment. (Right side) Theoretical modeling results for the same films, using the numerical results of the air-environment modeling of Fig. 5.2. Films A and B were prepared identically, while film C was prepared in a higher pressure oxygen environment.

The results of the Hall Effect and four-point probe measurements are displayed in Table 5.1. The results overall are consistent with other reports of thin films of AZO [1]. The charge carrier density  $n$  is seen to decrease from film A to B to C. This was expected for film C, which was prepared in a higher pressure  $O_2$  environment and is so expected to have fewer oxygen vacancies as charge carrier donors. However, A and B were prepared identically, and so the difference is indicative of some variability in the deposition method. The charge carrier mobility  $\mu$  is lower than many other reports of ZnO-based materials at the same charge carrier concentration, which can reach as high as  $\sim 50 \text{ cm}^2\text{V}^{-1}\text{s}^{-1}$  [1].

**Table 5.1: Results of the Hall Effect and four-point probe electrical characterizations of the AZO films used in this study.**

<b>Film</b>	<b><math>n</math> (<math>\text{cm}^{-3}</math>)</b>	<b><math>\mu</math> (<math>\text{cm}^2\text{V}^{-1}\text{s}^{-1}</math>)</b>	<b><math>\rho_{Hall}</math> (<math>\Omega \text{ cm}</math>)</b>	<b><math>\rho_{4pt}</math> (<math>\Omega \text{ cm}</math>)</b>
A	$8.847 \times 10^{20}$	7.011	$1.01 \times 10^{-3}$	$1.14 \times 10^{-3}$
B	$7.493 \times 10^{20}$	7.306	$1.14 \times 10^{-3}$	$1.24 \times 10^{-3}$
C	$6.507 \times 10^{20}$	6.242	$1.54 \times 10^{-3}$	$1.6 \times 10^{-3}$

#### 5.4 Discussion

In Fig. 5.2, for the SPR results in air, the shallow absorptions at  $4000\text{-}5000 \text{ cm}^{-1}$  were identified as the surface plasmon polariton (SPP) of the AZO. It is much less intense than the SPPs of, for example, ITO [35] or silver [36]. This is primarily a consequence of the high angles: as the angle is increased, the x-component of the incident electric field is reduced, and so the magnitude of the SPP observed in  $R_p$  is reduced compared to other non-SPP features. In addition, the feature is seen to be only weakly angle dependent, which is also a consequence of the high angles. As the angle is increased, the SPP wavevector approaches its high-frequency limit, and becomes less angle dependent.

The numerical results of the AZO fits are also displayed in Fig. 5.2. The values for the high-frequency dielectric constant  $\epsilon_\infty$  are in good agreement with literature values, which range from 2.99 to 3.78 depending on the sample preparation [1]. Also in Fig. 5.2, the plasma frequencies of the films were seen to change from one film to another. Film C was deposited at higher oxygen pressure than films A and B. This caused a reduction in the number of oxygen vacancies in the film, each of which can contribute two electrons to the charge carrier concentration. Therefore, film C had a lower charge carrier density, and thus a lower plasma frequency, than films A and B. This is reflected directly in the Hall Effect results, and is indirectly observed in the four-point probe results (Table 5.1) and the SPR results (Fig. 5.2). Films A and B also had different plasma frequencies and charge carrier densities. Since their preparation was nominally identical, this difference is indicative of some process variation. It is uncertain what could be the origin of this variation, but one conjecture is that the samples were positioned slightly differently relative to the plasma plume.

Several of the Hall Effect results (Table 5.1) warrant discussion. First, the mobilities  $\mu$  are seen to be lower than many literature values for AZO at similar charge carrier densities [1]. Because the dominant scattering mechanism at these charge carrier densities is ionized impurity scattering [1-3], these mobilities could potentially be improved by further optimization of the Al doping concentration and the oxygen deposition pressure. Second, the Hall Effect results, along with the AZO charge carrier effective mass  $m^*$  (expressed as fraction of vacuum electron mass  $m_e=9.109\times 10^{-31}$  kg), can also be used to calculate the optical parameters  $\omega_p$  and  $\Gamma$  via equations (5.2) and (5.3). This has been done in Table 5.2 in two parts for  $m^*$ . First, an estimate of  $m^*=0.30m_e$  was chosen, since literature values for  $m^*$  are approximately  $0.27m_e$  [37] to  $0.32m_e$  [1]. Second, the values of  $m^*$  were varied to produce plasma frequencies consistent with the results of Fig. 5.2. It is clear from these results that there is a discrepancy between the literature values for  $m^*$  and the combined optical and Hall Effect results of this study. Although it is known that  $m^*$  is a function of charge carrier density in TCOs [38], It is unclear if the unusually high effective masses reported in Table 5.2 are physically real, the by-product of some unascertained measurement error, or the result of a yet-unconsidered secondary effect.

**Table 5.2: Optical parameters for the AZO films using the Hall Effect results and either a literature estimate of  $m^*=0.30m_e$  or varying  $m^*$  to reproduce the plasma frequencies in Fig. 5.2.**

<b>Film</b>	<b><math>m^*</math> (<math>m_e</math>)</b>	<b><math>\omega_p</math> (<math>\text{cm}^{-1}</math>)</b>	<b><math>\Gamma</math> (<math>\text{cm}^{-1}</math>)</b>
A	0.30	16262	4439
B	0.30	14966	4260
C	0.30	13947	4986
A	0.5496	12015	2423
B	0.4794	11839	2666
C	0.6142	9747	2435

Lastly, the features seen in the water-environment mid-IR SPR spectra of Fig. 5.3 will be discussed in detail. These features appear to be significantly more complex than the air-environment near-IR SPR spectra, but the features are easily explained by theory. All of the features are due to the surface plasmon polariton wave. The added complexity arises because of the molecular vibrations of the water, which contribute to the water dielectric function and thus change the surface plasmon dispersion. From the electromagnetic wave equations and the boundary conditions at the metal/dielectric interface [28], the surface plasmon polariton dispersion relation is:

$$k_{SPP} = \frac{\omega}{c} \sqrt{\frac{\epsilon_m \epsilon_d}{\epsilon_m + \epsilon_d}}, \quad (5.5)$$

where  $\epsilon_m$  is the dielectric function of the metal, given by Equation (5.1), and  $\epsilon_d$  is the dielectric function of the dielectric material. When  $\epsilon_d$  is nearly constant, as it is for air, this dispersion relation increases monotonically to the limit  $\omega_{SP} = \omega_p / (\epsilon_\infty + \epsilon_d)^{1/2}$ . For water however, the dielectric function (Fig. 5.1) has a significant amount of structure, which is

contributed to the SPP dispersion relation as seen in Fig. 5.4. The dispersion  $k_{ev}$  of an evanescent wave from  $\text{CaF}_2$  at  $65^\circ$  incidence is also displayed in Fig. 5.4. Where these two lines intersect, the SPP may be driven. It is clear from the figure that there are multiple points of intersection, and so the SPP is simultaneously being driven at multiple frequencies and wavevectors. The points specified by 1, 2, 3, and 4 in the dispersion relation can be related back to the SPR spectra, as shown in Fig. 5.5.

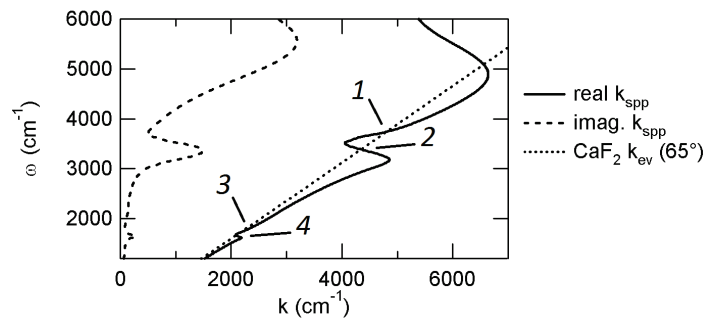


Figure 5.4: Surface plasmon polariton (SPP) dispersion relation for AZO in water ( $k_{spp}$ ), showing real and imaginary parts and the added complexity from the molecular vibrations of the water. Also shown is the dispersion of an evanescent wave from  $\text{CaF}_2$  at  $65^\circ$  incidence, and points of intersection where the SPP may be driven.

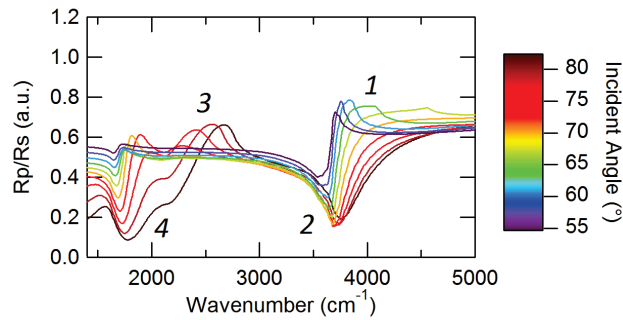


Figure 5.5: Theoretical SPR spectra for film A, with labeled regions corresponding to the labeled intersections in Fig. 5.4.

## 5.5 Conclusions

Thin conductive films of aluminum-doped zinc oxide (AZO) were prepared by pulsed laser deposition (PLD) in oxygen environments on CaF<sub>2</sub> substrates. Their charge carrier densities  $n$  and mobilities  $\mu$  were determined via Hall Effect, and the Hall Effect results were validated with four-point probe resistivity measurements. No substrate heating was necessary to obtain films with sufficiently high charge carrier densities and mobilities. In the future, however, substrate heating could potentially be a valuable deposition parameter to explore. In addition, increases in mobility could potentially be achieved by further optimization of the Al doping concentration and oxygen pressure.

The films' SPR response in the Kretschmann configuration was studied in air in the near-IR, and in water in the mid-IR. For the air-environment spectra, resonances for the surface plasmon polariton (SPP) mode were observed at approximately 5000 cm<sup>-1</sup>. A feature related to the quasi-bound mode was also observed at higher frequencies. For film C, which was prepared at slightly higher oxygen pressure than films A and B, the features occur at lower frequencies, indicative of plasmonic tuning by control of the oxygen vacancies in the film. The water-environment SPR spectra were complex, and showed multiple resonances. This effect was shown to arise due to interactions between the surface plasmons and the molecular vibrations of the water, which contribute significant structure to the water dielectric function and the SPP dispersion. This appears to be the first report of observation of this effect. However, the effects should persist in SPR on any conductor below 4000 cm<sup>-1</sup> in which water is used as the ambient medium. Theoretical modeling of the air-environment SPR spectra enabled extraction of the Drude plasma frequency ( $\omega_p$ ), damping constant ( $\Gamma$ ), and high-frequency dielectric constant ( $\epsilon_\infty$ ), which were used to model the water-environment spectra with satisfactory results. The values for  $\epsilon_\infty$  matched literature values. However, the charge carrier effective masses  $m^*$  required to match the Hall Effect results to the SPR results were significantly higher than literature values. It is uncertain at this point what the cause of this effect might be.

## 5.6 Acknowledgments

I would like to thank Karl Booksh for the use of his SPR spectrometer and substrates, and Edward Sachet for the CaF<sub>2</sub> dielectric function. This work was funded by NSF grants 1112017 and 1111618.

## 5.7 References

1. K. Ellmer, A. Klein, and B. Rech, *Transparent conductive zinc oxide* (Springer, 2008).
2. K. Ellmer, "Resistivity of polycrystalline zinc oxide films: current status and physical limit," *Journal of Physics D: Applied Physics* **34**, 3097 (2001).
3. K. Ellmer, and R. Mientus, "Carrier transport in polycrystalline ITO and ZnO:Al II: The influence of grain barriers and boundaries," *Thin Solid Films* **516**, 5829-5835 (2008).
4. T. Minami, H. Sato, K. Ohashi, T. Tomofuji, and S. Takata, "Conduction mechanism of highly conductive and transparent zinc oxide thin films prepared by magnetron sputtering," *Journal of Crystal Growth* **117**, 370-374 (1992).
5. H. Morkoç, and Ü. Özgür, *Zinc oxide: fundamentals, materials and device technology* (Wiley-Vch, 2008).
6. Y. Kishimoto, O. Nakagawara, H. Seto, Y. Koshido, and Y. Yoshino, "Improvement in moisture durability of ZnO transparent conductive films with Ga heavy doping process," *Vacuum* **83**, 544-547 (2008).
7. O. Nakagawara, Y. Kishimoto, H. Seto, Y. Koshido, Y. Yoshino, and T. Makino, "Moisture-resistant ZnO transparent conductive films with Ga heavy doping," *Applied Physics Letters* **89** (2006).
8. M. A. Thomas, J. C. Armstrong, and J. Cui, "New approach toward transparent and conductive ZnO by atomic layer deposition: Hydrogen plasma doping," *Journal of*

Vacuum Science & Technology A: Vacuum, Surfaces, and Films **31**, 01A130-136 (2013).

9. R. Chandramohan, V. Dhanasekaran, S. Ezhilvizhian, T. A. Vijayan, J. Thirumalai, A. J. Peter, and T. Mahalingam, "Spectral properties of aluminium doped zinc oxide thin films prepared by SILAR method," *Journal of Materials Science: Materials in Electronics* **23**, 390-397 (2012).
10. M. Karger, and M. Schilling, "Epitaxial properties of Al-doped ZnO thin films grown by pulsed laser deposition on SrTiO<sub>3</sub>(001)," *Physical Review B* **71**, 075304 (2005).
11. E. Sachet, M. Losego, J. Guske, S. Franzen, and J. Maria, "Mid-infrared surface plasmon resonance in zinc oxide semiconductor thin films," *Applied Physics Letters* **102**, 051111 (2013).
12. A. Singh, R. Mehra, A. Yoshida, and A. Wakahara, "Doping mechanism in aluminum doped zinc oxide films," *Journal of Applied Physics* **95**, 3640-3643 (2004).
13. W. Tang, and D. C. Cameron, "Aluminum-doped zinc oxide transparent conductors deposited by the sol-gel process," *Thin Solid Films* **238**, 83-87 (1994).
14. V. Assuncao, E. Fortunato, A. Marques, H. Aguas, I. Ferreira, M. Costa, and R. Martins, "Influence of the deposition pressure on the properties of transparent and conductive ZnO : Ga thin-film produced by r.f. sputtering at room temperature," *Thin Solid Films* **427**, 401-405 (2003).
15. V. Assuncao, E. Fortunato, A. Marques, A. Goncalves, I. Ferreira, H. Aguas, and R. Martins, "New challenges on gallium-doped zinc oxide films prepared by r.f. magnetron sputtering," *Thin Solid Films* **442**, 102-106 (2003).
16. E. Fortunato, P. Nunes, A. Marques, D. Costa, H. Aguas, I. Ferreira, M. Costa, R. Martins, and T. Vieira, "Highly conductive/transparent ZnO : Al thin films deposited at

- room temperature by rf magnetron sputtering," *Advanced Materials Forum I* **230-2**, 571-574 (2002).
17. P. Song, M. Watanabe, M. Kon, A. Mitsui, and Y. Shigesato, "Electrical and optical properties of gallium-doped zinc oxide films deposited by dc magnetron sputtering," *Thin Solid Films* **411**, 82-86 (2002).
  18. J. Mass, P. Bhattacharya, and R. S. Katiyar, "Effect of high substrate temperature on Al-doped ZnO thin films grown by pulsed laser deposition," *Materials Science and Engineering: B* **103**, 9-15 (2003).
  19. H. Kim, J. Horwitz, S. Qadri, and D. Chrisey, "Epitaxial growth of Al-doped ZnO thin films grown by pulsed laser deposition," *Thin Solid Films* **420**, 107-111 (2002).
  20. A. Singh, R. Mehra, N. Buthrath, A. Wakahara, and A. Yoshida, "Highly conductive and transparent aluminum-doped zinc oxide thin films prepared by pulsed laser deposition in oxygen ambient," *Journal of Applied Physics* **90**, 5661-5665 (2001).
  21. H. Kim, C. Gilmore, J. Horwitz, A. Pique, H. Murata, G. Kushto, R. Schlaf, Z. Kafafi, and D. Chrisey, "Transparent conducting aluminum-doped zinc oxide thin films for organic light-emitting devices," *Applied Physics Letters* **76**, 259-261 (2000).
  22. R. Mehra, A. Singh, M. Kumar, A. Yoshida, V. Kumar, and S. Agarwal, "Transparent conducting ZnO : Al thin films prepared by ArF excimer laser ablation," *Proceeding of the Tenth International Workshop on the Physics of Semiconductor Devices, Vols I and II* **3975**, 1198-1205 (2000).
  23. M. Hiramatsu, K. Imaeda, N. Horio, and M. Nawata, "Transparent conducting ZnO thin films prepared by XeCl excimer laser ablation," *Journal of Vacuum Science & Technology A: Vacuum, Surfaces, and Films* **16**, 669-673 (1998).

24. G. A. Hirata, J. McKittrick, J. Siqueiros, O. A. Lopez, T. Cheeks, O. Contreras, and J. Y. Yi, "High transmittance--low resistivity ZnO:Ga films by laser ablation," (AVS, Mineapolis, Minnesota (USA), 1996), pp. 791-794.
25. A. Suzuki, T. Matsushita, N. Wada, Y. Sakamoto, and M. Okuda, "Transparent Conducting Al-Doped ZnO Thin Films Prepared by Pulsed Laser Deposition," *Japanese Journal of Applied Physics* **35**, L56-L59 (1996).
26. M. Lorenz, E. M. Kaidashev, H. von Wenckstern, V. Riede, C. Bundesmann, D. Spemann, G. Benndorf, H. Hochmuth, A. Rahm, H. C. Semmelhack, and M. Grundmann, "Optical and electrical properties of epitaxial  $(\text{Mg,Cd})_x\text{Zn}_{1-x}\text{O}$ , ZnO, and ZnO:(Ga,Al) thin films on c-plane sapphire grown by pulsed laser deposition," *Solid-State Electronics* **47**, 2205-2209 (2003).
27. M. Losego, A. Efremenko, C. Rhodes, M. Cerruti, S. Franzen, and J. Maria, "Conductive oxide thin films: Model systems for understanding and controlling surface plasmon resonance," *Journal of Applied Physics* **106**, 024903 (2009).
28. S. A. Maier, *Plasmonics : fundamentals and applications* (Springer, New York, 2007).
29. J. Homola, S. Yee, and G. Gauglitz, "Surface plasmon resonance sensors: review," *Sensors and Actuators B-Chemical* **54**, 3-15 (1999).
30. J. Homola, "Present and future of surface plasmon resonance biosensors," *Analytical and Bioanalytical Chemistry* **377**, 528-539 (2003).
31. N. Menegazzo, L. Kegel, Y. Kim, D. Allen, and K. Booksh, "Adaptable infrared surface plasmon resonance spectroscopy accessory," *Review of Scientific Instruments* **83** (2012).
32. Z. e. Knittl, *Optics of thin films; an optical multilayer theory* (Wiley, London, New York,, 1976).

33. J. T. Guske, "SPR XPhase," (2013),  
<http://www.mathworks.com/matlabcentral/fileexchange/41090>.
34. D. J. Segelstein, "The complex refractive index of water," in *Physics*(Department of Physics. University of Missouri-Kansas City, Kansas City, 1981).
35. C. Rhodes, M. Cerruti, A. Efremenko, M. Losego, D. Aspnes, J. Maria, and S. Franzen, "Dependence of plasmon polaritons on the thickness of indium tin oxide thin films," *Journal of Applied Physics* **103**, 093108 (2008).
36. J. Guske, J. Brown, A. Welsh, and S. Franzen, "Infrared surface plasmon resonance of AZO-Ag-AZO sandwich thin films," *Optics Express* **20**, 23215-23226 (2012).
37. H. Sheng, S. Muthukumar, N. W. Emanetoglu, and Y. Lu, "Schottky diode with Ag on (112-bar 0) epitaxial ZnO film," *Applied Physics Letters* **80**, 2132-2134 (2002).
38. T. Pisarkiewicz, K. Zakrzewska, and E. Leja, "Scattering of charge carriers in transparent and conducting thin oxide films with a non-parabolic conduction band," *Thin Solid Films* **174, Part 1**, 217-223 (1989).